

Motor Design and Control for Scalable Distributed Actuation

by

David Preiss

B.Eng. McGill University (2015)

Submitted to the Media Arts and Sciences, School of Architecture and Planning

in partial fulfillment of the requirements for the degree of

Master of Science

at the

MASSACHUSETTS INSTITUTE OF TECHNOLOGY

September 2022

© Massachusetts Institute of Technology 2022. All rights reserved.

Author
Media Arts and Sciences, School of Architecture and Planning
August 2022

Certified by.....
Prof. Neil Gershenfeld
Director, MIT Center for Bits and Atoms
Thesis Supervisor

Accepted by
Prof. Tod Machover
Academic Head, Program in Media Arts and Sciences

Motor Design and Control for Scalable Distributed Actuation

by

David Preiss

Submitted to the Media Arts and Sciences, School of Architecture and Planning
on August 2022, in partial fulfillment of the
requirements for the degree of
Master of Science

Abstract

Machine design is often constrained to a limited number of controllable degrees of freedom due to the cost and complexity associated with integrating large numbers of actuators. This thesis explores the hardware and control development for a motor architecture designed for distributed actuation, where actuator quantities in the 100s or 1000s are required across macro scale structures. Availability of a low cost and easily integrated actuator at these scales would open new regimes for fields such as robotics, manufacturing, human computer interaction and wireless communication.

A survey of prior distributed actuation research is conducted which includes shape memory alloy, piezoelectric, hydraulic, and electric motor topologies. A new approach using multiplexed two-phase axial flux PCB motors is designed and iterated on through empirical testing and simulation. These motors are integrated into a modular 64 actuator array, and a proof of concept is built capable of distributed linear motion for interpolation of a surface or as independent degrees of freedom. Motor commutation is achieved through multiplexing of individual motor windings, allowing for sub-linear cost and component count scaling. Actuator performance over a number of performance parameters is addressed, including output torque, speed, mass, resolution, range of motion, as well as parameters critical to scalability including motor footprint, cost and power consumption. Finally two applications of serially distributed actuation are discussed, including the design of modular continuum robots from a discrete toolkit of structural elements, as well as a serpentine actuator with many controlled degrees of freedom.

Thesis Supervisor: Prof. Neil Gershenfeld
Title: Director, MIT Center for Bits and Atoms

Acknowledgments

Big thank yous to the following people:

Neil Gershenfeld for creating such a unique place in the CBA, filling it with amazing people and tools, and enabling me to learn so much over the past two years.

Jeff Lang and David Trumper for your valuable time and feedback as thesis readers.

CBA folks: Miana, Alfonso, Camron, Zach, Erik, Amira, Jake, Chris, Pat, and the many past members who've made the basement such a fun and mysterious place. In particular thank you to Erik for your patience and enthusiasm as a TA, and for the many hours you devoted to holding my hand through electromagnetism. To Alfonso for your help making origami on the Zund, and being an amazing basement neighbor.

Mark Feldmeier and David Bono for your EE wizardry, and generously holding office hours in the midst of a global pandemic.

Ted Hall and the folks at ShopBot for taking a chance on me as an unqualified environmental engineering student, which allowed me to find work that I love.

Brian for your support and guidance while I was an intern, and later as a coworker and friend. Looking back I don't know how you answered all of my Solidworks questions as patiently and kindly as you did.

Everyone at Formlabs, particularly Kostas for being an inspiring mentor, and teaching me to think like a mechanical engineer.

August for countless late night engineering discussions, and for swooping in and saving me on multiple occasions over the course of this degree. I've learned so much from you, and don't think I would be doing this work had it not been for our friendship.

The residents of Brown House and Auburn St for shared meals, weekend excursions, and thoughtful discussions.

Hayley for being the best imaginable partner, roommate, and friend, and your expertise with object oriented programming.

Motor Design and Control for Scalable Distributed Actuation

by
David Preiss

This thesis has been reviewed and approved by the following committee members:

Neil Gershenfeld
Director at the Center for Bits and Atoms
Professor, Media Arts and Sciences
Massachusetts Institute of Technology

Jeffrey Lang
Professor, Electrical Engineering and Computer Science
Massachusetts Institute of Technology

David Trumper
Professor, Mechanical Engineering
Massachusetts Institute of Technology

Contents

1	Introduction	11
1.1	Contributions	12
1.2	Applications	13
1.2.1	Manufacturing	13
1.2.2	Human Computer Interaction	15
1.2.3	Wireless Communication and Optics	16
1.3	Making Motors the Way We Make Transistors	18
2	Actuator Design	21
2.1	Prior Art in Distributed Actuation	21
2.1.1	Shape Memory Alloy	22
2.1.2	Piezoelectric	23
2.1.3	Hydraulic	24
2.1.4	Electric	25
2.2	Stator Design	28
2.3	Rotor Design	32
3	Motor Modeling and Characterization	37
3.1	Modeling Flux Density	38
3.1.1	Magnetic Circuit Model	39
3.1.2	Volume Integral Model	42
3.1.3	Finite Element Model	50
3.2	Torque Production	56

3.3	Characterization	58
4	Parallel Distributed Actuation	61
4.1	Linear Motor Array	63
4.1.1	Mechanical Design	63
4.1.2	Electrical Design	67
4.1.3	Scaling	71
4.1.4	Array Control Software	73
4.1.5	Commutation Control	74
4.2	Characterization	80
5	Serial Distributed Actuation	85
5.1	Continuum Actuation	86
5.1.1	Modular Robot Toolkit	87
5.2	Serpentine Actuation	92
5.2.1	Ribosomal Assemblers	93
6	Conclusion	97

Chapter 1

Introduction

To fully constrain a rigid body in three-dimensional space requires control of six total degrees of freedom. These are composed of three perpendicular translational axes commonly referred to as X , Y , and Z as well as three rotational axes about each of those translations θ_X , θ_Y , and θ_Z . Therefore robotic manipulators commonly devote exactly six actuators placed in series to control position and orientation of an end effector. In practice, demand for actuation often exceeds fundamental design principles, and the same robotic manipulator might require global actuation in X and Y around a warehouse floor, or wield a gripper with additional degrees of freedom. For context, the human body consists of over 600 independently controllable muscles [4], packaged into a roughly 70,000 cubic centimeter volume. A robot with similar proportions devoting 20% of its volume to actuation would leave only a cube with 28.5mm side length for each actuator. Therefore integrating controllable degrees of freedom are a costly addition for machine designers in terms of volume, but also cost, weight, and power consumption.

There are swathes of applications where total degrees of freedom can scale exponentially. An inkjet printer might devote on the order of thousands of actuators to ensure each jet prints quickly and reliably [7], and an optical telescope might require a deformable mirror composed of hundreds of actuators to control surface tolerances. These applications are considered to require distributed actuation, where a large number of actuators are arranged in parallel or series, as discussed in Chapters 4 and 5

respectively. The scope of work is narrowed to macro-scale actuation, where actuator stroke and size are on the millimeter scale, and actuator count is on the order of 100s or 1000s. Massively parallelized distributed actuators at these scales rarely see use in industry today, due to increasing integration and control complexity. Minimizing cost and complexity inevitably results in sacrifices to actuator performance, such as speed, torque, and efficiency. A system with 10,000 controlled degrees of freedom could easily require power consumption in the $200kW$ range, the average equivalent of 40 American homes. Similarly a conventionally low unit cost of \$10.00 per actuator would result in a total cost of \$100,000, which prices such a system outside of most consumer, and many industrial applications.

1.1 Contributions

Most broadly this thesis strives to establish a scalable actuator and control architecture, intended to allow for wider feasibility of macro-scale distributed actuation. The primary focus is placed on a planar array of rotary actuators, which are coupled with a lead screw to produce linear motion. These actuators are electrically and mechanically designed to be scalable to control 100s or 1000s of degrees of freedom. This is achieved through the design of an axial flux 2-phase stepper motor, as discussed in Chapter 2, for which the stator can be manufactured in parallel on a printed circuit board (PCB), and optimization of the rotor and motion components. This design is then iterated on in Chapter 3 using a variety of simulation techniques, including a magnetic circuit model, volume integral model, and an FEA solver. Chapter 4 outlines integrating these motors into a modular 8x8 array, where motor commutation is multiplexed at the power electronics level, allowing for arrays of $N \times M$ motors to be controlled with a sublinear number of $N + M$ drivers. While the primary focus is on an array, such an arrangement as been to be applicable for volumetric actuation of a structure [5], used to drive tendons for serial actuation [10], or be panelized into smaller modules as discussed in section 5.2. Chapter 5 discusses two implementations of serially distributed actuation. This includes a continuum case, where tendons are

routed through a selectively compliant modular structure, as well as a serpentine case, where 3 DOF modules constructed using a proxy for the motors designed previously are used to actuate a limb.

1.2 Applications

This section outlines several areas of research and industrial application where scalable distributed actuation is actively applied. This list is not at all comprehensive, and notably absent are robotics actuations, which are discussed in more depth in Chapter 5, and a variety of fluid handling applications where demand is typically limited to binary actuation. Later Section 2.1 will explore some of the more common actuator topologies and methods that have been applied to these applications. The parameters listed below were found to be recurring metrics used in the literature to grade the suitability of a given motor architecture for a given task. These parameters are later used in Table 6.1, to assess the contributions of this thesis.

- Actuator Dimensions
- Output Torque or Force
- Rotational or Linear Speed
- Rotational or Linear Resolution
- Rotational or Linear Stroke
- Power Consumption per Actuator
- Mass per Actuator
- Cost per Actuator

1.2.1 Manufacturing

Parallel distributed actuation for use in reconfigurable tooling has garnered research interest dating back to 1863 [33]. Since then large scale reconfigurable molds such as those shown in Figure 1-1 have been designed for reducing cycle times for stretch sheet metal forming, thermoforming, and composite layup processes. Adapa is a Danish manufacturer of reconfigurable molds used for casting curved concrete architectural panels, as well as other composites [2]. A PhD thesis by Zhijian Wang at University

of Nottingham has an incredibly extensive prior art on pin actuated reconfigurable vacuum molding tools [57], and an equally thorough background is given to sheet metal forming in [33]. Reconfigurable surfaces are also used for part fixturing and surface gauging, where the final tolerance for a formed sheet good can be maintained and inspected by a dense array of linear actuators equipped with contact sensors. Higher actuator densities could ultimately provide a means to achieve reconfigurable tooling for extrusion or injection molding processes, where initial tooling costs can often exceed the net value of parts being manufactured.



Figure 1-1: A) A 2688 actuator $1 \times 1.8m$ reconfigurable die for sheet metal forming built by David Hardt at MIT [36]. B) Reconfigurable composite layup die using NEMA packaged steppers and leadscrews [2].

In the context of additive manufacturing, Figure 1-2 shows figures from several recent papers demonstrating the use of reconfigurable print beds below an FDM 3D printer. A reconfigurable bed can be used to increase cycle time and decrease support material usage for parts with overhanging geometry that would otherwise require printed supports. This is particularly impactful for prints where print material costs are high, such as metal 3D printing, or where support materials make part extraction difficult. An similar application is towards non-planar 3D printing [45], where a base mold is printed to act as a mold surface for a final part requiring contoured base geometry. Final parts are often thin walled fiber reinforced parts mimicking a traditional composite contour part, in which final part volume is a fraction of material

volume invested in the base mold.

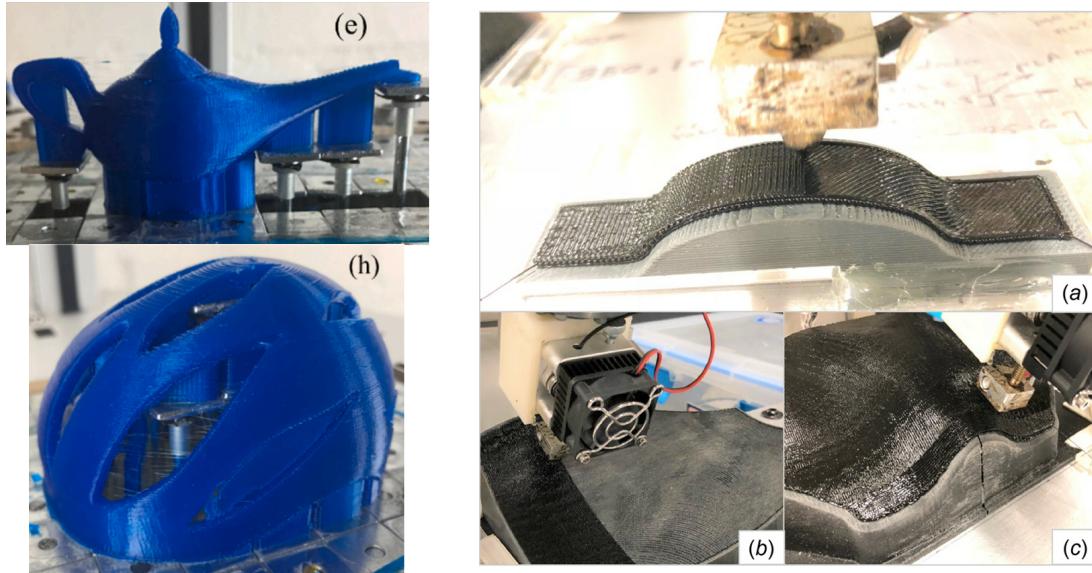


Figure 1-2: A) Reconfigurable FDM print bed for minimizing support structures [59].
B) Non-planar 3D printing toolpaths over printed support structures [45].

1.2.2 Human Computer Interaction

Early mechanical dot-matrix displays represented one of the largest demands for distributed actuation dating back to the early 1960s [48]. These displays were composed of mechanically flippable binary pixels that could be matrixed to form a reconfigurable display with zero static power consumption. Before being superseded by LED matrices, the most common implementation involved a multiplexed array of diode separated inductors, where each inductor produced a field that induced rotation in the pixel between two states.



Figure 1-3: An interpolated shape display intended for augmented and virtual reality [47].

Today there exists an active body of research working towards realizing 2.5D reconfigurable surfaces, intended for use as peripherals for augmented or virtual reality, or as assistive technology for the visually impaired [61] [46] [27] [47]. These displays provide tangible haptics that allow a user to directly touch and manipulate a simulated surface. Figure 1-1 shows a number of these examples from MIT and Stanford, where Figure 1-3 shows a more recent sparsely actuated array that uses a compliant surface to extrapolate between motor gaps. These human computer interaction applications typically prioritize actuator footprint, speed, and stroke, which all influence the spatial and temporal frequency of information that can be represented.

1.2.3 Wireless Communication and Optics

Distributed actuation over a planar array of linear actuators is commonly referred to as an adaptive surface in the context of wireless communication and imaging. In optics, deformable mirrors are often required to correct for laser spot size and shape, or for telescope wavefront correction [40]. As discussed in sections 2.1.2 and 2.1.4, these actuators typically only require short linear displacement, but with resolution in the nanometer scale to correct for aberrations on the order of the wavelength of light. For an overview of the current adaptive optics landscape, an excellent summary can be found in [30].

Wavelengths at radio frequency are significantly larger than visible light, and

therefore the peak resolution requirement is reduced for RF antenna applications. Figure 1-4 shows the $100\mu\text{m}$ surface tolerances required across the 36.6m primary reflector of Lincoln Lab’s Haystack Antenna, which must be maintained over changing environmental loads such as thermal expansion, wind and rain, as well as changing gravitational from antenna angle adjustment. Many RF antenna will therefore use large scale distributed actuation to maintain surface tolerance requirements, including the Greenbank and Large Millimeter Telescopes. where the former uses 2209 brushed DC motor driven ballscrews to achieve linear motion, and LVDTs for loop closing [26] [16].

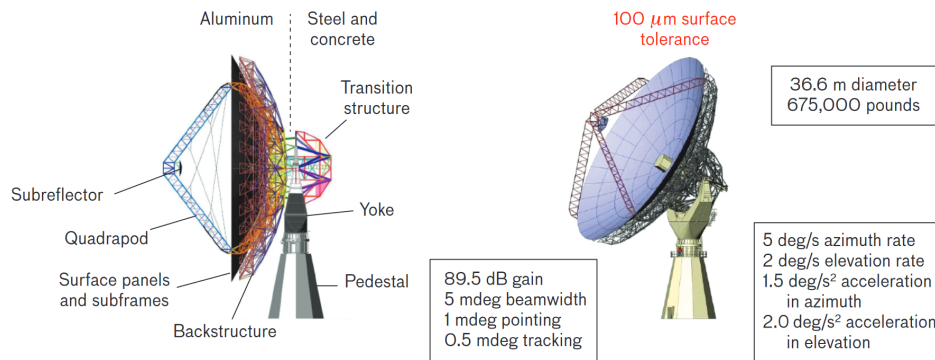


Figure 1-4: Geometric requirements for Lincoln Lab’s Haystack RF Antenna, as well as a tolerance stackup of the primary reflector to be accounted for in the manufacturing process

Researchers at Caltech’s CHIC group investigated the potential for geometric reconfigurability of phased array antenna [58]. Figure 1-5 shows the potential for geometric reconfigurability to improve antenna gain when beamforming at extreme angles relative to the planar antenna norm. It should be noted that phased array antenna are capable of accounting for surface accuracy at the RF switching level, and therefore geometric reconfigurability is used as a means to increase radiation pattern diversity. The antenna in [58] was therefore manually actuated and did not require a tightly controlled surface tolerance.

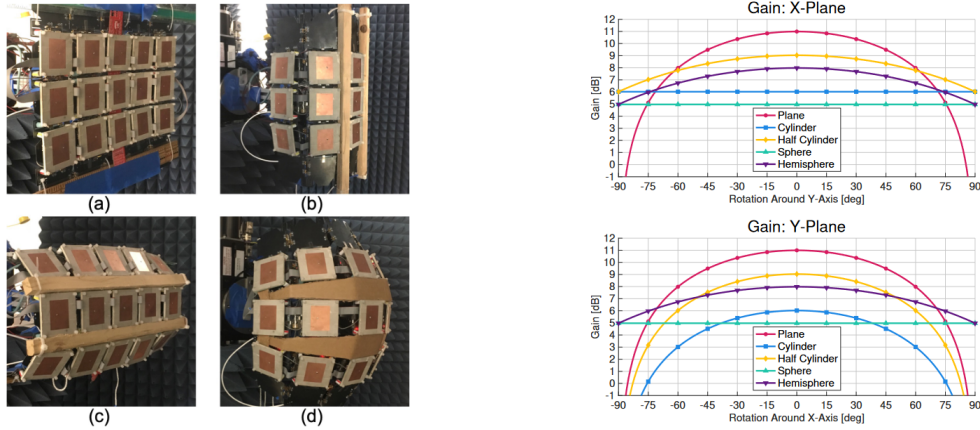


Figure 1-5: A) Shape changing phased array antenna demonstrating reconfigurability, including planar, cylindrical, and spherical. B) Simulated gain for various phased array geometries over a rotational sweep of beam angle. [58]

1.3 Making Motors the Way We Make Transistors

With our current progression of Moore's Law, a single integrated circuit (IC) can be expected to be composed of tens of billions of individual transistors, and this number increases orders of magnitude when considering the macro-scale wafer it was diced from. IC manufacturers can produce transistors at these scales by exposing features simultaneously through masked lithography. This parallelized process can occur orders of magnitude faster than a direct-write process, such as E-beam lithography, which can be considered analogously time-intensive to the manufacturing of current wire-wound stators. The ultimate goal for this work is to make a small step towards an actuator topology that can be produced and controlled at quantities comparable to the modern transistor.

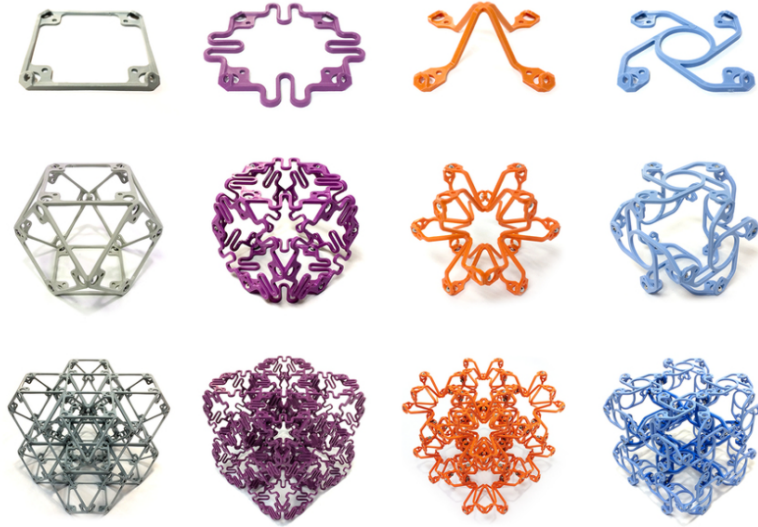


Figure 1-6: Discretely assembled mechanical metamaterials, demonstrating a variety of material properties including isotropic linear elastic, chiral, and auxetic compliance [21].

Actuation at this scale is pointless without something to actuate. Today much of our work at the CBA involves the design of discrete voxelized metamaterials, which are modular building blocks that have been used to construct lightweight space structures [22], and shape changing hydrofoils [42]. Recent research efforts have focused on the family of voxels shown in Figure 5-2 which can be used to introduce selective compliance into a structure allowing for passive or active degrees of freedom. Chapter 5 discusses the use of tendon actuation to effectively control a continuum of degrees of freedom across a voxel structure, and a large body of work exists at the CBA where actuation is an integral component of the voxel itself. Ara Knaian's thesis focused on the use of an electropermanent actuator [24], which were used to demonstrate stochastic assembly and disassembly. Cheney et al. propose a species of generatively evolved soft robots made up of passive and active voxels [5]. Their actuators are akin to biological muscle, and allow a voxel to undergo 20% isotropic volumetric contraction and expansion, which can be periodically applied both in and out of phase as prescribed by voxel type. Figure 1-7 shows that these simple actuators can be used to arbitrarily complex motion like walking or grasping. Realizing the potential

of these applications will require an actuator topology that can be buried behind a layer of abstraction not achievable by today's manufacturing standards.

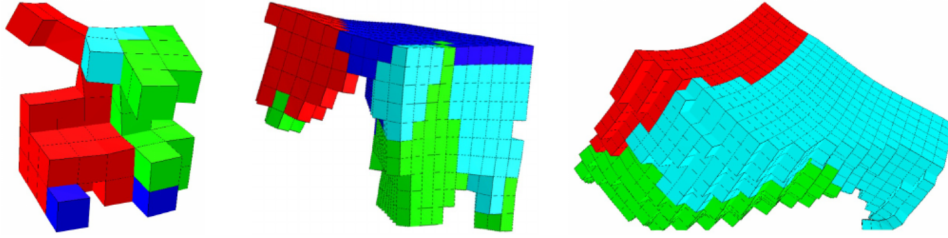


Figure 1-7: Computationally evolved walking soft robots made up of passive (blue) and actuated volumetrically expanding and contracting voxels (green and red) [5].

Chapter 2

Actuator Design

This chapter outlines the design of a 2-phase axial flux PCB motor, which was selected as a suitable candidate from the survey of prior art discussed in the following Section 2.1. These designs set out to address the scaling requirements outlined in Section 1.2. The design process was guided by several approaches to simulation and modeling, which are compiled in Chapter 3.

2.1 Prior Art in Distributed Actuation

Today the landscape of motor topologies is vast, and it is possible to find to find an actuator that meets the mechanical performance requirements of most applications. Electric vehicle manufacturers have optimized their motors for maximum power density while maintaining efficiencies in the 90% range over a wide range of speed and torque demands [43]. This performance comes at a cost in terms of scalability, and distributed actuation specific research has received comparatively little attention. The following section contains a literature review of motor architectures used in macro-scale distributed actuation applications. This includes many electric motors in line with the contributions of this thesis, as well as less common actuator architectures that use shape memory alloys, piezoelectrics, and hydraulics.

2.1.1 Shape Memory Alloy

Shape memory alloy (SMA) actuators have been widely used to construct 2.5D actuator arrays, although SMA's thermal response time and hysteresis has limited most implementations to binary open loop control. A common approach is to pass current through a helically wound SMA such as NiTi, or convect hot or cold fluid across it, causing expansion or retraction of the helix via the shape memory effect [35].

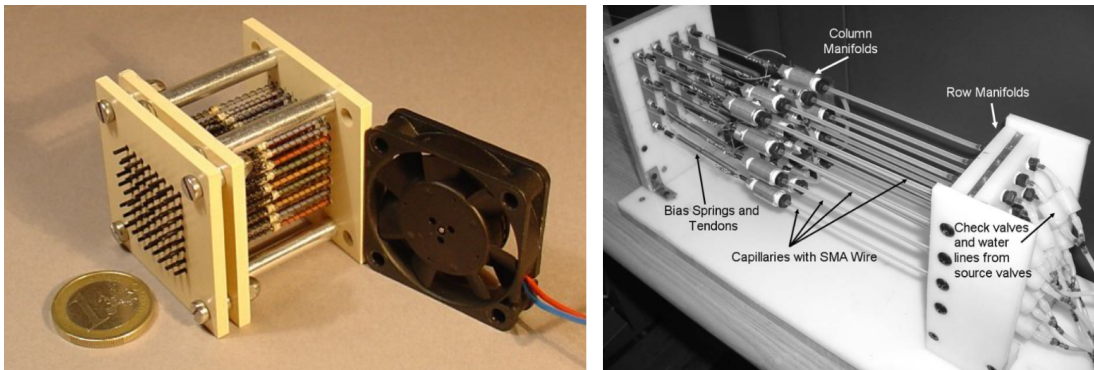


Figure 2-1: A) A 64 actuator SMA actuated tactile interface by Velázquez et al [54]. B) A 16 actuator array for control of high degrees of freedom [10].

The 2.6mm pitch tactile array shown in Figure 2-1-A achieved a force output of 320mN with a bandwidth of 1.5Hz over a 1mm stroke. The entire array weighed 200g , which comes to just over 3g per actuator. A limitation on array size noted by Veazquez et al. was thermal bleed between adjacent actuators, resulting in parasitic motion between neighboring pins [54]. One method to combat this effect is shown in Figure 2-1-B, where a 16 count SMA array is controlled by a matrixed manifold and valve system that selectively pumped heated or cooled water over individually SMAs. The prototype was able to reduce the number of valves required to control an N-by-N array to $2N + 2$ by matrixing the array [35]. Similar to this thesis. the paper focuses on robotic applications, where with larger arrays, binary SMA actuators could be routed in series or parallel to provide increased actuator resolution or force output.

2.1.2 Piezoelectric

Early piezo-driven actuator arrays date back to the 1970's [44] where they were used to drive deformable mirrors, and today piezo arrays have been commoditized to the point that a 40-actuator, 18mm diameter deformable mirror can be purchased from Thorlabs for \$4000 [50]. This highlights one of their main strengths, which is extremely small actuator size allowing for high density arrays. With error budgets dictated by the wavelength of light, linear resolution for these actuators is on the order of $< 1nm$, while required stroke is limited to tens of μm , and bandwidth in the kHz regime [40]. Piezoelectric actuators have inherent hysteresis and non-linearity, but with calibration can be feed-forward controlled in both serially stacked, and walking configurations [60]. Despite their low power consumption, full scale piezoelectric deformation may require RMS drive voltages in the 100V to 200V range [32], and so to avoid networking high voltages across a macro-scale distributed actuation structure, DC-DC converters or transformers would need to be added locally.

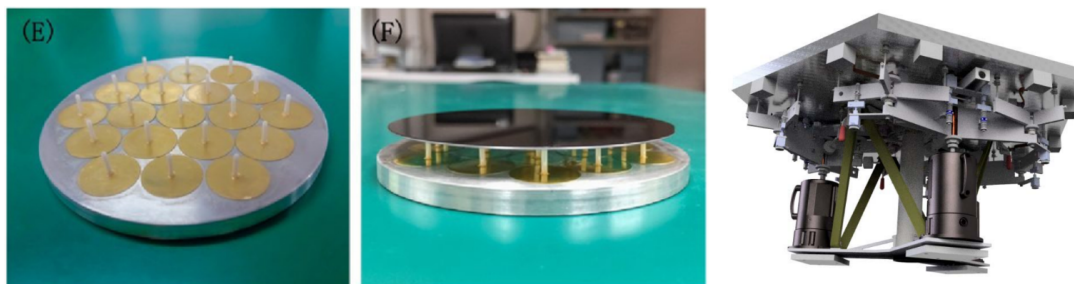


Figure 2-2: A) Low-cost 19 piezo actuator deformable mirror prototype [51] (captioned E and F). B) Piezoelectric actuators in series with servo driven ballscrews make up the 2394 actuators in the European Extremely Large Telescope [8]

Researchers from Ningbo University built a prototype deformable mirror using inexpensive commercially available serially stacked piezoelectric buzzers, but these stacked configurations are limited to linear strokes on the order of $10\mu m$ [51]. More in line with the direction of this thesis, to achieve actuator stroke at the millimeter scale, a stick-slip or stepping motor architecture would need to be taken [28], however this approach has not yet been applied to a distributed use case. Commercially

available SMD piezo components can be soldered directly to a PCB and arranged to achieve low cost linear and rotary motion [32], which may provide a means to achieve scalable distributed actuation over larger surface areas and stroke lengths.

2.1.3 Hydraulic

Figure 2-3-A shows a hydraulically driven 25 actuator prototype with 5mm pitch from a 2006 paper by researchers at Georgia Tech [14]. Their actuators had 50mm stroke and were able to exhibit a 1N force when driven at 20 PSI. A fundamental limitation of fluidically driven actuators is that as the array's pitch decreases in size, force decreases proportional to the bore area of each element in the array. With dead reckoning not considered a viable approach, the paper achieves closed loop control by multiplexing a high frequency signal that can be capacitively coupled to actuator pins selectively, thereby inferring their position. This method is particularly compelling for reducing the complexity and cost required to obtain feedback from each element in the array.

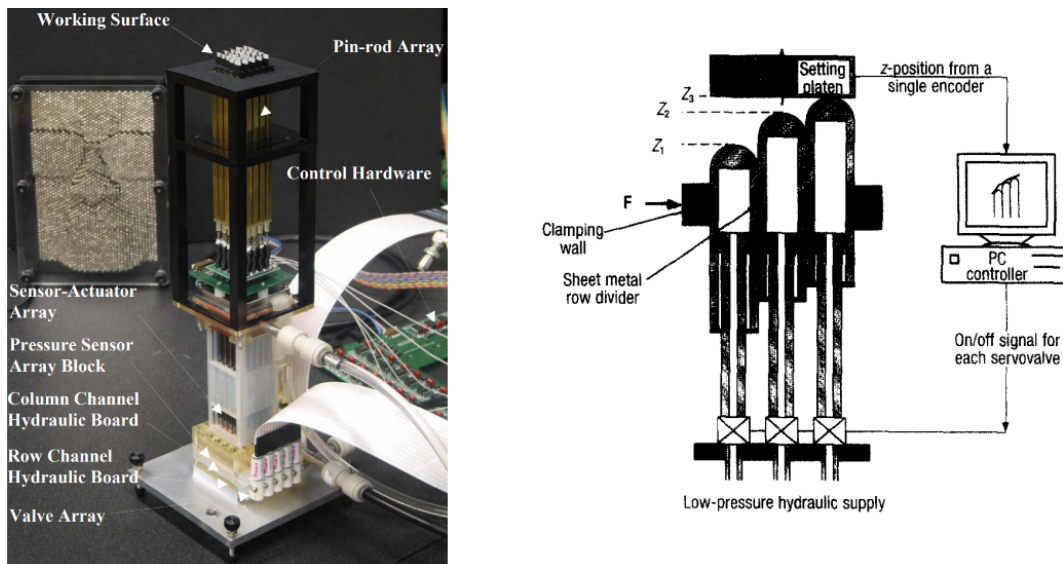


Figure 2-3: A) "Digital Clay" a 5x5 hydraulically driven actuator array for use as a tactile interface [14]. B) CAD for a platen-set actuator array intended for use in sheet metal forming [56].

On a much larger scale, a 1998 paper by Walczyk et al. outlined the design and construction of a 4x4 prototype hydraulically driven actuator array intended for use as a reconfigurable mold in stretch formed sheet metal aircraft body panels [56]. Rather than discretely controlling each actuator's vertical position, a single precision platen the size of the entire array is used as a moveable hard-stop, and each pin in the array can be driven into its desired location before pressure is removed and ultimately the entire array is clamped by an external actuator. This method effectively reduces the exponentially scaling control complexity for each actuator to a single binary valve, at the cost of the ability to move individual actuators in-situ.

2.1.4 Electric

The vast majority of distributed actuation applications are achieved not via novel actuator design, but through use of an off-the-shelf electric motor with a rotary to linear power transmission element such as a lead screw, as shown by the examples built in Figure 1-1. Some architectures aimed at reducing actuator count and complexity include a braked platen method, where a single precisely controlled motor lowers a platten which supports an array of pins, each of which includes binary clutch that can be activated to lock it in a desired position. Figure 2-4-A shows one such example, where distributed actuation is simplified to a 4x2 array of electrostatically braked pins at an impressively dense 1.7mm pitch [61]. Another simplification is to use a gantry mounted end effector to position pins independently, either by rotation of a threaded rod or through a similar locking mechanism [33].

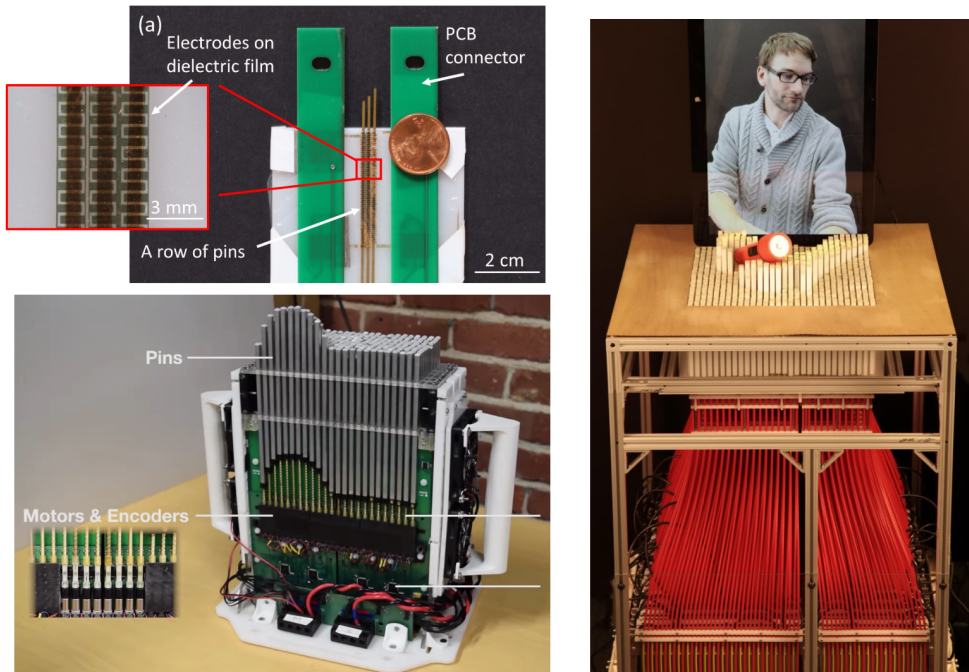


Figure 2-4: A) Stanford Shape Lab 2019 electrostatic adhesive brakes [61]. B) Stanford Shape Lab 2017 shapeShift [46]. C) Tangible Media at MIT’s inFORM from 2014 from MIT [27].

For applications requiring continuous motion, an actuator array’s pitch can be decoupled from motor size by using linkages to connect the two [27], as shown by the red cables used for inFORM in Figure 2-4-C. This prototype incorporated 900 motorized slide potentiometers in a 30x30 array, but this approach presents scaling problems as the actuator pitch becomes significantly greater than the array pitch. Another approach to addressing scaling for haptics applications shown in Figure 2-4-B, was to put a smaller denser 288 actuator array on a omnidirectional platform, which could be positioned over a larger area. With enough output force, an interpolator such as a flexible rubber sheet can be placed over a sparser array to allow for fewer total actuators, so long as the spatial frequency of information being represented allows for it [2] and [47].

Voice coils are commonly used for high precision applications such as those discussed in section 1.2.3, and are capable of achieving nanometer scale positioning over millimeters of stroke. A 2010 retrofit to the Very Large Telescope’s added 1170 el-

ement actuator array to control the secondary mirror surface to within nm position over $50\mu\text{m}$ of stroke at under 1ms rise time [3]. A similar 5352 voice coil actuator array makes up the secondary mirror of the European Extremely Large Telescope [55]. Despite their compelling resolution and linear stroke, voice coils require closed loop positional feedback, and constant current to maintain position, neither of which scale well with actuator quantity.

Electric Motor Topologies

This section includes a brief outline of rotational electric motor topologies, and their relative strengths and weaknesses as candidates for distributed actuation. Asynchronous motors such as induction motors are incapable of providing position control without some form of positional feedback. Induction motors also struggle to produce the low-end torque a permanent magnet machine is capable of, and for these reasons they were not considered a viable candidate. Commutated motors are often first placed into two categories, brushed and brushless. Brushed motors trade significant mechanical complexity for mechanical commutation via graphite brushes and a rotating armature. Like a synchronous machine, this tradeoff eliminates the ability to perform position control without feedback, and modern power electronics ICs have made electrical commutation simple and inexpensive. Commutation is later achieved via multiplexing in Chapter 4.

Switched reluctance motors (SRMs) can be electrically commutated, and rely on the reluctance torque produced by misalignment of their rotor and stator, which are both composed of soft magnetic materials. Switched reluctance machines most notably do not require permanent magnets to produce torque, which is particularly compelling for a distributed actuation application where large quantities of magnets are often expensive and difficult to assemble. To their detriment, SRMs are not capable of producing torques comparable to a permanent magnet motor at the same footprint without significantly higher power consumption [53], the justification for which is expanded on in Chapter 3. After some initial experimentation, a switched reluctance machine was not considered a viable candidate due to limited torque pro-

duction, but remains a compelling topic for future research.

This leaves a large class of permanent magnet machines, which include what are commonly referred to as brushless DC motors (BLDCs), internal permanent magnet motors, hybrid stepper motors which combine the characteristics of a BLDC and an SRM, and many more. Possibly the simplest manifestation of permanent magnet motor was ultimately what was used, which relies on torque production via the Lorentz Force created by axially oriented magnets over radially oriented windings. The following sections discuss the design of this actuator, informed by simulations conducted in Chapter 3.

2.2 Stator Design

PCB stators were popularized in the 1990s for use in hard disk drives [18], and have experienced a resurgence in recent years through commercial [9] [17] and academic applications [38] [39] [52]. They are typically constructed in an iron-less configuration, which results in lower weight, lack of cogging torque, and low eddy current losses, although these benefits are derived from the lack of soft magnetic material in the motor, and not the nature of the PCB itself. To their benefit, PCB stators enable easily manufacturable thinner axial length due to their rigidly laminated windings, and in some instances improved conductive cooling access to those windings. Perhaps most importantly, integrating motor windings with the PCB and power electronics allows for a higher degree of manufacturing customizability and precision when it comes to their windings, particular at small quantities. To their detriment, PCB motors must follow trace width and spacing design rules dictated by the PCB manufacturing process. This results in poor copper packing densities compared to their enameled wire counterparts, as well as comparatively higher ratio of wire in their end-turns, and therefore increased conductive losses. This thesis proposes the use of PCB stators to leverage the lithography industry's high throughput and quality control, allowing for reliable manufacturing of large quantities of stators in monolithic arrays. In this way, rather than a single strand of magnet wire being wound serially across each pole of

each motor, an entire array of motors can be exposed and etched simultaneously and directly into a mechanical substrate.

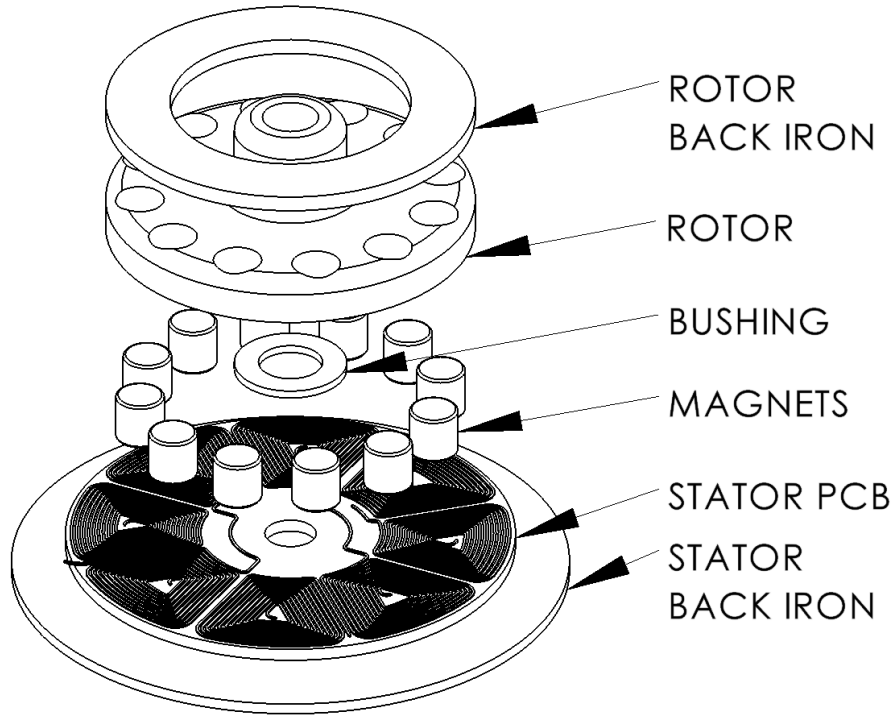


Figure 2-5: 8/12 stepper motor exploded view.

Figure 2-6 shows an axial view of the 2-phase 8-slot and 12-pole motors designed over the course of this thesis. A 2-phase design was chosen for multiplexing simplicity as discussed in Section 4.1.2, despite its lower copper utilization rate [15]. The choice of an 8/12 configuration was largely driven by desired motor diameter relative to the cost and availability of 3mm rotor magnets which fit at that footprint. The primary motivation for stator design at this stage was to maximize output torque and minimize rotor inertia and friction, the effects of which are discussed in Section 3.1. The stators were manufactured as 0.8mm thick PCBs, following 5/5 design rules on 1oz copper, resulting in 0.127mm trace width, 0.127mm gaps between traces, and 0.035mm copper thickness. This results in a 17.5% copper density axially through the board, and a 50% copper density radially across the board or 8.75% volumetric fill, which is poor in comparison to the typical 40%-60% slot fill factor of a conventionally wound motor [34]. One means to overcome this limitation is with the use of a folded

flex PCB, which has been used to demonstrate 75% axial copper density by folding and laminating 2 layer flex PCBs with a thinner polyamide dielectric substrate [?]. Sam Calisch wrote a PhD thesis at the CBA describing a method for plotting windings with a tangentially rotating tool head that precisely lays out thin gauge magnet wire [?]. This approach allows for high copper densities while maintaining a thin wire gauge, although comes at a higher manufacturing cost and time.

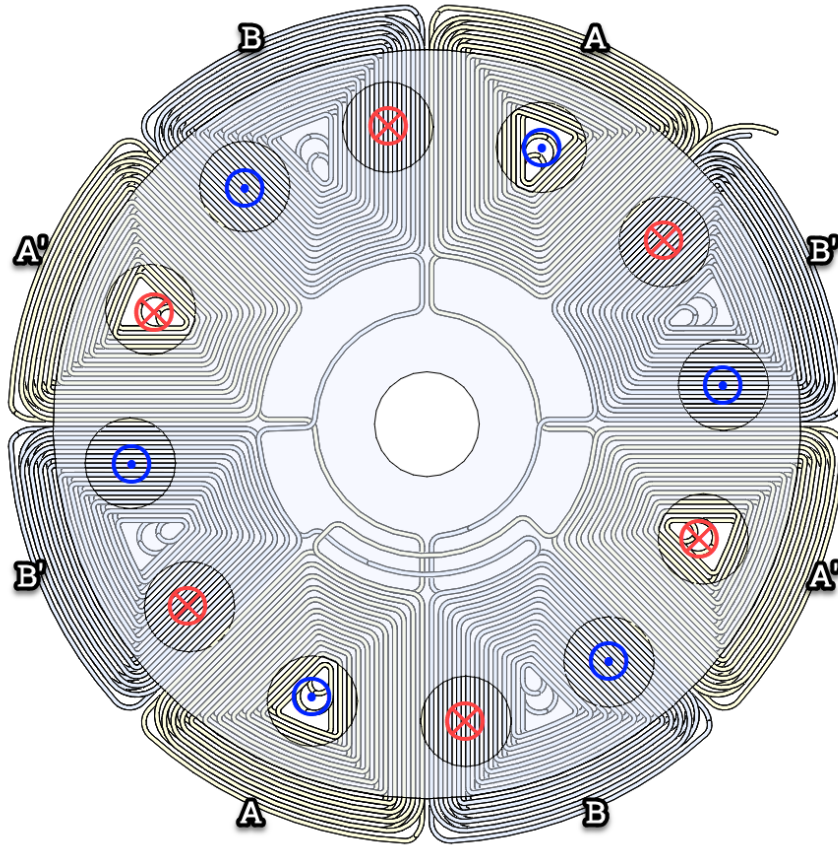


Figure 2-6: Motor top view showing A and B phase windings and connections, as well as magnet orientation in red and blue.

For the windings shown in Figure 2-6, phase resistance and inductance came to 19.5Ω , and $0.5mH$ respectively, as measured with a bench top LCR meter. By moving to a larger trace width, slot fill factor could be increased, but this comes at the expense of reducing phase resistance and inductance, and therefore a lower torque constant. Moving to a thinner PCB with higher layer density, would result in a more

substantial increase in power density, as the slot fill factor is particularly poor in this axis. Maintaining a high torque constant is particularly important for distributed actuation, where high current consumption at each motor would result in increased ohmic losses, and make powering a larger multiplexed array challenging [15].

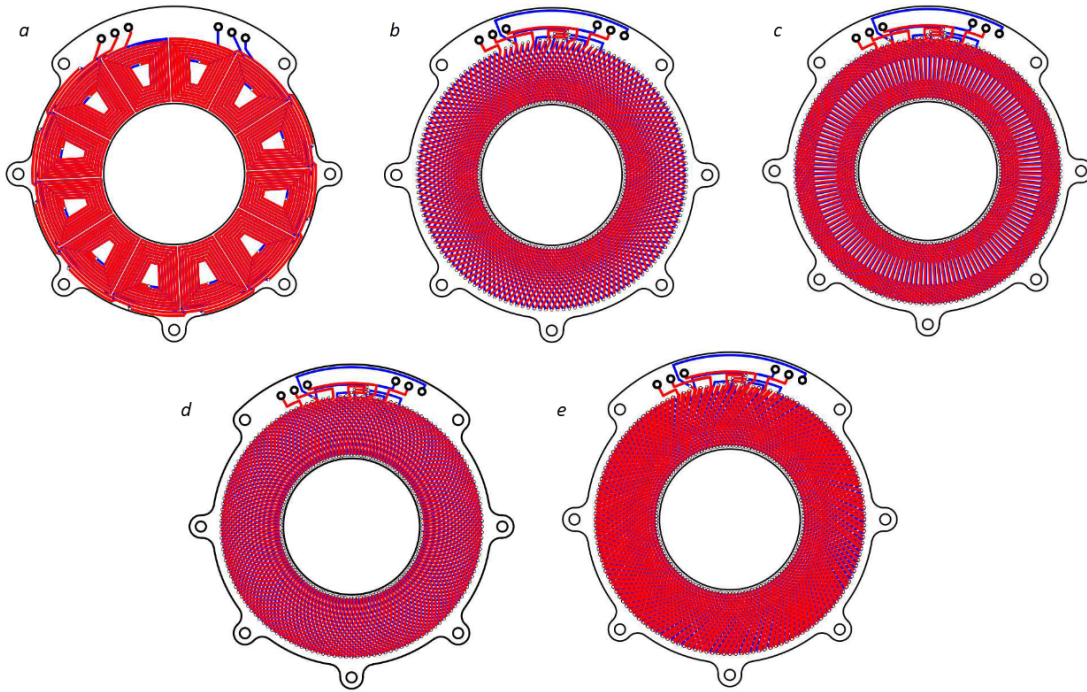


Figure 2-7: Axial flux winding topologies: a) Concentric, b) Parallel, c) Radial, d) Arc, e) Unequal width parallel [52].

A variety of axial flux winding topologies exist and are shown in Figure 2-7. Concentric windings were ultimately chosen, which prioritize copper density over maintaining radial winding direction. Maintaining radial windings in the active regions bisecting rotor magnets maximizes the portion of Lorentz force contributing to torque in the motor. This tradeoff is investigated in Section 3.1, where it is found that between 95% and 99% of force created in this design’s concentric windings contribute to torque, depending on commutation angle. In comparison, for motors with a large radial winding length, winding spacing increases with distance from the inner winding diameter, and therefore slot fill factor decreases. In their study, Tokgöz et al. found that with all else held equal across the topologies shown in Figure 2-7, concentric and

radial windings resulted in the highest torques of $175mN$ and $178mN$ respectively [52]. To their detriment, concentric windings also resulted in the lowest efficiency, due to their increased length of end-turns which do not contribute to torque production via the Lorentz Force equation (3.1). The current design shown in Figure 2-6 would benefit from an improved winding form factor, to better bisect the rotor magnets at the start of commutation. Additional vias could be used to reduce the length of end turns, but an effort was made to minimize via usage, which represent a serial process in PCB fabrication without a dedicated drill bank. There are likely many more improvements to make to better balance of efficiency, footprint, and torque production.

A complete view of the stator and rotor assembly can be found in Chapter 5, Figure 4-2. A steel back-iron is included in the final design, which is separated by an FR-4 kapton spacer acting as a dielectric and also to minimize the friction axial attractive force between the rotor and the stator back-iron. Ultimately an optimal motor layout would ensure that the winding copper stayed as close as possible to the permanent magnets in the rotor, limited by the minimum thickness of the PCB, and then depending on the torque or speed requirements of the application, space off the stator back-iron to minimize friction. There are still some open design questions left here, but a more thorough analysis of the effects of the back iron can be found in Section 3.1.3 and 4.1.5.

2.3 Rotor Design

Unlike the stator, the quantity of rotor components scales proportionally to the total number of actuators required for a given application. To mitigate the effects of this unfavorable scaling, prioritization was placed on minimizing cost and manufacturing complexity of the rotor assembly. For prototyping, each rotor consists of a 3D printed housing for 12 neodymium permanent magnets arranged in alternating polarity. An ideal design would likely replace this housing with a single stamped sheet metal part, incorporating the housing, bushing, and back iron into a single part. A small

diameter greased steel washer acts as an axial and rotational bushing, although for applications requiring increased torque and efficiency a rolling element bearing could be used instead. To decrease the effective frictional moment arm applied to the rotor, it becomes desirable to minimize this bushing diameter. To that end, an M3 washer with a $7mm$ outer diameter was used, although a smaller diameter is likely allowable without compromising the axial stability of the rotor, and could ultimately be incorporated into the body of the rotor itself. To provide linear motion, a 50mm M3x0.5 hex head bolt is threaded through the housing, which is held rotationally captive by another 3D printed guide at the base of the motors, the details of which are discussed later in Section 4.1.1.

Minimizing the rotational inertia of the rotor was found to be a critical parameter to ensure fast rotor acceleration and therefore an acceptable top speed when multiplexing through the array. Figure 2-8 shows each of the components used in the final prototype. The washer was not included in this analysis because, unlike the screw, it does not rotate or contributed a gravitational force. The magnet's inertial contribution was found with I_{mass} from equations 2.1, where each other components contribution was found with $I_{cylinder}$.

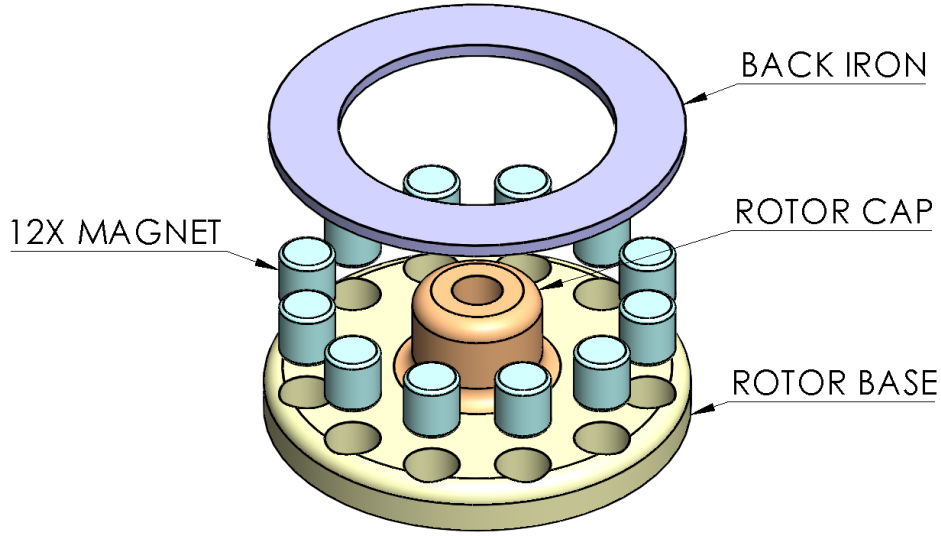


Figure 2-8: Rotor exploded view showing the components used for the rotational inertia calculations in Table 2.1.

The back-iron acts as the largest individual contributor to rotational inertia, with 45.33% of the total, as shown in Table 2.1. For this prototype it was required to ensure the magnets were not able to slip out of the 3D printed base, although through simulations described in Section 3.1.3 it is estimated to increase torque by only 18%. These results suggest that for optimal rotor speed and acceleration, the back-iron is a hinderance, but that it does contribute to increase torque production by improving the effective magnet circuit between the rotor and the stator. The results of Table 2.1 are ultimately used in a discrete time simulation found later in Section 4.1.5.

$$I_{cylinder} = \frac{1}{2}m(r_i^2 + r_o^2) \qquad I_{mass} = \frac{1}{2}mr_c^2 \qquad (2.1)$$

Magnet geometry was selected primarily based upon the availability of inexpensive $3mm \times 3mm$ cylindrical Neodymium magnets. The use of axially magnetized segmented arc magnets would drastically increase the cross section of motor windings contributing to Lorentz force production, but these are not as readily available direct

Contributor	Mass [g]	r_i [mm]	r_o [mm]	r_c [mm]	I [kgm ²]	%
Rotor Base	0.93	2.75	10.75	-	5.72e-7	21.16%
Rotor Cap	0.17	2.75	7.0	-	4.83e-9	1.79%
Back Iron	1.30	7.5	11.5	-	1.23e-7	45.33%
Magnets	1.90	-	-	9.50	8.57e-8	31.72%
Screw	2.40	-	-	-	-	-
Total	7.00				2.70e-7	100%

Table 2.1: Rotational inertias of each component in the rotor.

to consumers. As discussed in Chapter 3, magnet field strength diminishes quadratically with distance, and therefore for certain applications, it may become desirable sacrifice thickness (and therefore field strength) for a decrease in cost and rotational inertia.

Figure 2-9 shows a custom jig for stamping magnets in alternating polarity. It could be loaded with up to 192 individual magnets, and then will press 12 into a rotor base simultaneously. As an alternative to using individual magnets, Section ?? discusses the design of a jig for magnetizing custom multi-pole ring magnets, which would yield much higher air gap flux and improved manufacturability.

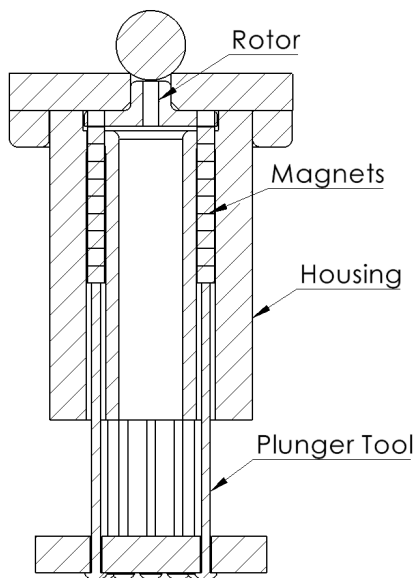


Figure 2-9: Rotor stamping jig and section view

Chapter 3

Motor Modeling and Characterization

The motor described in Chapter 2 can be thought of as subset of ironless axial flux motors, for which torque production can be modeled succinctly via its Lorentz force production, expressed in equation 3.1. In this case Lorentz force is produced by the interaction of flux produced by the rotor's permanent magnets \vec{B} through each conductor in the stator carrying current \vec{J} , with charge q and velocity \vec{v} . In the context of an axial flux motor, Figure 3-1 shows representations of these vectors, and the resultant force which is directed following the right hand rule.

$$\vec{f} = q(E + \vec{v} \times \vec{B}) = \vec{J} \times \vec{B} \quad (3.1)$$

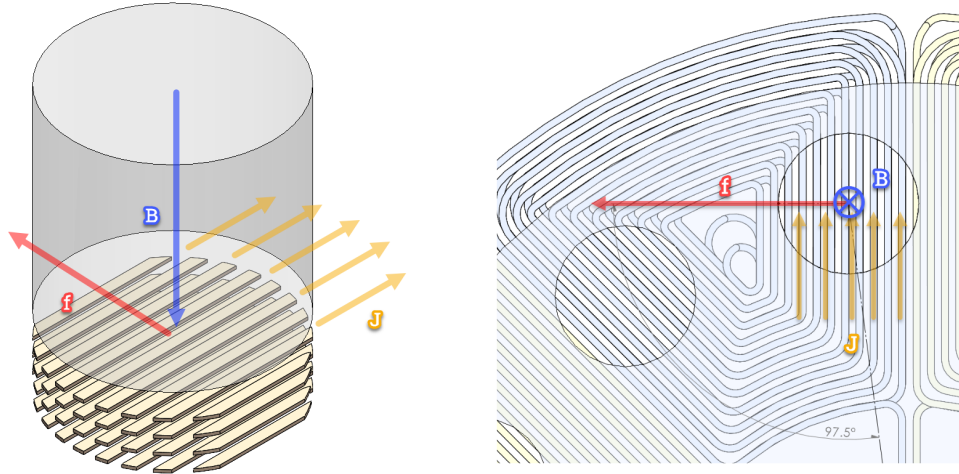


Figure 3-1: A) Lorentz force \vec{f} produced by current \vec{J} and field \vec{B} . B) Top down view of the windings exposed to \vec{B} .

With this representation, we can focus the majority of our electromagnetic modeling efforts on representing the magnetic field \vec{B} produced by the permanent magnets in the rotor, where finding force via winding current is comparatively simple. Section 3.1 provides an outline for three different methods of modeling the magnetic fields produced by a single rotor magnet, and in the case of Sections 3.1.2 and 3.1.3, the comparatively small contributions from the stator windings are modeled as well. Each of these sections will approximate force for a single magnet and phase interaction. In Section 3.2 these forces used to provide estimates for motor torque produced by the entire motor.

3.1 Modeling Flux Density

In this section, three different approaches to modeling magnetic fields are taken, including a magnetic circuit model in Section 3.1.1, a volume integral method in Section 3.1.2, and finally these results are compared to a 2D FEA simulation in Section 3.1.3. Note that the final two models are 2D simplifications, and so most notably assume a $3mm$ cube magnet rather than the actual $3mm$ length by $3mm$ diameter cylindrical magnets used. A compensation factor is applied in Section 3.2,

to correct for this difference.

3.1.1 Magnetic Circuit Model

One common approach to finding \vec{B} is to construct a magnetic circuit model, in which magnetic flux through materials of variable reluctance can be considered analogous to current flow through a resistor network [15]. The basis for this model is outlined in figure 3-2, which simplifies the rotor back iron, magnet, stator PCB, stator dielectric, and stator back iron into a simple magnetic circuit.

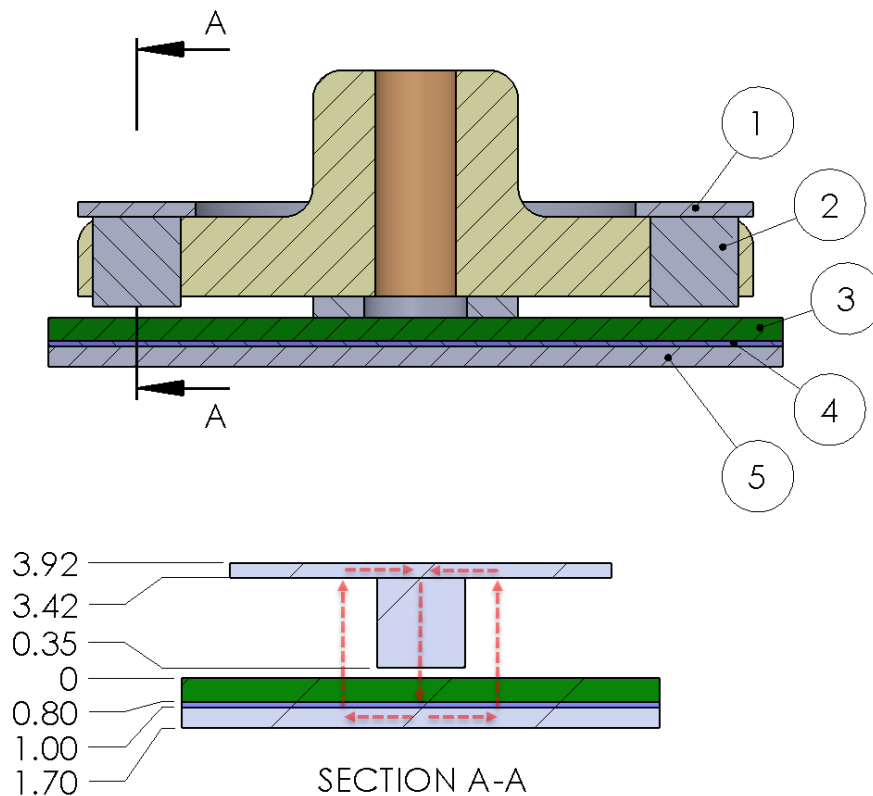


Figure 3-2: A) Cross section of the stator and rotor showing the orientation of section view A, as well as materials: (1) Rotor Back Iron, (2) Magnet, (3) Stator PCB, (4) Stator Dielectric, (5) Stator Back Iron. B) Section view of a single rotor magnet used as the final magnetic circuit model.

The resultant schematic representation is shown in Figure 3-3, where dimensions correspond to length of a magnetic circuit element in Table 3.1. Because they are all

of equal permeability and in series with one other, the 0.35mm air gap, stator PCB, and stator dielectric were all lumped into a single reluctance with length 1.35mm, called air gap. Areas were found by taking the cross sectional area of an element normal to the arrows shown in Figure 3-2-B. For the magnet and air gap, this was the area of a 3mm diameter circle. For the stator back iron this was the product of material thickness taken from Figure 3-2, and an assumed 4mm depth into the page.

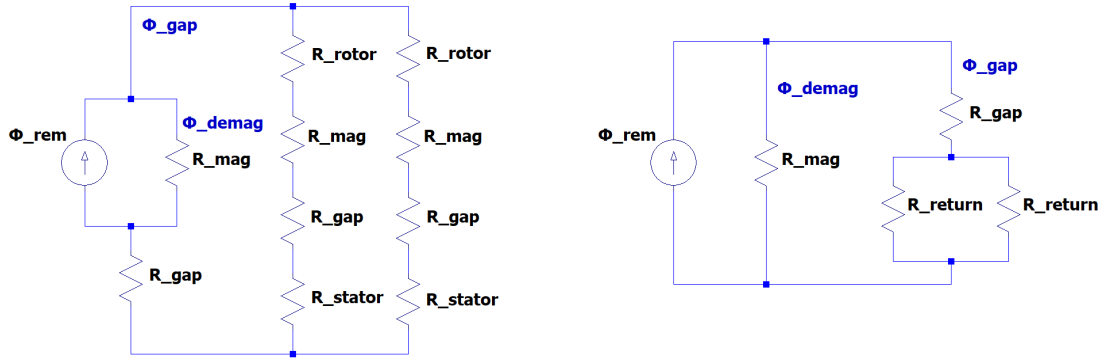


Figure 3-3: A) Schematic representation of the magnetic circuit established in Section 3-2. B) Simplification combining each flux return path into a single reluctance.

The goal of this model is to solve for the portion of total flux ϕ_{remn} flowing through the air gap as ϕ_{gap} , which we can then divide by air gap area to find the magnitude of \vec{B} . The two parallel flux return paths can be simplified as a single reluctance $\mathcal{R}_{return} = \mathcal{R}_r + \mathcal{R}_s + \mathcal{R}_m + \mathcal{R}_g$, which is schematically represented in Figure 3-3. Finally Kirchhoff's Current Law is used to find the flux represented by equation 3.2.

$$\phi_{gap} = \phi_{demag} \frac{\mathcal{R}_{gap} + \mathcal{R}_{return}/2}{(\mathcal{R}_{gap} + \mathcal{R}_{return}/2)\mathcal{R}_{mag}} \quad (3.2)$$

The final reluctance contributions can be found in Table 3.1, where the permeability of free space $\mu_0 = 1.26 \times 10^{-6}$ was used for the magnet and air gap, and $\mu_{steel} = 1.24 \times 10^{-4}$ was used for the rotor and stator back irons. The magnet acts as the single largest contributor to reluctance in the circuit, followed by the air gap

Contributor	Area [mm^2]	Length [mm]	Reluctance [H^{-1}]	% Total
Rotor Back Iron	2.00	3	1.19E+07	2.30%
Stator Back Iron	2.80	3	8.50E+06	1.64%
Magnet	7.07	3.07	3.46E+08	66.72%
Airgap	7.07	1.35	1.52E+08	29.34%

Table 3.1: Magnetic circuit reluctances

which is considerably larger than a normal air gap due to the lack of iron pole pieces, a tradeoff that is explored further in Section 3.1.3. Finally, by substituting these values into equation 3.2, with a remnant flux of $1.35T$ for an N42 neodymium magnet [49], across $7.07mm^2$ surface area, we obtain an air gap flux density of $0.617T$.

To find force over the region of windings encompassed by the air gap, the Lorentz force can be re-written in equation 3.3, where \vec{J} is current density over each conductor's cross sectional area. Total conductor volume was calculated as $0.61mm^3$ from CAD, as taken by the volume of copper in Figure 3-1-A. Cross sectional area of a $1oz$ thick $6mil$ copper trace comes to $0.005334mm^2$. Therefore the force between each magnet over an active winding comes to $0.127N$, which is later applied to find total torque production in Section 3.2.

$$\vec{F} = \iiint_v \vec{f} \cdot dv = \iiint_v \vec{J} \times \vec{B} dv \quad (3.3)$$

This magnetic circuit model has limitations, namely that it uses a simplified approximation of reluctance paths and cross section areas, particularly through circuits with ample free space. It also ignores fringing effects, and wrongly assumes a uniform flux across the motor's air gap. It also assumes a single magnetic permeability, and has no means of representing saturation, which in the case of the thin cross sections of steel in the stator and rotor yokes is probable. Although the magnetic circuit model is particularly useful for understanding the parameters we can adjust to increase air gap flux density and therefore torque, the following sections will attempt to improve on some of these limitations.

3.1.2 Volume Integral Model

A primitive 2D volume integral solver was written in python to obtain a more complete and non-uniform estimation of \vec{B} across the air gap. Unlike finite element analysis, volume integrals do not require solving a complete boundary value problem, which often includes calculating field strengths across regions much larger than the areas of interest. The volume integral approach allows interactions between magnetic materials to be calculated directly, which with a sufficiently simple model can occur orders of magnitude faster than FEA, and be easily called and iterated through for optimization. In this case the solver written was neither faster nor ultimately used for optimization, but it proved to be a useful way to build intuition around magnetostatics, and achieved results comparable to those found in Sections 3.1.1 and 3.1.3.

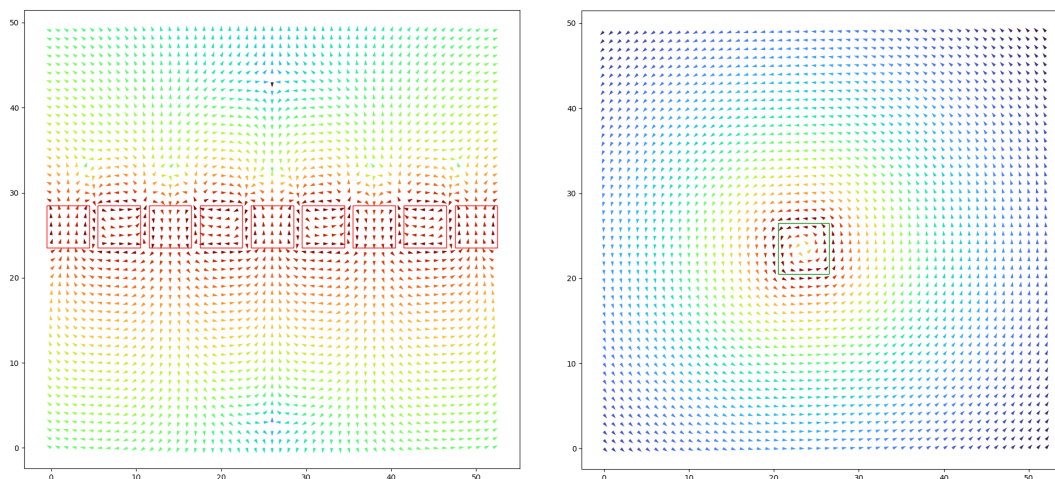


Figure 3-4: A) Halbach array simulation with strong side oriented in the $-Y$ direction. B) Rectangular cross section of a 5×5 element current carrying conductor.

First a 2D rectangular region with some integer dimensions is defined to act as the cross section for a simulation, where the number of elements dictates the spatial resolution of the problem. A command-line interface allows for sub regions of elements to be defined by an origin, height, and width, where hard magnetic materials are assigned a magnetization vector \vec{m} , and conductors are defined with a current \vec{I} , although current direction is limited to into or out of the page.

$$B(r) = \frac{\mu_0}{4\pi} \int_C \frac{I d\ell \times \hat{r}}{|r|^2} \quad (3.4)$$

$$B(r) = \frac{\mu_0}{4\pi} \frac{3\hat{r}(\hat{r} \cdot m) - m}{|r|^3} \quad (3.5)$$

The flux density around these elements can then be calculated at some point of interest via Biot–Savart for a current carrying conductor in equation 3.4, or the magnetic dipole moment via equation 3.5 for a permanent magnet. Permeability is material dependent, but in both cases is fixed at μ_0 for reasons discussed later. The vector r points from the charge or dipole source to the point of interest. In equation 3.4, I is the current flowing along a vector $d\ell$ along path C , which in our case will always be the depth of a cubic volume for which we are integrating over. In equation 3.5 we are already familiar with the magnetization vector m , although this value is typically abstracted into surface flux density by magnet vendors, and therefore not easily referenced. Instead we can find an estimate inversely, by selecting values that closely match surface flux density from FEA simulation of an equivalent magnet, and finding a value for m that results in similar magnitudes over simulated area. As \vec{r} approaches zero, Biot-Savart will converge to zero, but the magnetic dipole equation is only an approximation and happens to diverge for this case. Therefore equation 3.5 is only valid when sufficiently far from the circulating charges at the dipole source (valid for the macro-scale distances in these simulations) and therefore cannot be used to find an element’s self contribution.

This approach has not yet addressed a way to model soft magnetic materials with permeability greater than μ_0 , which introduces additional complexity. A soft magnetic material can be modeled as a permanent magnet with initial magnetization equal to zero. With B defined via equation 3.6, it was assumed that the portion of B contributed from the material itself M , could be found from some applied magnetic field in a soft magnetic material with permeability μ , by iterating through solutions

for B and M until they converged.

$$B = \mu(H + M) \tag{3.6}$$

To that end, we now require a means to calculate self contribution. A common approach here is to switch from the magnetic dipole approximation in Equation 3.5, and instead model a magnetized material's field as resulting from a loop of current carrying wire around some macro-scale region of interest with uniform \vec{M} . This is identical to a true magnetic dipole, but with this literal interpretation we can calculate self contribution of a volume element. In 3 dimensional space these can be modeled as sheets of current traveling around the material's bounding volume, circumferential to the magnetization vector. In the case of a 2D simulation with rectangular elements like the one described in this section, these current sheets would be traveling into and out of the page with direction dictated by the right hand rule. The two sheets of current traveling in the XY plane would not produce a field in the XY plane, and can therefore be ignored, similar to the end turns of a motor winding.

Assuming that the magnetization field is uniform in our square elements, we know that the curl will be zero everywhere except the perimeters of the material where M steps to zero. Therefore \vec{J}_{bound} from equation 3.7 will be zero everywhere but along the perimeters parallel to \vec{M} as stated earlier.

$$\vec{J}_{bound} = \Delta \times \vec{M} \tag{3.7}$$

Similar to \vec{M} in the last section, there are no references for finding \vec{J}_{bound} , but we can find it through trial and error by inversely solving for it from some known field. We can then plug this bound current into the equation for the magnetic vector potential as shown in equation 3.8. Because Gauss' law states that \vec{B} is free of divergence, we can assume that the entirety of \vec{B} is composed of only the curl of the vector potential. This follows the Helmholtz decomposition which states that we

can write a vector field as the sum of the gradient of its scalar potential, Φ , for which curl is zero, and the curl of its vector potential \vec{A} , for which divergence is zero. Therefore \vec{B} can be written in Equation 3.9 as simply the curl of \vec{A} .

$$\vec{A} = \frac{\mu_0}{4\pi} \int \frac{\vec{J}_{\text{bound}}}{|r|} \quad (3.8)$$

$$\vec{B} = \nabla \times \vec{A} \quad (3.9)$$

To bring this into a Python executable format, we can integrate equation 3.8 to find the potential at some coordinates x and y , contributed from a single current sheet oriented symmetrically across the X axis crossing the origin, and extending from $y' = a$ to $y' = b$. The curl about X and Y at that point is \vec{B} , written in equations 3.10 and 3.11.

$$B_x(x,y) = \frac{-\mu_0 J}{4\pi} \left[\frac{1}{\sqrt{x^2 + (y - y')^2}} \right]_a^b \quad (3.10)$$

$$B_y(x,y) = \frac{\mu_0 J}{4\pi} \left[\frac{x}{\sqrt{x^2 + (y - y')^2} \left(y - y' + \sqrt{x^2 + (y - y')^2} \right)} \right]_a^b \quad (3.11)$$

This integration can be applied on element-by-element basis, which is necessary for materials with heterogeneous magnetization fields such as soft magnetized materials, but also be used to solve for a bulk region of uniformly magnetized material, which is computationally faster for a permanent magnet.

Unfortunately the script as written failed to converge to a solution when solving for soft magnetic materials, therefore the results from this section are for an ironless

motor. The process attempted went as follows: Step 1 is to calculate \vec{B} everywhere contributed by any permanent magnets or conductors, and store this as a baseline vector field. Step 2 is to in any soft magnetic regions, calculate the induced magnetization field $\vec{M} = \mu_{material}\vec{B}$. Step 3 is to calculate the \vec{B} field induced by this newly magnetized material as though it were a permanent magnet, and add it to the baseline field. Finally step 4 is to return to step 2 with the updated baseline field until the solutions converges.

With this limitation, Figure 3-5 shows the volume integrated vector field used to represent the magnet and winding cross section previously shown in Figure 3-1-B, but without back irons. The black arrows in the winding represent the Lorentz force unit vector. The magnet's magnetization vector was found iteratively by selecting a value for \vec{M} that produced a field closely matching the ironless FEA model shown in Figure 3-12-C. The metric used was field along the magnet's centerline, shown as the dotted black line plotted in the x-axis in Figure 3-6. Note that the permanent magnet's field dwarfs the one windings, and that peak flux in this model was suspiciously $13.43T$ along the magnet's two current sheets, which is considerably lower than in FEA.

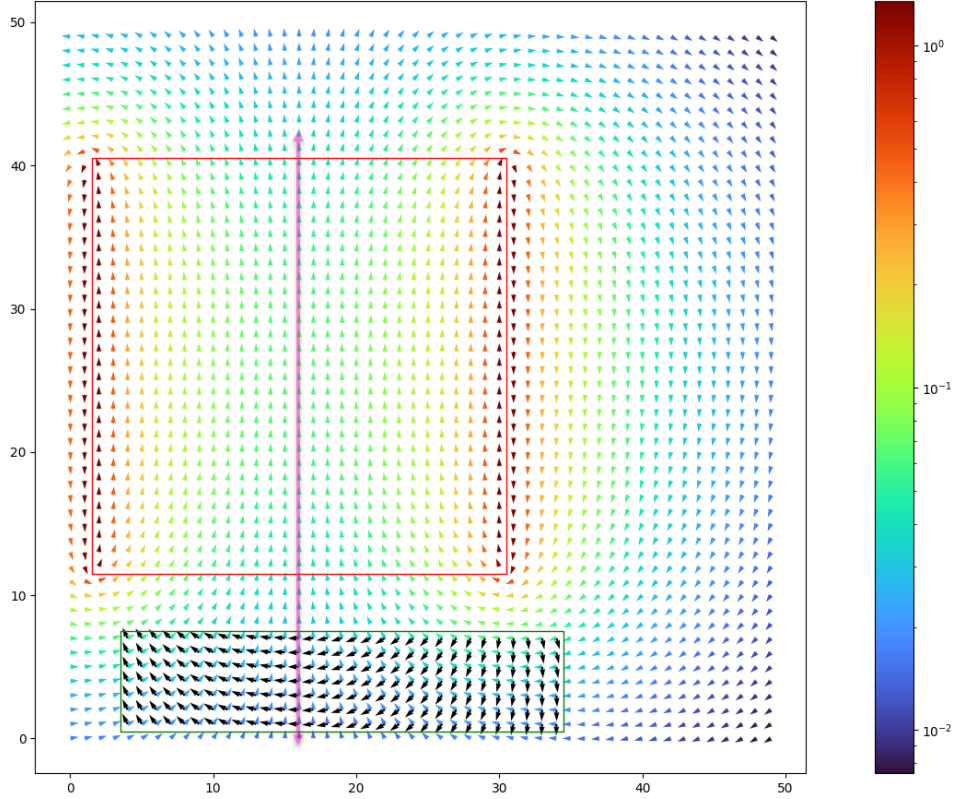


Figure 3-5: Vector field representing magnetic flux density for a motor magnet (red bounding box) and half of a winding (green bounding box). Lorentz force unit vectors are shown in black. Magnitude of \vec{B} along the pink line is plotted in Figure 3-6.

Figure 3-6 shows an average flux density in the windings of $0.22T$ along the magnet's centerline, although unlike with the magnetic circuit model, we can now account for the non uniformity of the field as shown in Figure 3-5. A complete picture of Lorentz force contributing to torque can be obtained by applying equation 3.1 to each element in the winding. With this approach we find an estimated force output of $F_x = -0.0032N$ and $F_y = -0.0012N$. These values are only $\sim 10\%$ of the ones found later using FEA in Table 3.2, although the proportion of F_x to F_y is comparable suggesting that \vec{B} is geometrically representative despite being lower across the windings as noted in Figure 3-6. Note that due to the lack of back iron are not directly comparable to those found previously in Section 3.1.1.

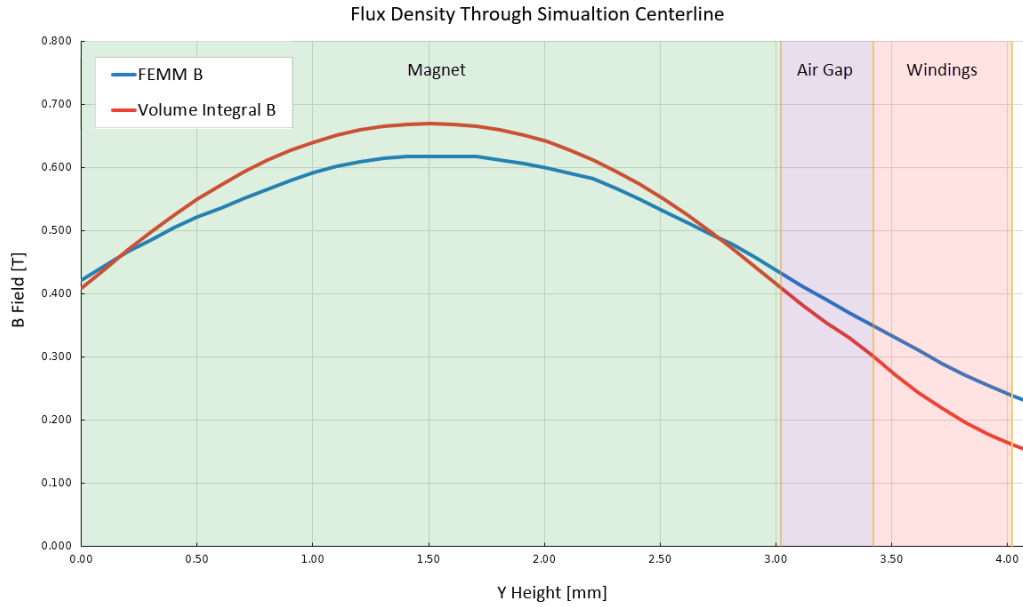


Figure 3-6: Plot of flux density magnitude through the pink arrow shown in Figure 3-5 for both the volume integral method and FEA discussed in the section 3.1.3.

Validation

An additional validation step was taken to compare the model to a known winding shown in Figure 3-7-A. The flux produced by passing 1A and 2A was measured using a TMAG5170 3-axis hall effect sensor with 100mT sensitivity and 16 bit resolution over a range of axial distances. The coils were cut from adhesive backed copper on a vinyl cutter, with 4 layers of 9 turns of equally spaced windings with a 60mm outer diameter. The test setup and results are shown in Figure 3-7.

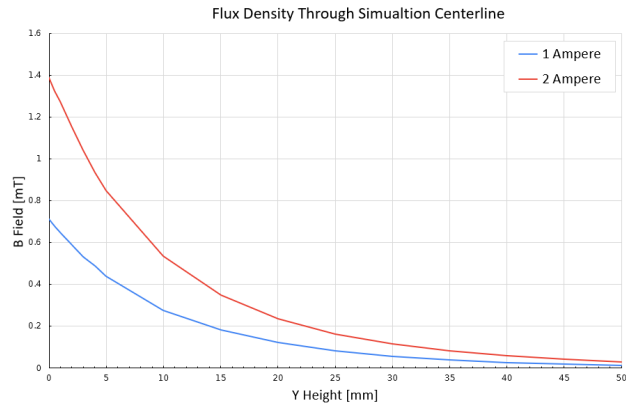
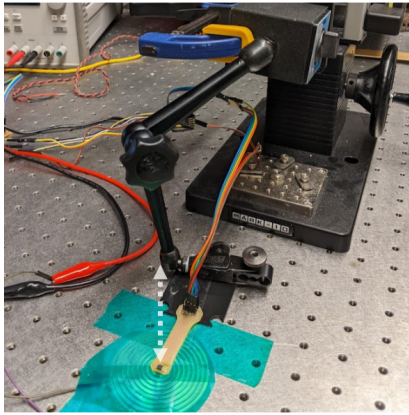


Figure 3-7: A) Measuring axial flux density relative to distance from a 36 turn, 60mm outer diameter winding. B) Plot of flux density through the white arrow shown in (A) at 1A and 2A.

Figure 3-8 shows the equivalent simulation, where each winding is shown as a green box, and assigned a current of 1A and length equal to half its location's circumference. The results differ by a factor of 6, although the inverse square relationship with distance is comparable along with the linear current relationship. The numerical error could possibly be attributed to the zero point for the validation step being imprecise, or more likely the geometric inaccuracies with the simulation, particularly attributing the correct circumference to winding location as dl .

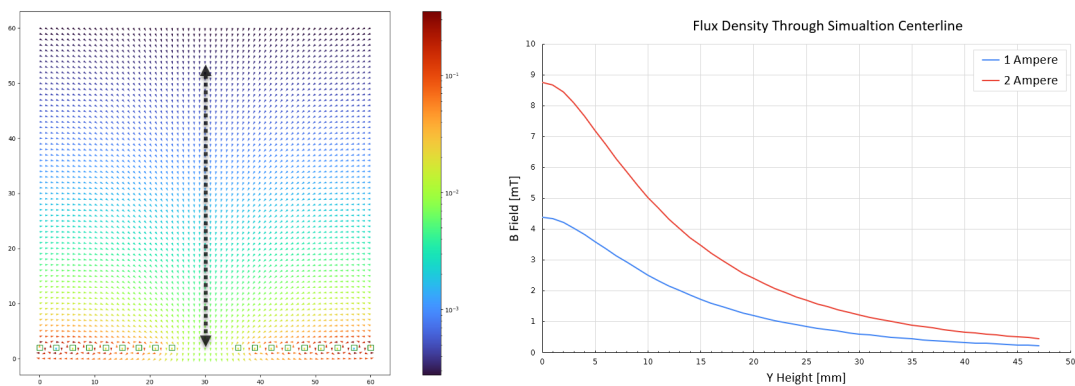


Figure 3-8: A) Vector field of a center cross section of the coil shown in Figure 3-7-A. B) Plot of flux density through the black arrow shown in (A) at 1A and 2A.

3.1.3 Finite Element Model

FEMM is an open source 2D Finite Element Analysis tool that is commonly used for electromagnetic simulation in academia and industry. In this section a FEMM model is constructed with a cross section identical to the one established in Figure 3-2. For planar simulations, FEMM does not account for depth into and out of the page (+/- Z) when calculating flux density, but does scale force outputs linearly with depth, which in this case was set to $3mm$. A baseline model representative of the current motor is shown in Figure 3-11 which will be used to find \vec{B} and output force. The FEMM manual encourages calculation of Lorentz force when applied to materials with permeability equal to μ_0 [31], and so both F_x and the smaller F_y force is calculated this way by integrating over the stator windings. The normal force in the Y direction produced by attraction of the magnet to the stator back iron is found via the weighted stress tensor.

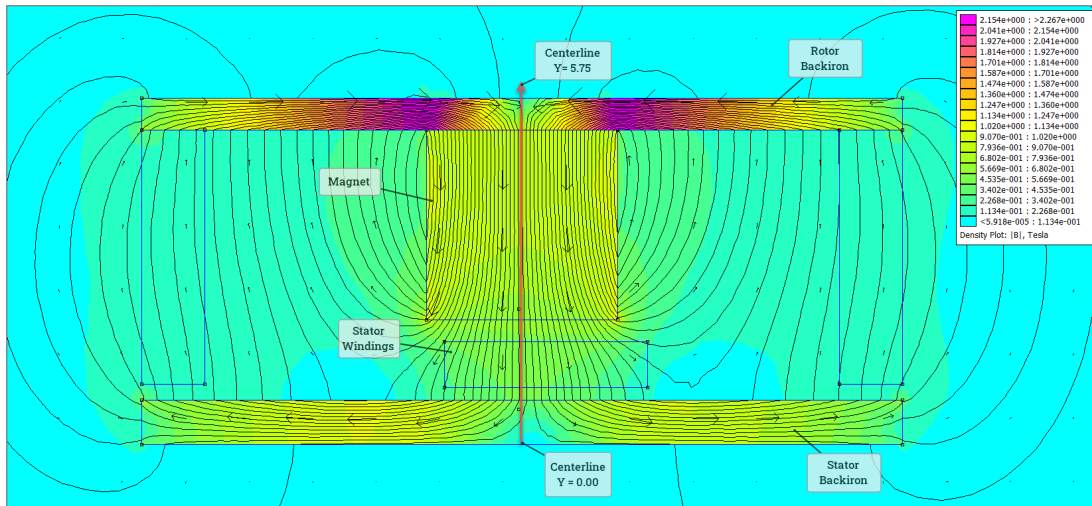


Figure 3-9: Simulation of \vec{B} cross section of magnet and half of a stator winding

The simulation uses an N42 magnetic material with magnetization vector oriented in -Y. The windings are attributed 35 turns and $1.8A$. All geometries and orientations were taken directly from CAD as shown in Figure 2-6, with rotor angle set to the start of commutation. The simulation uses the BH curve for hot rolled low-carbon steel as shown in Figure 3-10, where complete saturation occurs at roughly $2T$. The

motor as designed has a simulated force output of $F_x = 0.0876N$ and $F_y = 0.7879N$. These and all future force outputs are included for comparison in Table 3.2, where this baseline case is used as a point of comparison for the percent changes in columns 3 and 4.

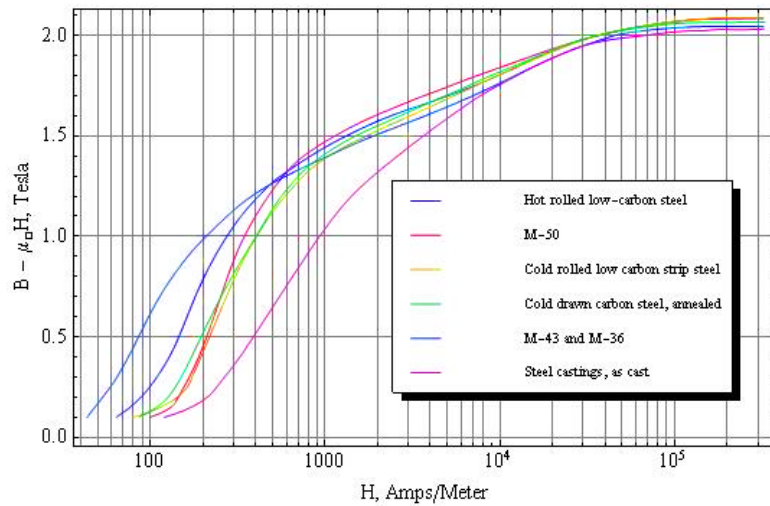


Figure 3-10: BH Curves for Hot rolled low-carbon steel, in comparison with other magnetic materials. [1]

Figure 3-11 shows an average air-gap flux of $0.55T$, which is very close to the results obtained in Section 3.1.1, although there we assumed this flux was uniform axially through the winding which will over represent force. The steep drop off past both the stator and rotor back irons indicate that they are not overly saturated, although flux density in the rotor back iron peaks at $2.26T$, which is past the back iron's saturation point. Before considering increasing rotor back iron thickness to minimize saturation, the following sections will explore the tradeoffs associated with including it at all.

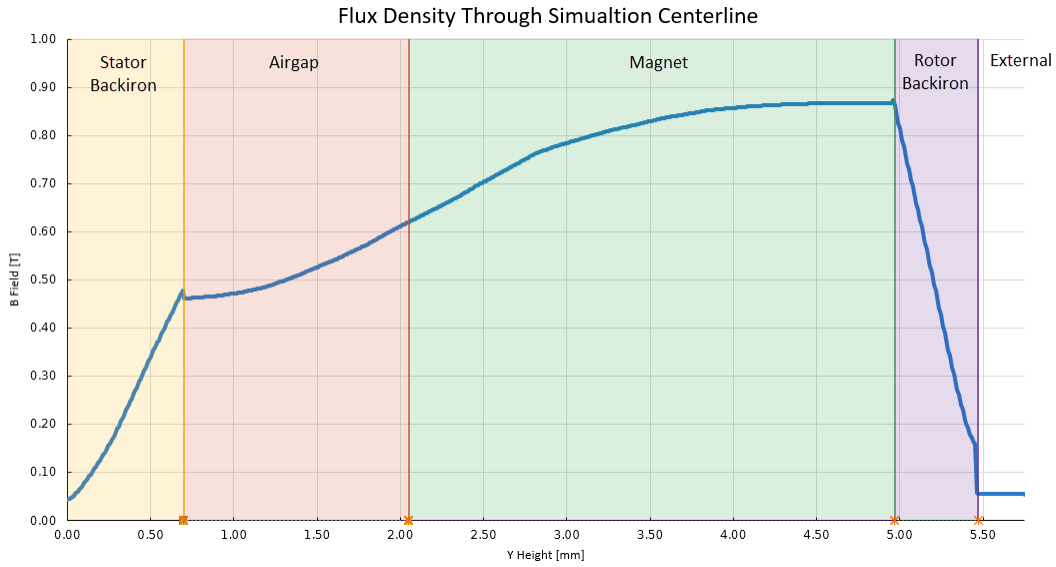


Figure 3-11: \vec{B} field as a function of distance along the red centerline shown in figure 3-9, where colored regions represent transitions between components.

Effects of Rotor and Stator Back Irons

To better evaluate motor design choices, three modifications were made to the baseline simulation, as shown in Figure 3-12, and their effects on force output and rotational inertia are plotted in Table 3.2.

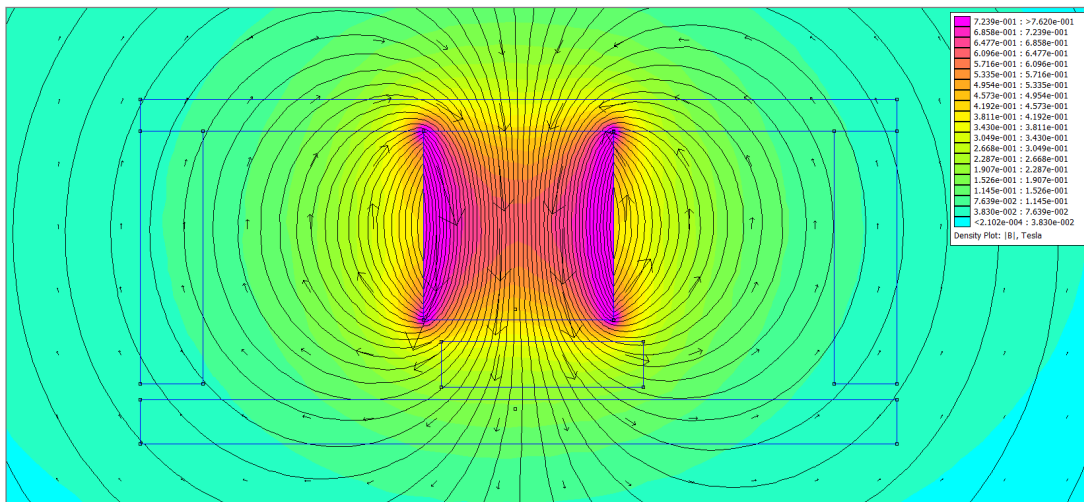
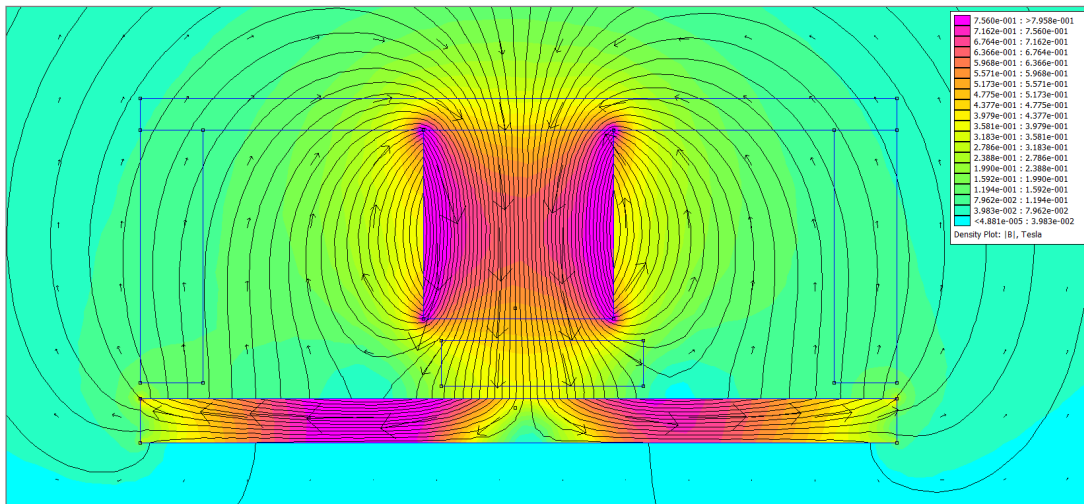
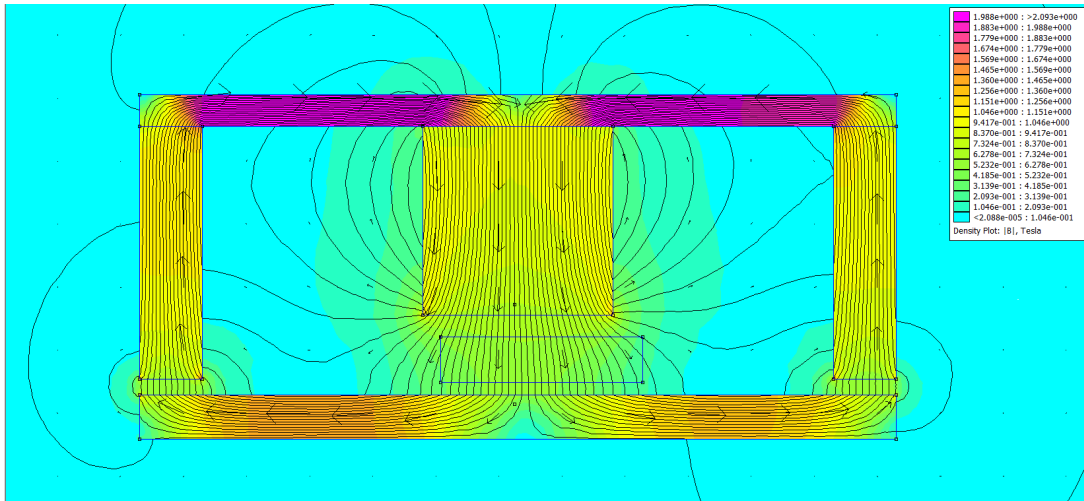


Figure 3-12: A) Rotor back iron with yoke that extends through the magnet and PCB air-gaps. B) Removing the rotor back iron. C) Removing the rotor and stator back irons.

Simulation	F_x[N]	F_y[N]	F_x%	F_y%	I%
Current Prototype (Fig. 3-9)	0.088	0.788	100%	100%	100%
Full Yoke (Fig. 3-12-A)	0.105	1.936	119%	246%	112%
No Rotor back iron (Fig. 3-12-B)	0.072	0.519	82%	66%	45%
No back irons (Fig. 3-12-C)	0.043	0.010	49%	1%	45%
Extended Stator Winding (Fig. 3-13)	0.028	0.779	32%	99%	100%

Table 3.2: Simulated X and Y force outputs, and associated effects on rotational inertia. Increasing F_x and decreasing F_y and I are considered beneficial.

As shown in Section 3.1.1, the large air-gap return path is the primary contributor to reluctance in the current motor layout. By adding narrow return path back iron on either side of the rotor, it becomes possible to yoke the magnet and significantly increase flux in the air-gap. This simulation is shown Figure 3-12-A, where forces increased to $F_x = 0.104N$ and $F_y = 1.936N$. The return path yokes were modeled as narrow and far from the magnet to incentivize flux towards crossing the stator winding air gap, and not jumping directly into the yoke. In reality, to be manufacturable, these yokes would be placed radially around the perimeter of the rotor and therefore bisect the magnet in these simulations, however this model should provide a similar representation of increased force without requiring 3D simulation. Despite the 19% increase in tangential force, the added mass and resulting increase in rotational inertia at the rotor make it likely that this change would result in slower commutation overall. The normal force F_y also increased by 146%, which is likely to outweigh the increased torque contribution in the form of increased frictional loss. For this reason we can try some further changes aimed at mitigating these effects in the sections below.

Figure 3-12-B shows the effect of removing the rotor back iron, which resulted in forces decreasing to $F_x = 0.0718N$ and $F_y = 0.5189N$. In Table 2.1, we see that the rotor back iron contributes to $\sim 45\%$ of the total rotor inertia. Including the back iron results in only a $\sim 22\%$ increase in output torque, suggesting that a motor optimized for multiplexed speed would accelerate twice as fast with the lower inertia rotor.

Figure 3-12-C, shows that there is also a tradeoff to including the stator back iron, as the normal force between it and the rotor is the primary contribution towards frictional loss during move with minimal axial load. Removing the rotor and stator back irons completely resulted in forces of $F_x = 0.0431N$ and $F_y = 0.0099N$, where the residual F_y component is likely a combination of noise and the slightly off-axis stator winding at the start of commutation. The stator back iron has no effect on rotational inertia, but this change reduces the normal force produced by the magnet to zero, which, in the absence of externally applied loads, reduces friction to negligible amounts, as well as removes the potential for eddy currents to be generated in the stator. With the high coefficient of friction associated with using a plain bearing, it is likely that this arrangement would result in the highest rotor acceleration and therefore commutation speed, despite the 51% penalty to torque.

Effects of Fringing and Return Fields

As alluded to in Section 3.1.1, the effects of fringing and return fields were previously neglected in both models. Figure 3-13 shows the effects of increasing the stator winding width to encompass a majority of the return flux traveling in the +Y from the stator back into the rotor back iron. Return inflection points where the direction of flux transitions from the -Y to +Y direction, are approximately 1mm past the magnet edges on both sides of the stator, and are shown with red arrows. Lorentz force produced by windings past these regions is acting in the opposite direction to that of the central windings. This simulation tells us two things, one is that there are diminishing returns to generating torque as the windings extend further in X, and that well past this point there are regions where the fringing fields will produce opposite the desired direction of rotation.

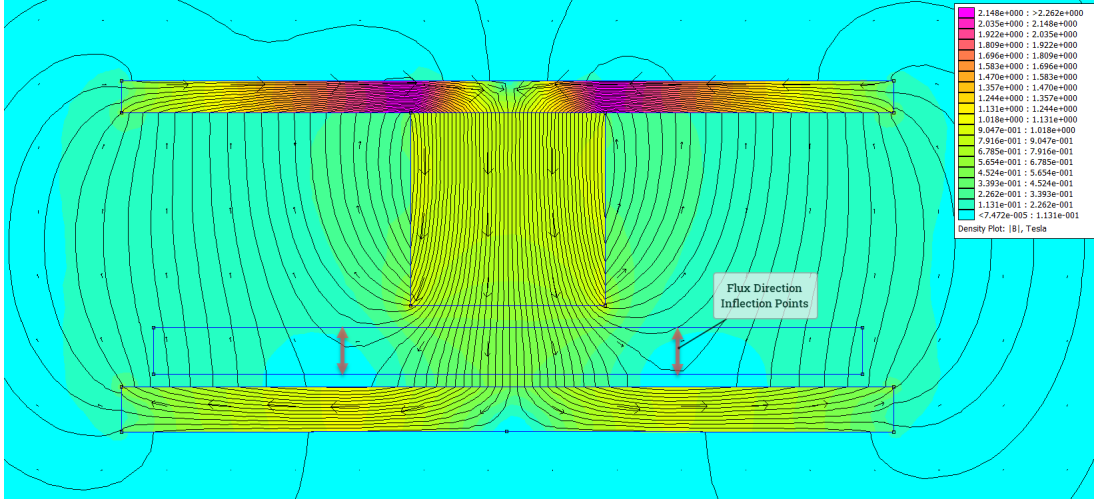


Figure 3-13: Simulation with an expanded 11mm width stator winding which encompasses the majority of the magnet’s fringing return flux and results in a reduced $F_x = 0.0279N$.

This effect is useful to note as a limit to the extension of stator windings such that they do not extend into regions of fringing return flux. This is particularly important for concentric windings, where windings traveling farther into the page in the $+/- Z$ direction in the simulation are liable to pass these regions. Fringing can also come into play during commutation, where as the rotor approaches full commutation, more of the stator winding is liable to be exposed to return flux, which results in lower output torque further from the start of a commutation cycle.

3.2 Torque Production

In each of the 3 simulation approaches we have estimated torque produced from a single magnet winding interaction. Figure 2-6 shows that for a single active phase, there are 8 such interactions which is reflected in equation 3.12, and so F_x and F_y should be multiplied by a factor of eight.

$$[H]\tau = \vec{r} \times \vec{F} = \|r\| \|F\| \sin(\theta) \quad (3.12)$$

The volume integral and FEA simulations did not account for the cylindrical nature of the magnet, and therefore their torques should account for the percent difference between the area of a square of side length d and a circle of diameter d . With $d = 3$ this scale factor is as follows: $ScaleFactor = \pi 1.5^2 / (3 \times 3) = 78.5\%$. Note that this scale factor does not need to be applied to the magnetic circuit model.

Concentric motor windings do not produce a purely tangential force vector as shown in Figure 3-1-B. The effective torque at the start of commutation follows equation 3.12, where \vec{r} is the radial vector pointing to the point of applied force \vec{F} . When evaluated for $\theta = 97.5^\circ$, we find that 99.14% of force contributes to torque. As the magnet begins to pass the 11° commutation mark and approach the full commutation angle of 15° , this loss of tangential torque producing torque increases to 94.83% at $\theta = 108.5^\circ$.

These three correction factors are applied in Table 3.2 below, where the output torques and forces for each approach can be compared. For purposes of this thesis, the FEA approach is considered the most accurate and will be referenced moving forward. The magnetic circuit model was able to provide comparable results with significantly less time invested, although is not capable of estimating normal attractive forces in F_y without referencing empirical equations. The volume integral method is significantly further from FEA, but the ratio of F_x and F_y are promisingly close, and further work will be done to improve this simulation tool.

Simulation	Back Iron	Torque [Nmm]	F_x [mN]	F_y [mN]
Magnetic Circuit	Y	20.137	-127	-
Volume Integral	Y	-	-	-
FEA	Y	10.964	-88	-788
Magnetic Circuit	N	8.566	-54	-
Volume Integral	N	0.401	-3.21	-1.211
FEA	N	5.357	-43	-10

Table 3.3: Final simulated full motor torque outputs, as well as single magnet forces.

3.3 Characterization

Establishing limits on speed and torque of these motors through empirical testing will be essential for future design iteration. Maximum motor speed is ultimately limited by the multiplexed commutation scheme outlined in Chapter 4. Taking a direct torque measurement for motors at this size is challenging due to the low output torque's proximity to frictional losses in a system. Motor output force after passing through a lead screw transmission is measured later in Figure 4-13, but unfortunately a low power dynamometer was not constructed in time to produce a proper speed torque curve for the motors designed in this thesis. Figure 3-14 shows a small electric motor dynamometer built using an 800W brushed DC motor and encoder as an absorber. Motors under test are mounted to an adaptor plate connected to a slewing ring, which is rotationally constrained by a load cell to effectively measure torque. By adapting the design to use a smaller and more sensitive absorber, this prototype could be used to test motors at the 10W scale.

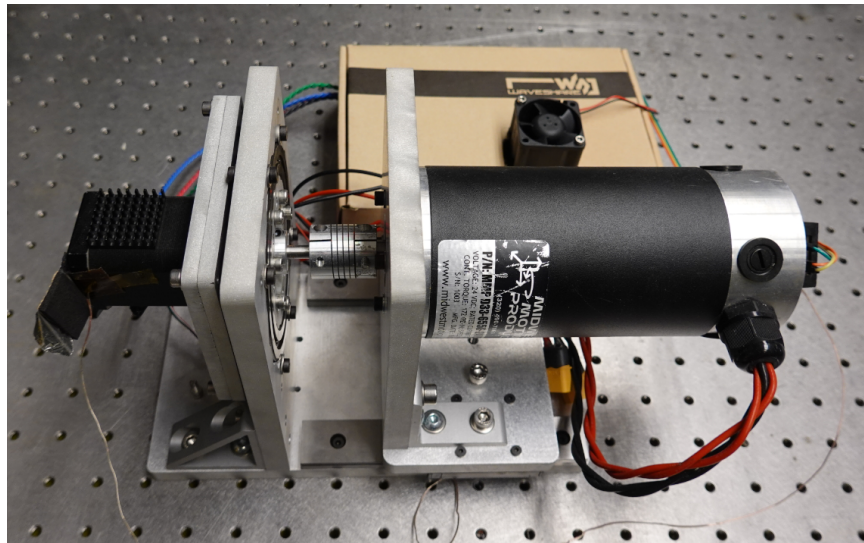


Figure 3-14: Custom dynamometer coupled to a NEMA17 stepper motor.

The dynamometer can perform automated torque-speed sweeps with efficiency data as shown in Figure 3-15, as well as a thermal sweep that reports temperature at some given current setpoint, and a saturation sweep that measures output torque as a

function of current setpoint. Together, these three sweeps can be used to determine a complete sweep of torque across speed, and if torque output is thermally or saturation limited.

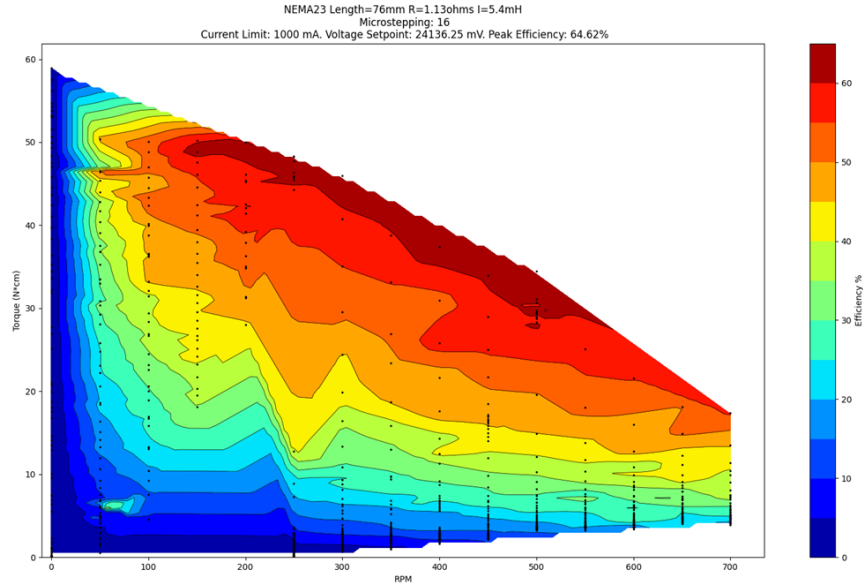


Figure 3-15: Efficiency map of a NEMA23 stepper motor generated by the custom dynamometer shown in Figure 3-14. Black dots are sample points from sweeping torque applied to the device under test at a given speed. The color overlay is interpolation of efficiency equal to the ratio of mechanical power produced $P = \omega T$, to electrical power consumed $P = VI$.

Chapter 4

Parallel Distributed Actuation

Chapter 2 introduced the design of an axial flux permanent magnet PCB motor designed with an emphasis on scalability. This chapter will focus on integrating that actuator into an array, and rather than using a conventional stepper motor driver, multiplexing the array to improve scalability at the power electronics level.

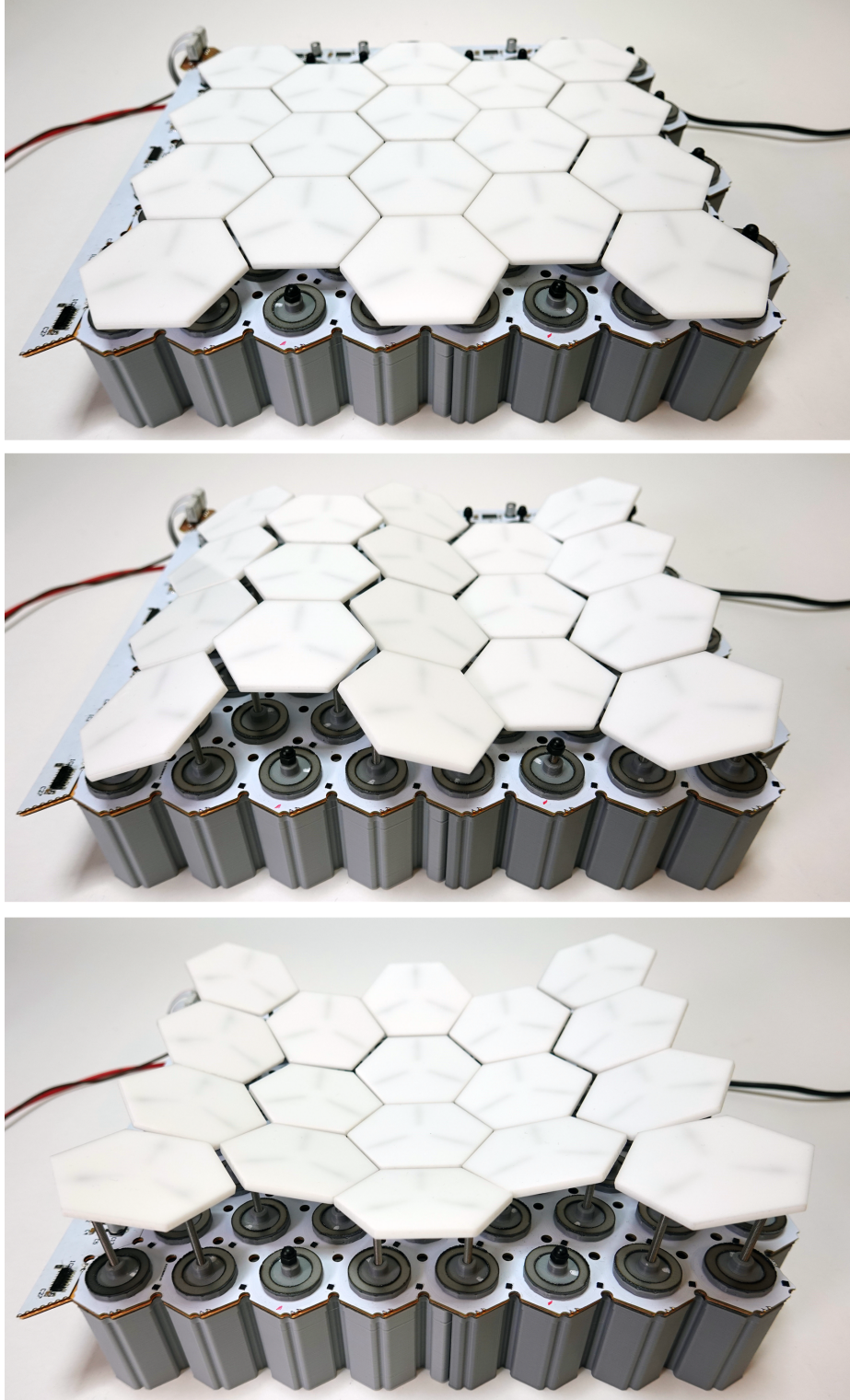


Figure 4-1: Hexagonal motors configured as: A) Plane. B) Sinusoid. C) Concave Parabola. Corresponding driving functions are shown in Figure 4-8.

4.1 Linear Motor Array

4.1.1 Mechanical Design

Figure 4-2 shows an exploded view of a cluster of three motors responsible for driving a single hexagonal interpolator. The lead screw mechanisms are simple M3x50mm hex head screws, which can move vertically corresponding to rotation of the threaded rotor. Linear stroke is dependent on screw length, where for longer stroke actuation the screw could be replaced with threaded rod of any length and a hex nut. An acorn nut threaded over the top of each screw provides a spherical interface for the kinematic canoe grooves machined into the base of each hexagon. The hex head of each screw is rotationally constrained by lobed linear guides extruded into the 3D printed base. This rotational constraint allows the rotor to act as a nut, advancing or retracting the screw, which is kept rotationally constrained. One caveat of this design is that the effective bearing distance preventing the screw from rotating about the X or Y axes is established by the clearance fit between the screw thread and mating hole in the top of the base, and the clearance fit between the screw's hex head and lobed extrusion. At max screw extension, this distance approaches zero, and non-axial play at the tip of the screw is increased.

As discussed previously, the rotor is axially constrained in the $-Z$ direction against a lubricated stainless steel washer. The rotors are only weakly constrained in the $+Z$ direction by the attraction between the rotor magnets and the stator back-iron. For low axial loads, this washer acts as an adequate bushing with an empirically estimated coefficient of friction of 0.2, with some additional expected viscous damping behavior. The smaller washer diameter reduces the effective moment arm applied to the gravitational and magnetic normal forces resisting rotation. Aside from the magnetic normal force, the screw and rotor are unconstrained in the Z axis opposing gravity, and so any axial forces pulling the rotor from the stator would result in failure. Radially the rotor is constrained by the screw bearing against the clearance hole in the base, and therefore is not capable of withstanding significant radial loads.

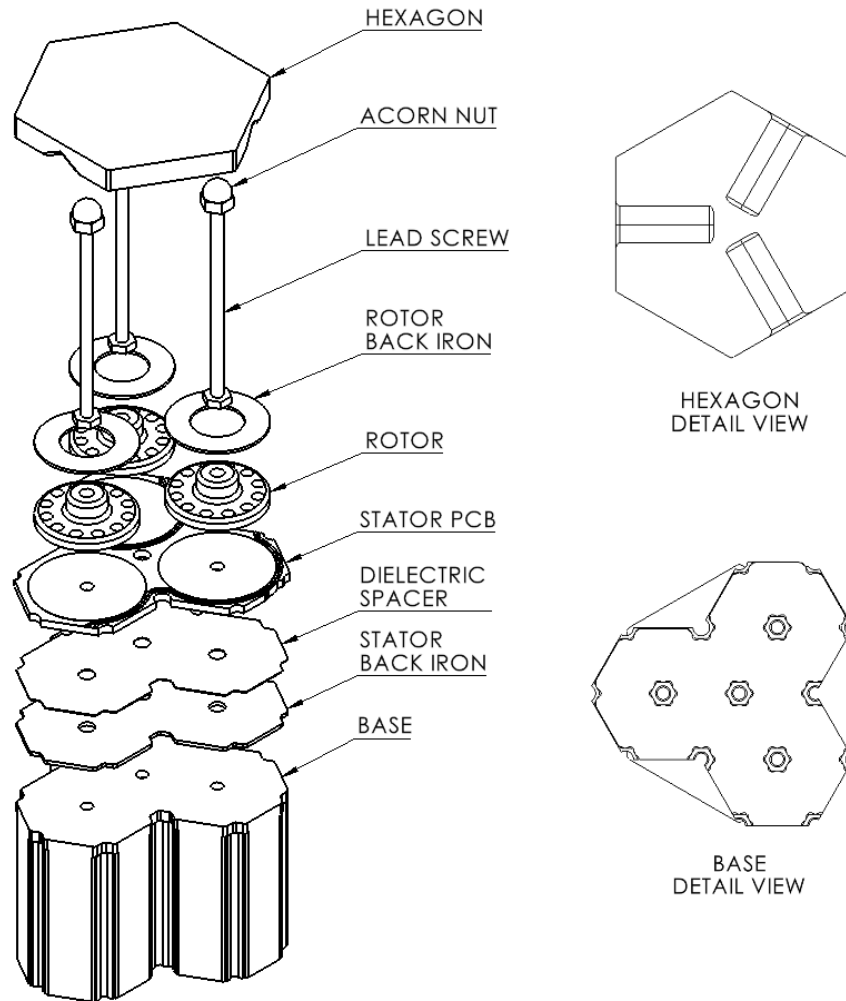


Figure 4-2: Exploded view showing a three actuator segment of the full array shown in Figure 4-1.

Rotary to Linear Motion

The 0.5mm pitch screw thread provides a high degree of mechanical reduction, which increases the linear resolution of each motor, and amplifies the mechanical advantage that the rotor has over the lead screw. Equation 4.1 can be used to calculate output force at the screw tip, where l represents the pitch of a single start screw thread, and η represents efficiency which is a function of the thread's helix angle and the coefficient of friction at the thread interface.

$$F_{out} = \frac{2\pi\eta}{l}T_{in} \quad (4.1)$$

An imperial 10-24 threaded bolt could alternatively be used at the same form factor to trade speed for torque. Screw threads also dictates the motor’s linear resolution, equal to the pitch divided by the rotational step resolution of the motor. In this case, the motors are capable of 24 steps per revolution, which results in a $20.83\mu m$ linear step resolution. Assuming repeatability between rolled thread pitch, this resolution could be expected to translate to equivalent accuracy. The tradeoff between motor resolution, force, and speed could be adjusted further with a custom threaded screw. Finally the motors do not need to expend energy when at rest due to poor back-drivability of the screw, a property that Knaian et al. resolved with electropermanent magnets [12]. This lack of back-drivability is desirable for certain subsets of applications where infrequent motion and large constant loads are placed on each motor. Back-drivability becomes desirable where proprioceptive actuation might be required, and therefore an alternative transmission mechanism.

Interpolation

One common method of interpolation between an array of motors with coarse pitch is to stretch a compliant membrane between actuators [2] [36] that interpolates the array into a continuous surface. This approach requires substantial output force from the actuators and well constrained linear actuation to resist the tensile loads in the membrane. As a lower force but still easily reconfigurable alternative, Figure 4-2 shows an array of hexagonal lasercut tiles, each with three machined canoe grooves to act as kinematic couplings interfacing with the acorn nuts on a corresponding set of three linear actuators. With this arrangement the two rotational degrees of freedom θ_x and θ_y for each tile can be adjusted, as well as its Z translation. Each tile is currently constrained against the tips of the three actuators by gravity, but magnets or flexures with a fastener could also be used to resist normal loads.

An alternative approach shown in Figure 4-3 uses a continuous origami skin that was manufactured on a Zund flatbed tangential cutting and creasing tool from Pyralux flex-PCB material. This design can be used to create electrical continuity across the surface of the array, allowing for hybrid integration of higher resolution, short stroke actuators such as piezoelectrics [8], or geometrically reconfigurable PCB assemblies. Two prototypes were made, Figure 4-3-A is underactuated, using a single actuator per hexagon, leaving the two rotational degrees of freedom to be resolved by the stiffness of the connecting elements and height of adjacent hexagons. This approach allows for higher hexagon pitch, but lower overall precision. Figure 4-3-B shows an approach similar to the discrete hexagonal tiles with three actuators per hexagon. A steel lasercut stiffener is laminated to each hexagon, but rigid-flex PCBs would be a more viable alternative for future prototypes. Both designs are coupled to the stiffener using ball magnets which attach to the ferritic M3 screw of each linear actuator.

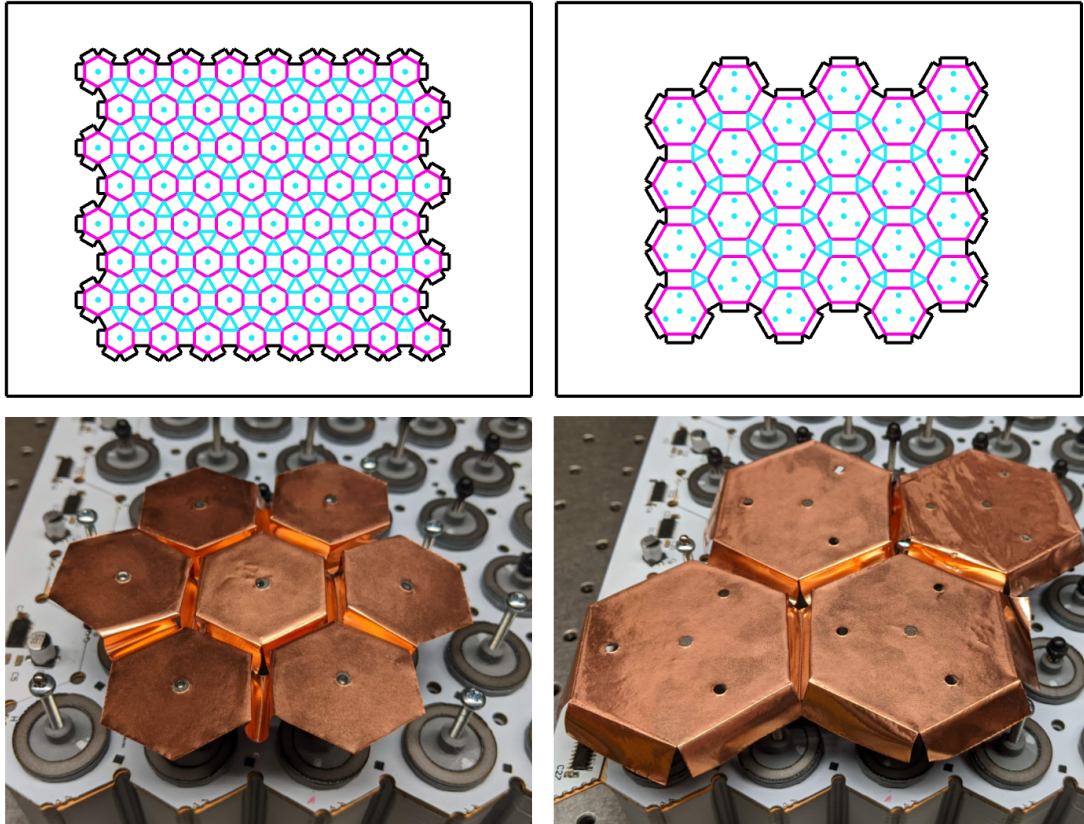


Figure 4-3: Flat patterns for origami interpolators and their folded counterparts. Black lines represent perimeter cuts, blue lines represent interior cuts, and pink lines represent creases. A), C) Single actuator per hexagon. B), D) Three actuators per hexagon.

4.1.2 Electrical Design

To drive large arrays of motors, motor power is multiplexed throughout a diode protected array of windings, as shown in Figures 4-4 and 4-5. In this way, $N \times M$ actuators can be controlled with only $N+M$ drivers, with the limitation that only a single row or column of motors can be energized at a single time. This approach reduces the quadratic scaling for drivers required as N and M become large. For example, a 100×100 actuator array might require 10,000 discrete driver ICs and their associated discrete components, where as this multiplexed approach requires only 200.

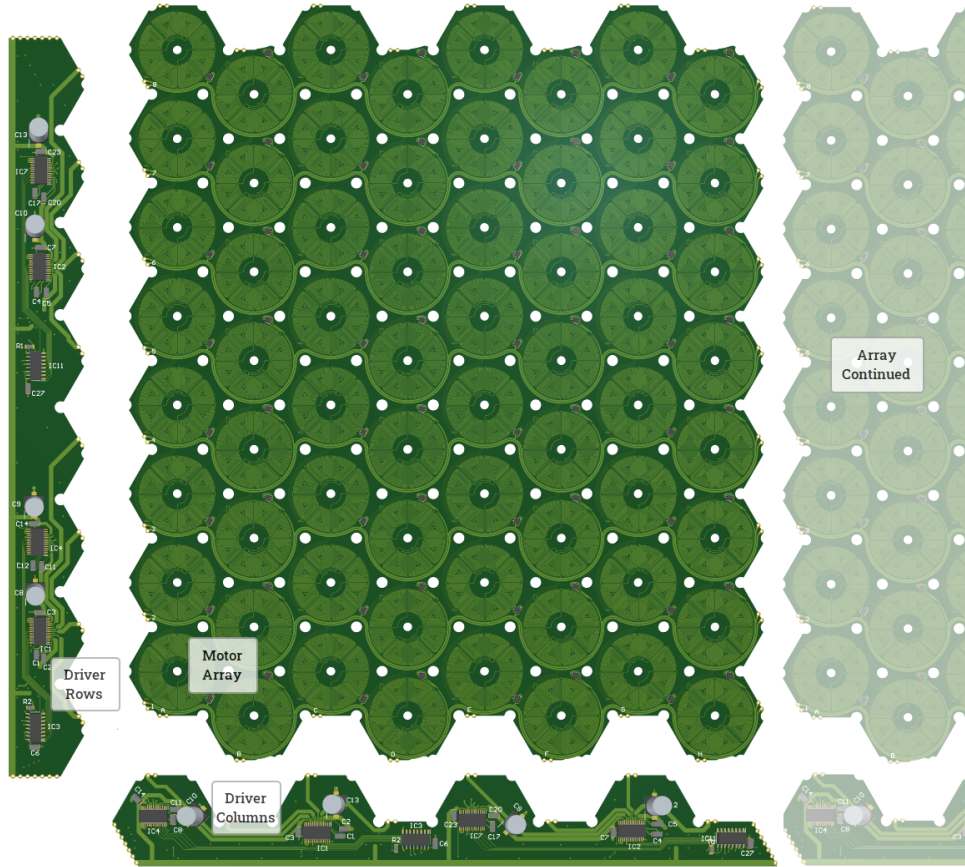


Figure 4-4: Motor array with row and column driver PCBs

Figure 4-4 shows a full 8x8 PCB motor array, with its associated row and column drivers. Castellated edges are used instead of connectors to allow power transmission between these boards. This allows for the row and column driver boards to be soldered directly to an motor module, and these 8x8 motor modules can then be tiled to form larger arrays in multiples of eight. Holes were also left in the spaces between circular motor windings, which allow for denser linear actuation by stacking three layers of boards on top of each other with a 9, 24mm offset in the +X direction. This arrangement decreases the hexagonal pitch of the array from 32mm to 18.5mm.

Four independently enabled quad 1/2 bridge driver ICs capable of supplying 2.5A at $VDD = 60V$ are used for each row and column driver PCB. Each row and each column is assigned two 1/2 bridges, which allows any phase termination to be tristated to either VDD, ground, or be left floating. In this way current can be passed selectively

between nodes in the array, but to prevent current from passing through adjacent windings, two blocking diodes are required for each phase. These blocking diodes can be seen in Figure 4-5, and rather than using four discrete diodes at each motor, an inexpensive full bridge rectifier can reduce the number of components to a single IC, which use Schottky diodes for a minimal forward voltage drop.

The row and column driver circuits can be controlled simultaneously from a single low-power microcontroller, although for prototyping simplicity a Teensy 4.0 was used. Each row and column driver is assigned a seven conductor bus, including ground and motor power, which are bussed along the perimeter of the boards. Two channel inputs dictating the high or low state for a 1/2 bridge are shared for all of the row and column A phases (top and left rows and columns respectively), and all of the row and column B phases (bottom and right rows and columns respectively). With this approach, simultaneous commutation for an entire row or column must share aligned phases. Finally, three conductors are dedicated to the control of a cascading series of shift registers used to selectively enable or disable rows and columns, which allows them to be selectively brought into a floating state. The shift registers are fed via a SER and SRCLK line which are used to load 16 bits of binary data, one for each of the two phases for each row and column in an 8x8 array, which can then be loaded to the drivers using the LATCH line.

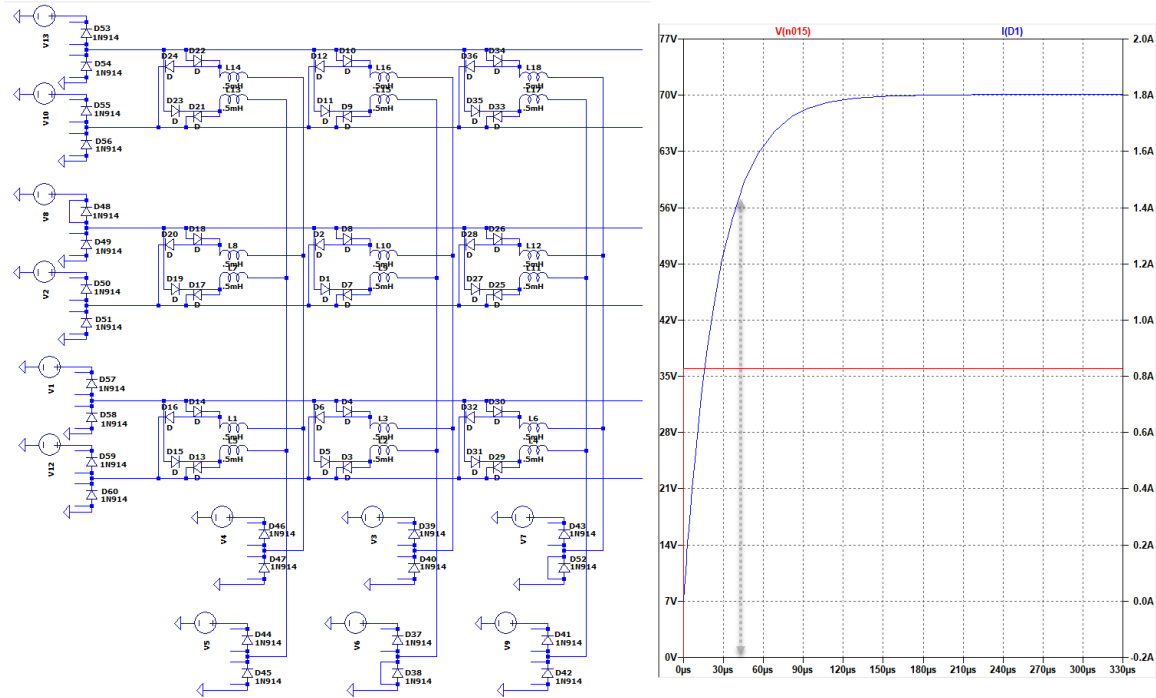


Figure 4-5: 3x3 motor array simulated in LT Spice showing current rise time with a $500 \mu\text{H}$ and 19.5Ω coil winding. The grey line shows rise time to 1.44 A, or 80% of the steady-state current demand through the inductor.

An LT Spice simulation representative of the final circuit layout for a 3x3 array is shown in Figure 4-5, which uses manually bypassable diodes instead of 1/2 bridges, but does validate the lack of parallel paths through other elements in the array. Each phase is modeled as an inductor $I = 500\mu\text{H}$ in series with a resistor $R = 19.5\Omega$, with an associated current rise time of $50\mu\text{s}$. This inductance is low compared to a NEMA packaged stepper motor, which have typical inductances ranging between 2mH and 60mH , but should be drivable with most off the shelf stepper chopper drivers if desired. To validate the array at a smaller scale, a 3x3 hardware prototype was built as shown in Figure 4-6. At this scale the controller was prototyped on a breadboard.

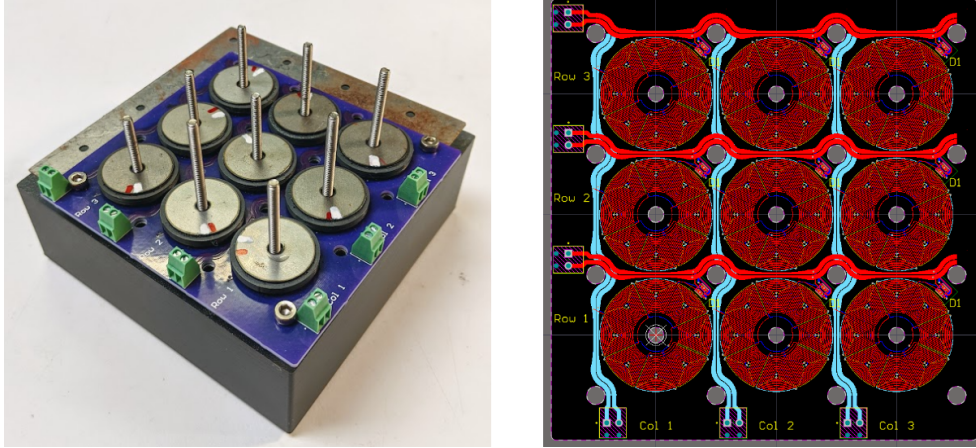


Figure 4-6: 3x3 motor array prototype built for electrical testing and breadboard driver experimentation.

4.1.3 Scaling

Table 4.1 shows a complete BOM for the 8x8 array shown in Figure 4-1, with the exception of the hexagonal tiles. The BOM is divided into driver components numbered 1-8, and motor components numbered 9-14. Another exception is that the PCBs were limited to 4x4 panels to stay under the 100mm x 100mm promotional cost provided by many board houses, where quantity 10 4-layer boards can be purchased for \$14.00 USD. The complete 8x8 array could then be assembled from four of these boards, and the row and column PCBs were broken up similarly. This subdivision increases assembly time and soldering required, but drastically reduces the price of the PCBs at small quantities. All 3D printed parts were quoted using sliced part mass calculated with PrusaSlicer, with a 4% infill for the Printed Stator Base, and 20% infill for the Printed Rotor Base. Spool cost was based on a 1kg spool of PLA priced at \$15.59 per spool. The steel rotor and stator back irons were not included in the BOM also due to uncertainty in their benefit in a next generation prototype. Labor and shipping was not included for any BOM items.

#	Component	Price	Quantity	Total Price
1	Column PCB	\$1.40	2	\$2.80
2	Row PCB	\$1.40	2	\$2.80
3	Quad 1/2 Bridge IC	\$1.65	8	\$13.20
4	Shift Register IC	\$0.07	4	\$0.27
5	Microcontroller IC	\$0.55	2	\$1.10
6	Ceramic Capacitor	\$0.02	28	\$0.56
7	Electrolytic Capacitor	\$0.05	8	\$0.40
8	Resistor	\$0.01	4	\$0.04
	Total		58	\$21.17

9	Stator PCB	\$1.40	4	\$5.60
10	Printed Stator Base	\$3.66	2	\$7.31
11	Printed Rotor Base	\$0.02	64	\$1.30
12	Full Bridge Rectifier Diode IC	\$0.07	64	\$4.35
13	Round 3x3 N50 Nd Magnets	\$0.04	768	\$30.57
14	M3x40 Hex Head Screw	\$0.05	64	\$3.20
	Total		966	\$52.33

Table 4.1: BOM for an 8x8 motor array divided by driver components (1-8) and motor components (9-14).

Total cost for both motor and driver components came to \$72.50 USD, or \$1.13 USD per actuator at prototype quantities. Total component count came to 1024, where only 5.6% of the total component count was accounted for by the driver, and as the multiplexed array grows larger, this percentage diminishes. Table 4.1 shows that part quantity is overwhelmingly dominated by the motor components, where 75% of the total components are accounted for by the rotor magnets, which led to the interest in multipole magnets in Section ???. This scaling gets worse with larger array sizes.

Two metrics used to judge scalability are cost and component count, as shown in

Figures 4-7 A and B, where estimates for both at the prototype quantities from Table 4.1 are extrapolated to up to a 10,000 motor array. While there are still significant improvements left to make if manufacturing at these quantities, these plots are meant to provide some baseline insight. They assume that a single PCB is used for an 8x8 array of motor stators, as well as column and row drivers. Additionally they assume a single multipole magnet is used rather than the 12 individual ones which dominate the component count in Table 4.1.

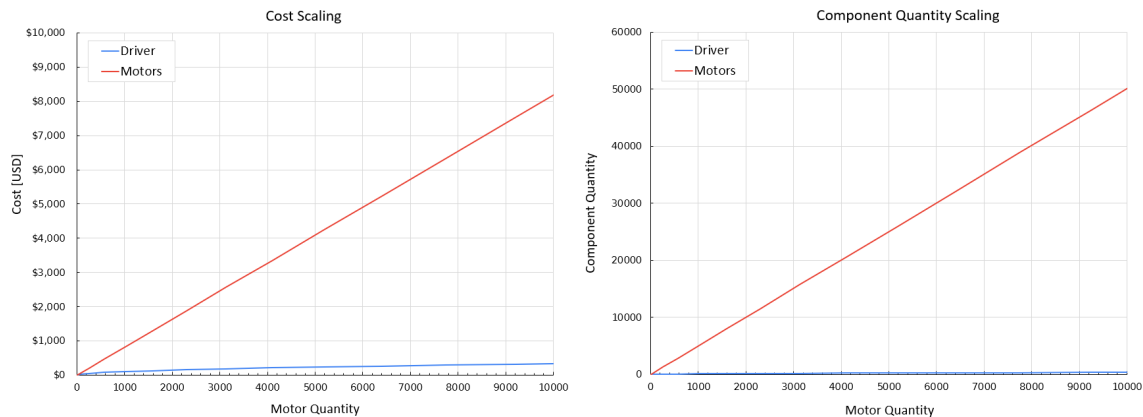


Figure 4-7: Analysis of cost (A) and component quantity (B) scaling relative to motor quantity for the BOM in Table 4.1.

The figures above show that driver cost and component count scales negligibly in comparison to the motors themselves, and most notably multiplexing allows the drivers to scale sub-linearly. This is true under the assumption that an entire array is multiplexed, however a 10,000 motor array with side lengths of 100 actuators would pose severe bottlenecks to individual motor speed when large portions of the array are being actuated simultaneously. Therefore a more thorough analysis would include options for subdividing the multiplexing of the array into smaller segments, at the penalty of driver cost and component count.

4.1.4 Array Control Software

Above the embedded level, a Python script was written to accept an arbitrary 3 dimensional function, and ensure tangency of each hexagonal tile. The array is then

be controlled in real time via serial communication between a host computer running the script and a microcontroller. Each hexagon is assigned an ID and fixed centerpoint corresponding to the point equidistant to the hexagon's three actuators. Three of the hexagon's six corners are then assigned a z position intersecting the function, which is then used to describe a plane on the hexagon's surface, which can be used to find the desired position for each of the three actuators, and the remaining three hexagon corners. This process is then repeated for each hexagon in the array, where neighboring hexagons share at least one intersecting corner.

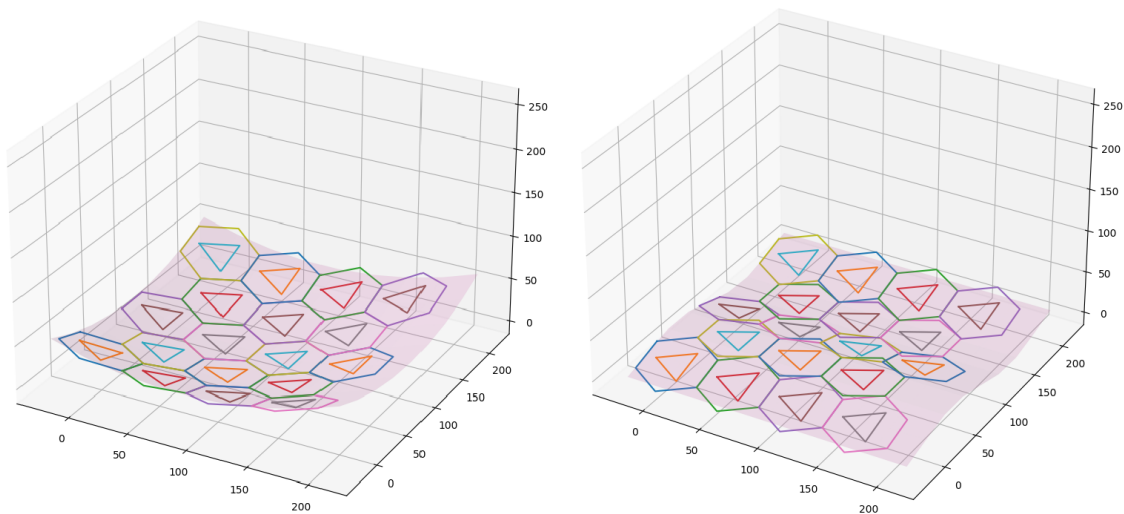


Figure 4-8: Software that generates an arbitrary function and then fits an array of hexagons to A) Concave parabola. B) Sinusoid.

4.1.5 Commutation Control

A conventional stepper motor driver will most often use a chopper driver scheme, where due to the high inductance of a hybrid stepper motor, current can be tightly controlled by chopping the applied voltage with an on-off controller. In the on state, current will rise in the windings, and in the off state it will fall. So long as the chopping frequency is appreciably faster than the decay rate of the windings, minimal current ripples can be achieved. Applied to a stepper motor, this current feedback loop allows for open loop positional control, where current can be applied at all times to create

holding torque, so long as that current is kept below the thermal limits of the motor. Therefore an open-loop stepper motor driver will maintain constant current in its windings, regardless of whether a torque is required or not. This approach can allow for accurate open loop position control, but does drastically lower motor efficiency over idle periods.

Without some form of positional feedback, the motors in this thesis are effectively driven as open loop stepper motors, however multiplexing prevents the use of a constant holding current that results in a deterministic rotor settling over time shown in Figure 4-11. This necessitates that torque be applied in discrete kicks of current, with duration less than the settling time of the motor. Driving the motors this way improves peak multiplexing speed and efficiency, by ensuring that no power is wasted in decelerating the rotor to a deterministic state. However, if a kick is too powerful, the motor may overshoot and skip commutation steps, and if a kick is too weak the motor may undershoot and steps will be lost. This problem is complicated by the fact that the frictional losses between motors in an array may vary with time and motor load. To ensure more deterministic commutation behaviour, shorter repeated kicks were found to be an optimal commutation scheme. As shown in the equations below output torque diminishes as the rotor approaches the target commutation angle, which eliminates the potential for overshooting so long as the acceleration from a single kick is kept sufficiently low.

Figures 4-9 - 4-11 illustrate the results from a discrete time Python simulation, towards optimizing the magnitude, duration, and number of these kicks. The Stall State plot shows a binary representation of commutation being on or off in red, as well as a binary representation of the motor coming to a halt or stall shown in black. All commutations simulated here are $1.5ms$ in duration, and are applied three times, where a subsequent commutation is applied immediately after the motor comes to a stall. The equations of motion are described in Equation 4.2, where torque is proportional to peak torque modeled in Section 3.2, which scales proportional to the surface area of the magnet over the windings, represented as the ratio of A_i and A_m . Frictional and damping torques τ_f and τ_d are then applied counter to the direction of

applied torque using conditional statements.

$$\tau_i = \tau_{peak} \frac{A_i}{A_m} - \tau_f - \tau_d \quad (4.2)$$

Equation 4.3 shows the method for calculating the frictional torque τ_f , which is a constant, found as the product of the normal force estimated in Section 3.2, and an experimentally found coefficient of friction μ . Damping torque τ_d is proportional to velocity, and an experimentally found coefficient of damping, but was kept low for all simulations shown here due to the use of a light machine oil lubricant for the rotors.

$$\tau_f = F_{norm}\mu \quad \tau_d = \dot{\theta}_{i-1}b \quad (4.3)$$

The exact overlapping area A_i can be found via equations 4.4 which converts the current angular position θ_i to area A_i for a given magnet radius $r = 1.5mm$ and commutation angle $\theta_c = 15^\circ$. Note that for a radial arc magnet, this ratio would be directly proportional to commutation angle. For a circular magnet cross section a sinusoidal relationship exists between rotor angle relative to commutation angle, rather than a linear one. Equation 4.4 gives the area of total magnet cross section for a circular magnet to the rotor angle, where $\theta_i = 0^\circ$ is equal to maximum overlap and therefore maximum torque, and $\theta_i = 15^\circ$ is equal to zero overlap and torque. An FEA model accounting for the effects of adjacent windings was estimated to have a negligible impact on torque, and was considered outside the scope of this simulation.

$$A_i = \frac{r^2}{2}(2\phi_i - \sin(2\phi_i)) \quad \phi_i = \cos^{-1}\left(\frac{r - x_i}{r}\right) \quad x_i = 2r \frac{\theta_i}{\theta_c} \quad (4.4)$$

Finally angular acceleration $\ddot{\theta}_i$ can then be found as the ratio of torque to rotational inertia, which can be used to find velocity $\dot{\theta}_i$ as the sum of the previous velocity $\dot{\theta}_i$ and the current acceleration over some timescale dt . Position can then be updated

similarly following the last equation in 4.5.

$$\ddot{\theta}_i = \frac{\tau_i}{I} \quad \dot{\theta}_i = \dot{\theta}_{i-1} + \ddot{\theta}_i dt \quad \theta_i = \theta_{i-1} + \dot{\theta}_i dt \quad (4.5)$$

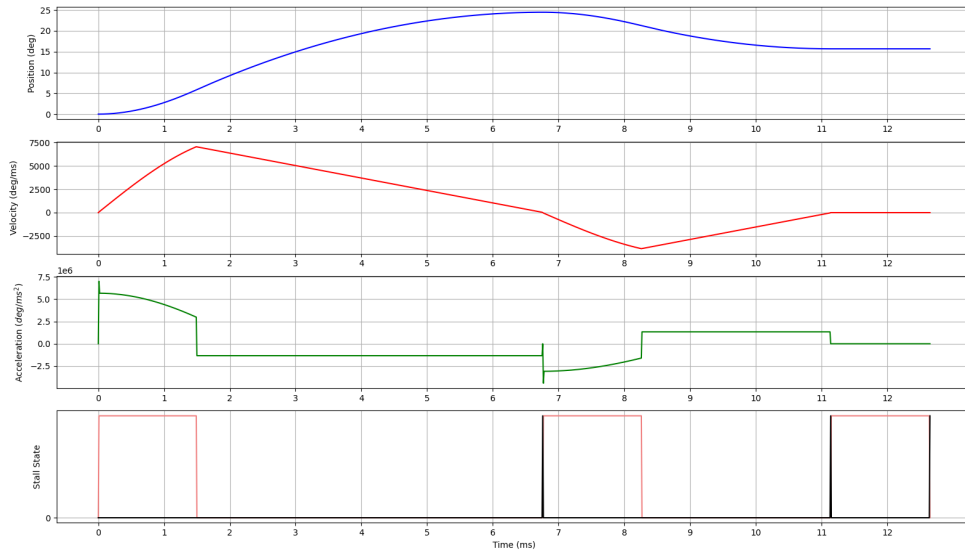


Figure 4-9: First commutation resulting in overshooting before correction in commutation two.

4

Figure 4-9 shows an example of overshooting, where the first motor commutation at $t = 0ms$ causes the rotor to settle at 25° , which is nearly double the target 15° angle. To correct the overshoot, the same phase is commutated again, resulting in torque back towards the 15° target. A third commutation at $t = 11.1ms$ is not able to provide a substantial enough torque to overcome static friction in the rotor, and position remains constant.

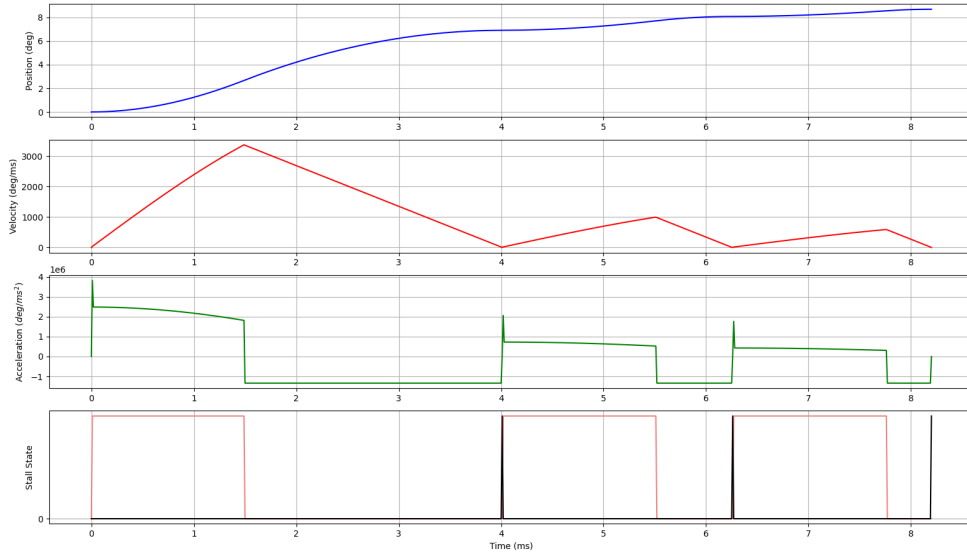


Figure 4-10: Undershooting as a result of increased friction and damping coefficients.

6

Figure 4-10 shows an example of undershooting, where friction and damping are increased such that the rotor is only commutated to $\theta = 7^\circ$ after the first commutation, and the subsequent two commutations are unable to produce a torque significant enough to overcome static friction. This failure condition is difficult to overcome, as the next phase commutated will inherit this final undershot commutation state, and therefore applied torque will be lower than τ_{peak} , resulting in an aggregation of error that ultimately results in lost steps. Because there is presently no positional feedback, this is also the failure mode for increased actuator load.

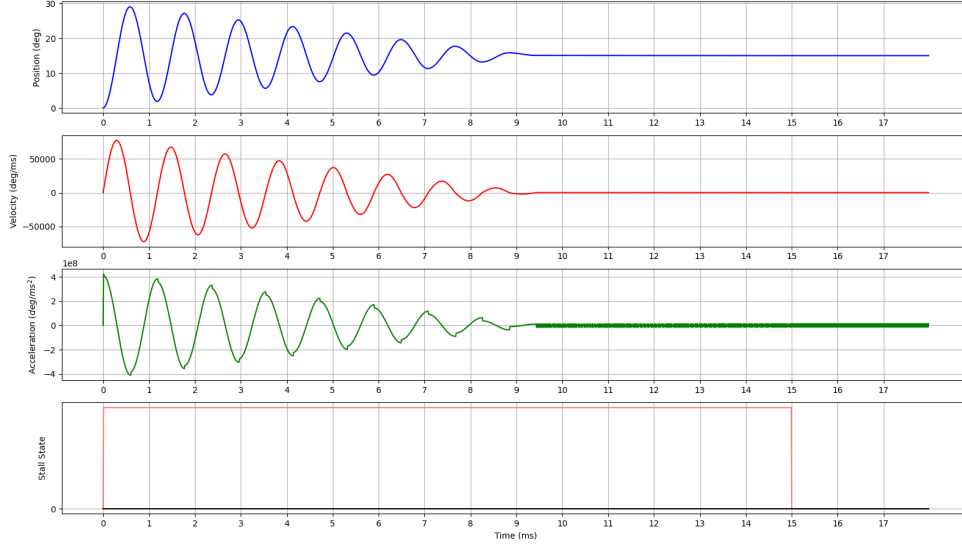


Figure 4-11: Exaggerated commutation cycle time of $15ms$ resulting in ringing, before damping and frictional losses bring the rotor to rest at $\theta = 15^\circ$.

,

Figure 4-11 shows an example of ringing resulting from an exaggerated $15ms$ commutation cycle. This approach is akin to a traditional stepper motor commutation, where a successful target angle can be achieved by supplying a constant holding torque. This approach is not optimal for control of large numbers of actuators due to poor efficiency and heat generation, as well as the increased effective commutation time for each actuator limiting final speed for an array.

Slow motion video was captured and used as a reference to create the failure modes shown in Figures 4-9 and 4-10. Approximate rotor angle could be extracted from video after each commutation, which led to estimation of the following parameters: $\tau_{peak} = Nmm$, $b =$ for damping. For friction, $F_{norm} = N$ was taken from Section 3.2, and a range between $\mu =$ to $\mu =$ where the range resulted in the full scale of over and undershooting. All simulations were run with a discrete time $dt = 10\mu s$.

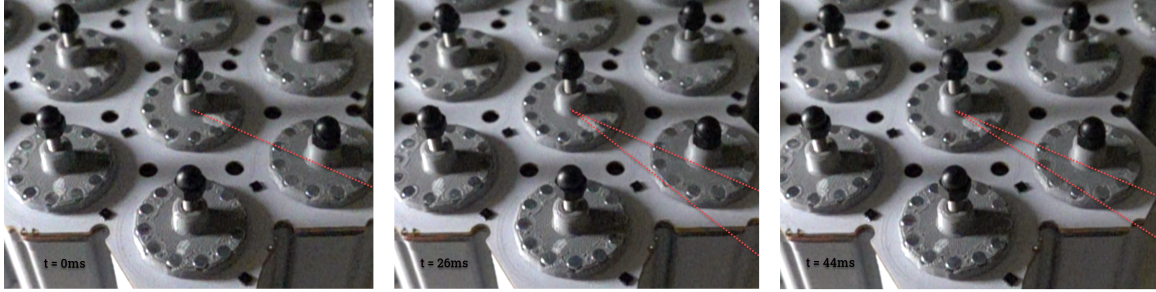


Figure 4-12: 1000 fps slow motion video of motor commutation used to fit model parameters.

Future optimization will be necessary to improve position control, and there is significant headroom for improving speed, efficiency, and commutation resolution. One path towards optimal control is to individually characterize motors in a manufacturing calibration step to account for difference in material properties such as friction. This approach has been shown for diamagnetically levitated milli robots with similar lorentz actuation to achieve $100nm$ positional accuracy and eliminate overshoot [37].

4.2 Characterization

Motor Speed

The use of discrete multiplexed kicks to drive a motor allows us to easily calculate the linear speed for each actuator in an array. As shown in simulation, the motors are currently commutated with three repeated commutations, each lasting $1.5ms$ in duration. Motor speed can be generalized to Equation 4.6, where d is screw pitch in mm per revolution ($0.5mm$), n is number of repeat commutations (3), t_c is commutation time ($1.5ms$), and θ_c is the commutation angle (15°). Finally q represents the total number of rows or columns being multiplexed simultaneously, where each can only be driven sequentially and therefore limit total speed when the entire array is being driven constantly.

$$v_{linear} = dnt_c \frac{\theta_c}{360^\circ} \times \frac{1}{q} \quad (4.6)$$

This results in a maximum individually driven motor speed of $4.63mm/s$, however when multiplexing through rows or columns in an array, this number is divided by side length (8), which results in a peak motor speed of $0.58mm/s$. It is important to note that motor speed is ultimately thermally limited, and peak speed when driving a single motor could not be sustained for extended periods of time. To reduce the likelihood of thermal failure, the microcontroller uses a timer to track elapsed time for each motor in the array, and limits it to $20ms$. Further work to increase torque and reduce rotational inertia of the rotor, along with better thermal management should allow for this number to improve significantly. Finally, the computational overhead at the microcontroller level was not included in this section, as oscilloscope measurements showed that a shift register could be updated in fewer than $10\mu s$ with a Teensy 4.0, which is several orders of magnitude below commutation time.

Output Force

Output torque was modeled using Equation 4.2, and several approaches to finding τ_{peak} through simulation were outlined in Chapter 3. Due to the lack of an adequate torque testing setup, output force was measured instead, using the jig shown in Figure 4-13. Force and torque are related through Equation 4.1, which requires an empirically found coefficient of friction η . Ultimately, direct force measurements were taken via the test setup shown in Figure 4-13, using a Nextech $50N$ load cell with $0.01N$ resolution. Pushing directly against a rigidly mounted load cell would not provide accurate force measurements due to the randomness associated with the commutation angle for which the motor might stall. Instead, a $k = 0.467N/mm$ compression spring was mounted in series between the load cell and tip of the actuator. This allowed for gradual increases in output force to be measured, which are not dependent on linear displacement of the screw. The spring was constrained by a linear stage, and the mass

for both was recorded and later compensated for in the output force measurements. Force was measured by advancing the screw into the spring via rotor commutation, and constraining the spring against the load cell.

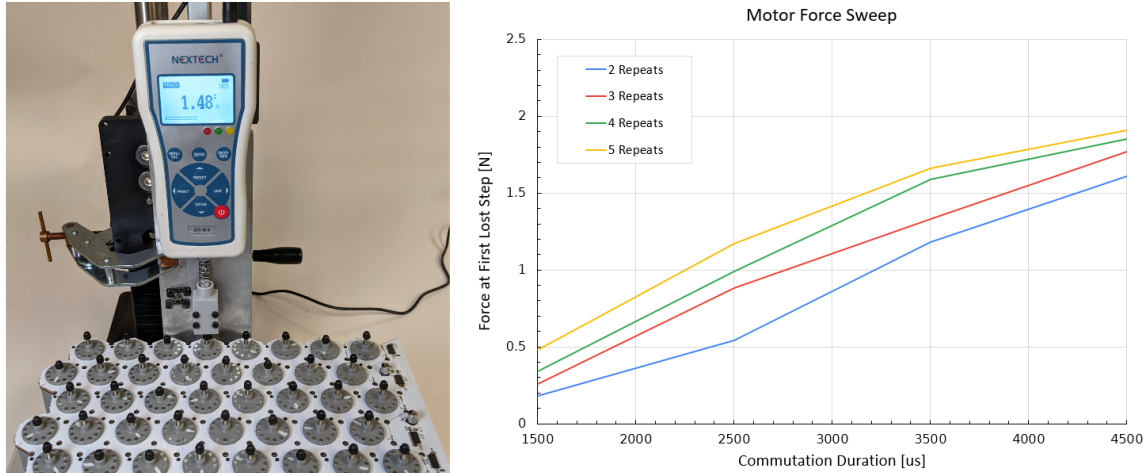


Figure 4-13: A) Force measurement jig. B) Output force measured at first step loss for various commutation durations, swept through 2 to 5 repeat commutations.

Two parameters were swept for force production as shown in Figure 4-13. First commutation duration, which was the length of time a phase was exposed to VCC , and therefore experienced a torque and positive acceleration as shown in Figures 4-9 - 4-11. The second was the number of commutation repetitions, which can be thought of as taking a single longer duration commutation and breaking it up into repeated discrete kicks to avoid rotor overshoot. Both parameters result in relatively linear increases to output torque, with good repeatability between measurements. Applied voltage and therefore steady state current were left at $36V$ which was the max allowed by the power supply, however increase in current is expected to follow a similarly linear relationship to the two temporal parameters. Because motor speed and torque are ultimately thermally limited, an increase in motor voltage and therefore winding current will run into the same thermal limits that increasing commutation duration or repetition would. All of these parameters are expected to be traded equally, so long as total energy consumption is kept constant. Most importantly, it should be noted that these sweeps were possible due to the gradual increase in motor impedance at the

motor output, and applying a $4500\mu s$ commutation duration to an unloaded motor would result in immediate overshoot and loss of position. Therefore, to tap into these higher force outputs for dynamic input impedance, some form of loop closing would be necessary to ensure proper commutation.

Chapter 5

Serial Distributed Actuation

This thesis has primarily focused on the design and control of parallel arrays of distributed actuators. This chapter shifts focus towards serially distributed use cases, in which control of many degrees of freedom arranged in series are required, commonly to form a robotic limb. Figure 5-1 illustrates a distinction that will be drawn upon between the following sections, where serially distributed actuation is categorized as either continuum or serpentine. Continuum actuators, are effectively made up of infinite degrees of freedom by virtue of having joints made up of a compliant material [25]. One or more actuators can then be used to control deformation in the material, and therefore actuator position. A serpentine robot is made up of a finite number of linkages, where each is constrained by a discrete actuator [41]. Serpentine robots can closely approximate a continuum deformation as the number of discrete actuators increases, but are also capable of nonlinear and piecewise deformation. In Section 5.1 a modular toolkit for constructing continuum robots is explored, which taps into many of the benefits of soft, rigid, and modular robotics. Section 5.2 discusses the design of a modular serpentine robot designed for integration with the actuators discussed in Chapter 2, which could act as an assembler for the aforementioned toolkit.

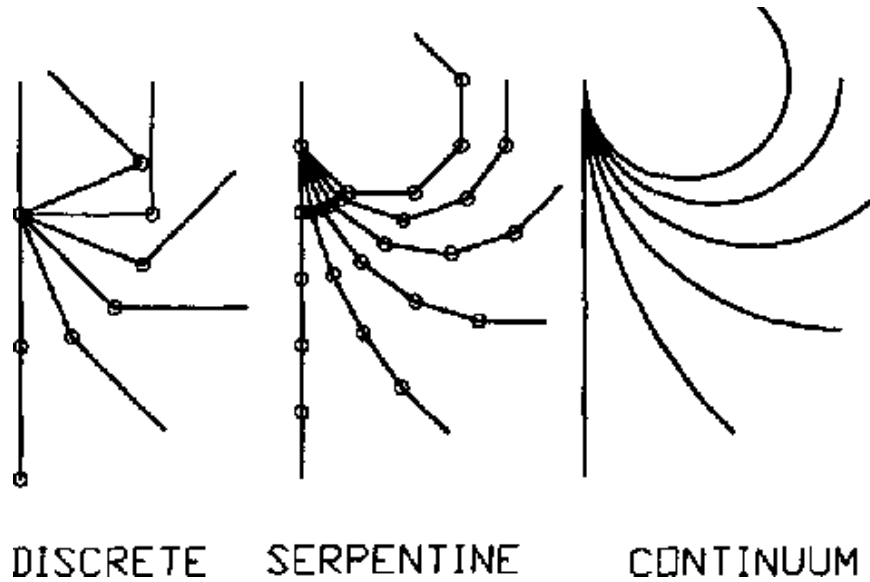


Figure 5-1: Hierarchy of robotic limb degrees of freedom [41].

5.1 Continuum Actuation

A longstanding goal at the CBA has been to construct a toolkit of mechanical metamaterials, made up of discrete and recursive 3-dimensional voxels, which can be assembled to construct modular structures with mechanical properties defined at the voxel level. Voxels have been designed using fiber reinforced composite base materials capable of demonstrating ultralight high stiffness structures [6], as well as structures with tunable mechanical stiffness assembled from a library of voxel geometries [42] [21]. In this case the term mechanical metamaterial implies that material properties are derived from a material's macro geometric features, rather than their bulk material properties. By carefully engineering their placement, larger structures can be assembled which demonstrate particular mechanical properties represented by their constituent parts.

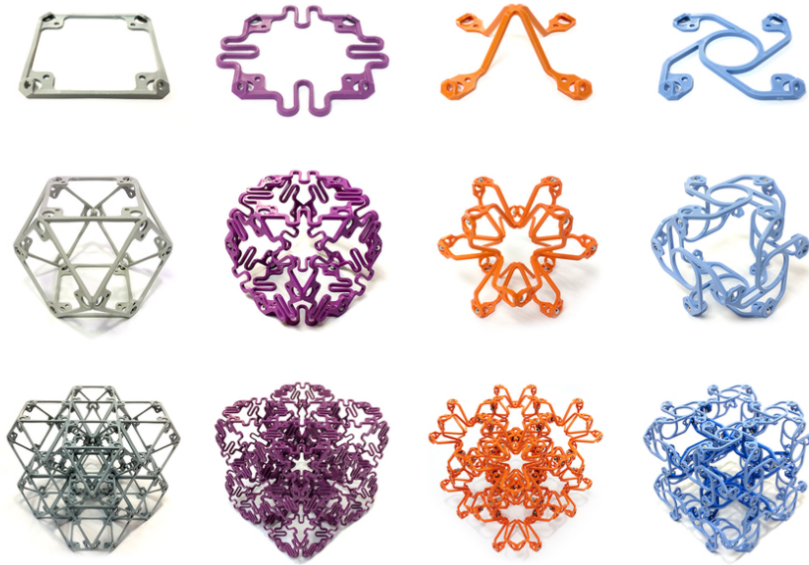


Figure 5-2: Voxel based metamaterials demonstrating a variety of material properties including isotropic, linear, elastic, chiral, and auxetic compliances.

5.1.1 Modular Robot Toolkit

We can use these metamaterials to construct tendon driven continuum robots without the use of dedicated joints. Figure 5-4 shows the tendon routing paths, represented as dotted red and green lines, which are used to induce bending in selectively placed elastic elements. By introducing selective compliances, we can engineer degrees of freedom directly into the structure rather than using discrete revolute, prismatic, or spherical joints. In applying this toolkit to robotics, a continuum actuation scheme that allows for the construction of structural robots that move by bending at these selective compliances has been explored [42] [6] [20]. Figure 5-3 shows the most recent iteration of actuators, which was designed for this thesis. The design uses an inexpensive geared stepper motor that fits within an isometric voxel to spool a tendon and apply tension in either the top or bottom of the limb. In this way actuation specific voxels can be introduced into the toolkit to transition from static to robotic structures. In the context of distributed actuation, if an actuation requirement can be met by a single actuator causing continuum deformation in a structure, we can

circumvent the requirement for a large number of motors while achieving a similar result.

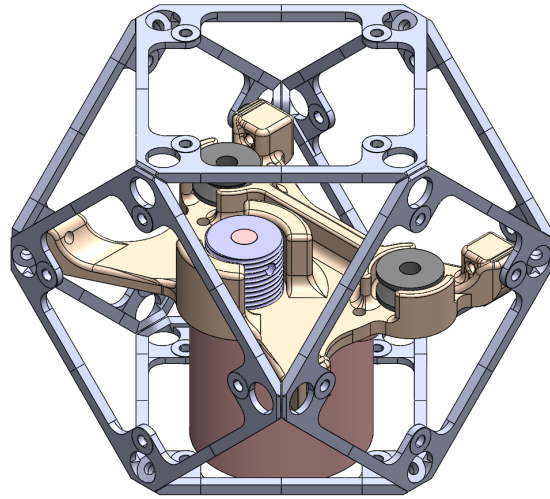


Figure 5-3: Capstan driven voxel actuator utilizing a single 7.5° full step stepper motor with 30:1 gear reduction. V-bearings are used to route cables axially along the skin of a continuum voxel limb into the capstan, as shown in Figure 5-4.

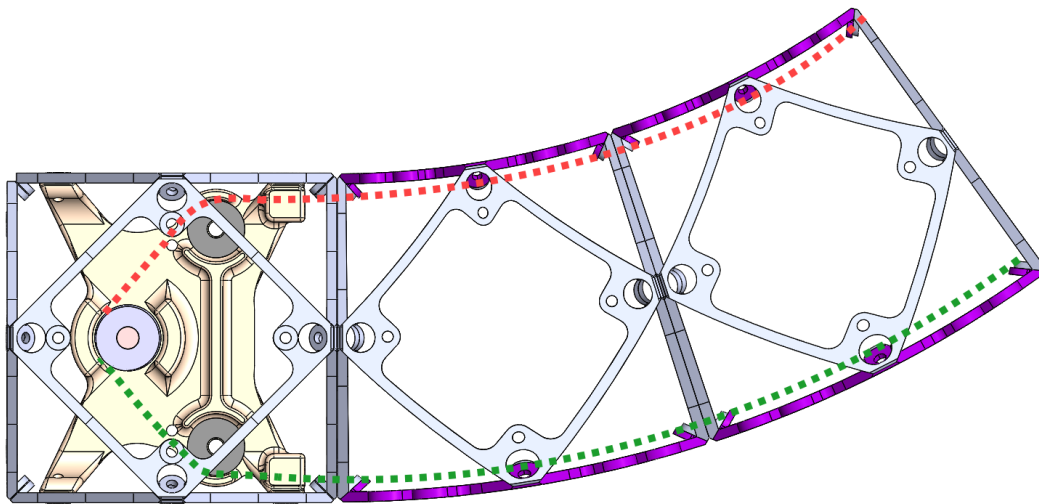


Figure 5-4: Continuum voxel limb deforming under tendon contraction. Tendons in tension are shown with a dotted red line.

Figure 5-3-A shows the tendon configuration applied to deform three selectively compliant voxels in series. In this case the first and third voxel contain carbon fiber

sleeves around the tendon, acting as short circuiting elements to limit the max deflection in that voxel. These short circuiting elements can be used to further constrain compliant behavior, where through testing it was found that friction caused voxels closest to the actuator to deform slightly more than those further away. The same approach could be used to create asymmetrical deformation depending on bending direction. Figure 5-6-B shows a hydrofoil wing built by Alfonso Parra Rubio that introduced a folded 3 dimensional skin [42]. Continuum deformation is appealing for hydrodynamic applications, where the sharp edges created from a conventional aileron are notorious for producing turbulence and loss of efficiency.

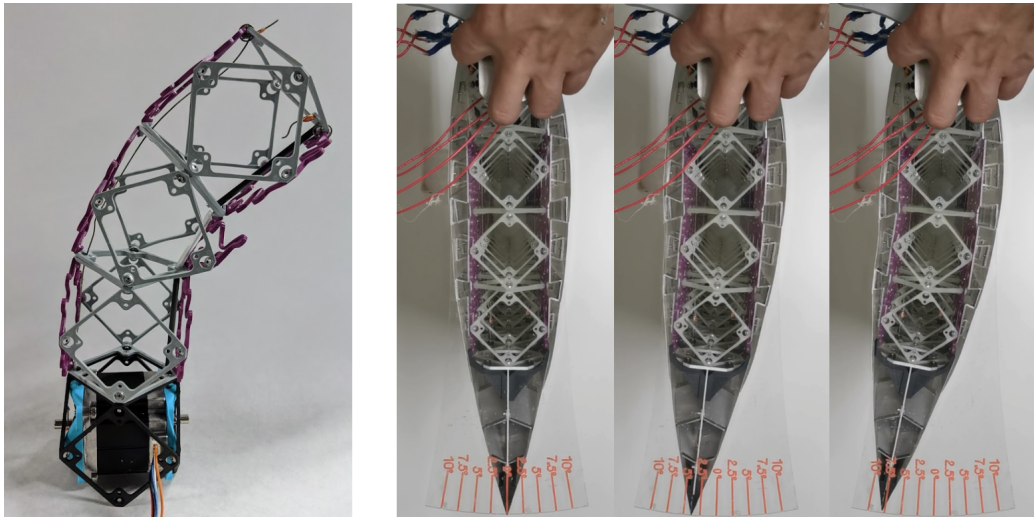


Figure 5-5: A) 1 DOF limb actuated using a spooling dual shaft stepper motor. B) Morphing hydrofoil using the same tendon actuation scheme [42].

In Figure 5-6-A, the same tendon architecture was applied to construct a walking quadrupedal continuum robot. The quadruped consists of eight of the actuation voxels shown in Figure 5-3, two for the shoulder and elbow of each leg. The quadruped is capable of walking autonomously at approximately 400 mm per minute while carrying a battery unit, motor drivers, and a microcontroller.

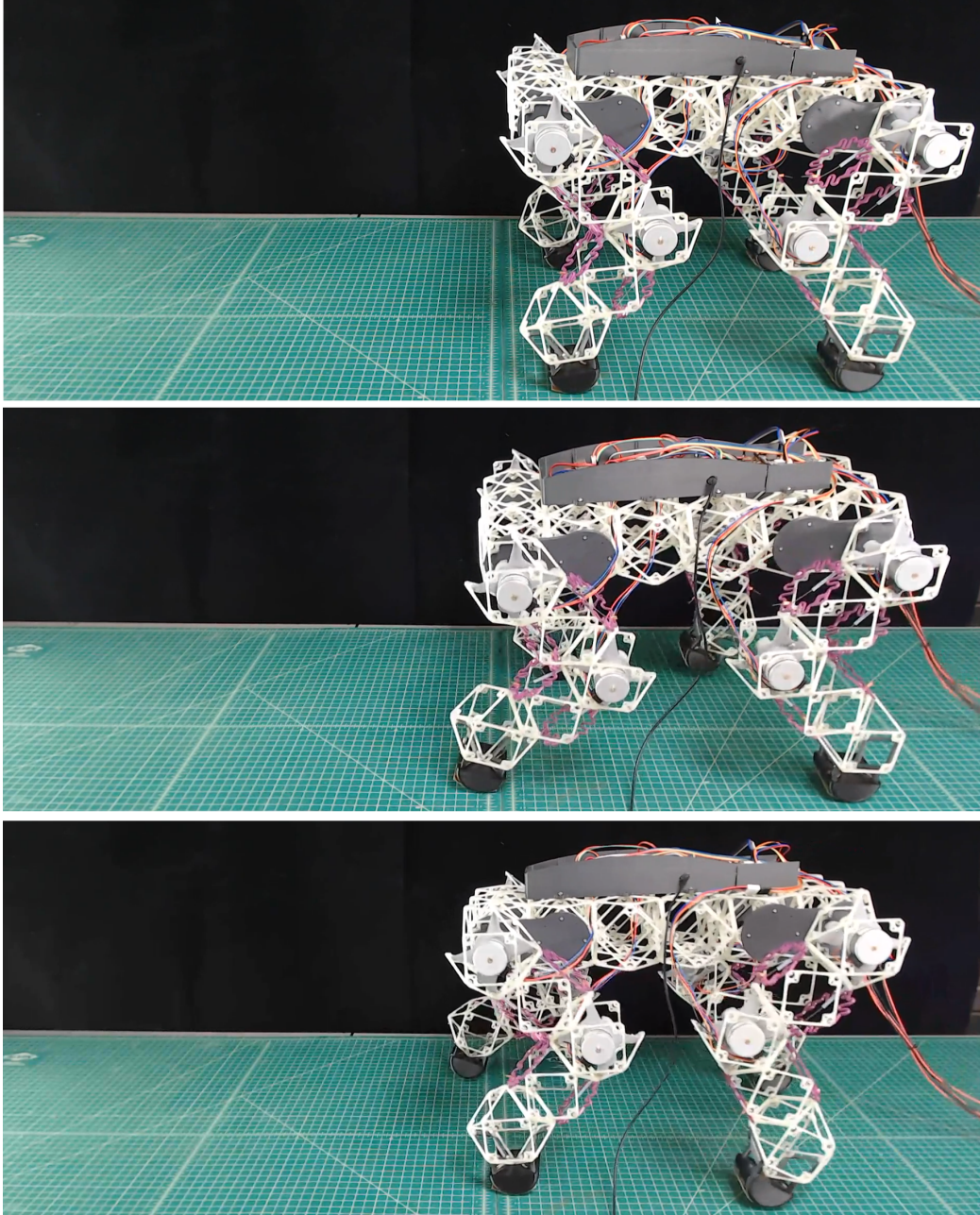


Figure 5-6: Video stills of an 8 degree of freedom walking quadruped, assembled from discrete mechanical metamaterials without the use of conventional rotary or prismatic joints.

The use of a compliant voxel structures in the quadruped result in characteristics of both serial and parallel elastic actuation. Like other soft robots, their series elastic nature results in a decoupling of end effector position and motor position when

external loads are applied. Due to the nature of tendon driven actuation, the limb behaves like a spring with relatively linear spring constant in compression, but tensile loads are taken up by the tendon and transmitted to the motor. Voxel stiffness is essential for the quadruped to support its own weight, but puts a greater burden on the actuator, which must compress a stiff parallel spring in order to move from the limb's neutral position, regardless of the impedance at the end effector. For a walking gait, very little of this energy is recoverable due to the high spring constant of the current generation of voxels, and relatively low impedance faced by the limb in an unloaded state. This behavior becomes particularly relevant when performing dynamic motion such as running or jumping, where it becomes critical to recover parallel elastic energy storage, and ensure that gait stride matches the spring constant of any serial elasticity. A large body of research exists on this topic [13] [11] [29], which represents a critical direction for future research.

To characterize voxel deformation, a computer vision system was built to quantify the non-linearity associated with tendon actuation, as documented in [42]. Displacement was measured through a cartesian mapped and calibrated video feed from a Raspberry Pi Camera, which measured translation and rotation of pairs of ArUco markers assigned to each voxel. Displacement was induced by pulling on a tendon using a tensile tester, which allowed for visualization of deformation as a function of tendon displacement, as well as applied load at steady state. The test setup and output of these measurements can be seen in Figure 5-7, which were helpful in characterizing beam bending in tendon driven structures without a centroid, where compressive loads can cause parasitic deformation beyond pure bending.

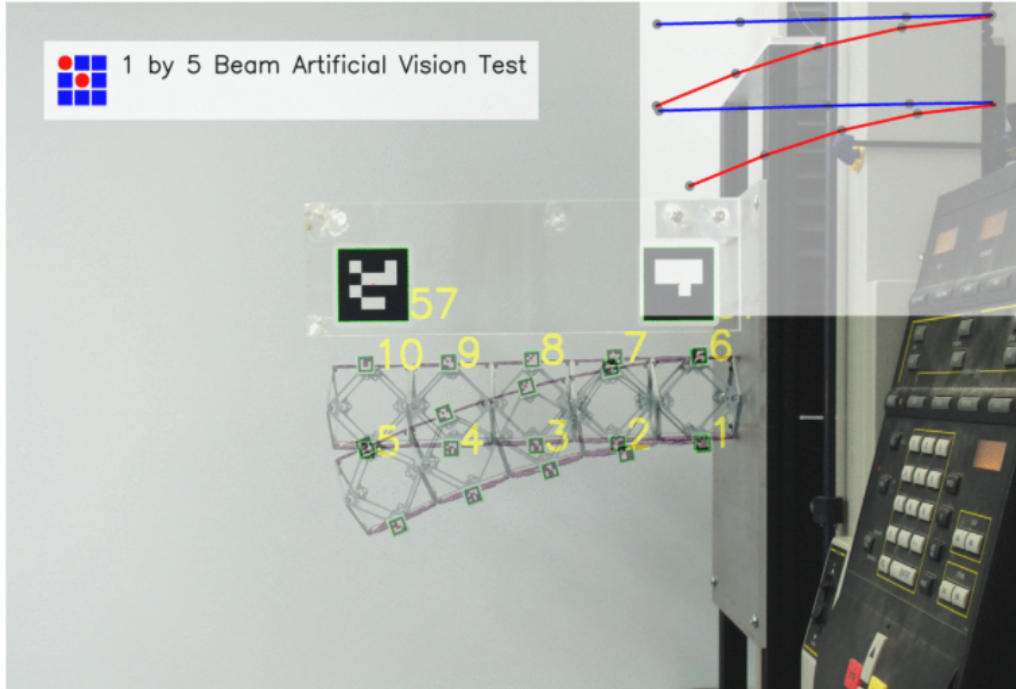


Figure 5-7: Open-CV computer vision system developed to characterize strain in a voxel limb in response to an applied tendon tension.

5.2 Serpentine Actuation

To automate the assembly of the voxel structures discussed in section 5.1, several generations of scalable ribosomal assembly robots have been prototyped to achieve this task [19]. One generation of these robots is shown in Figure 5-8, which are designed to autonomously scale a voxel structure by locomoting similar to an inchworm, while performing assembly and maintenance by placing or removing voxels. Rather than achieving precise locomotion and assembly on their own, these assemblers use the regular spacing of the voxel structure itself to maintain positional accuracy, allowing them to be assembled with relatively low cost and lightweight servomotors.

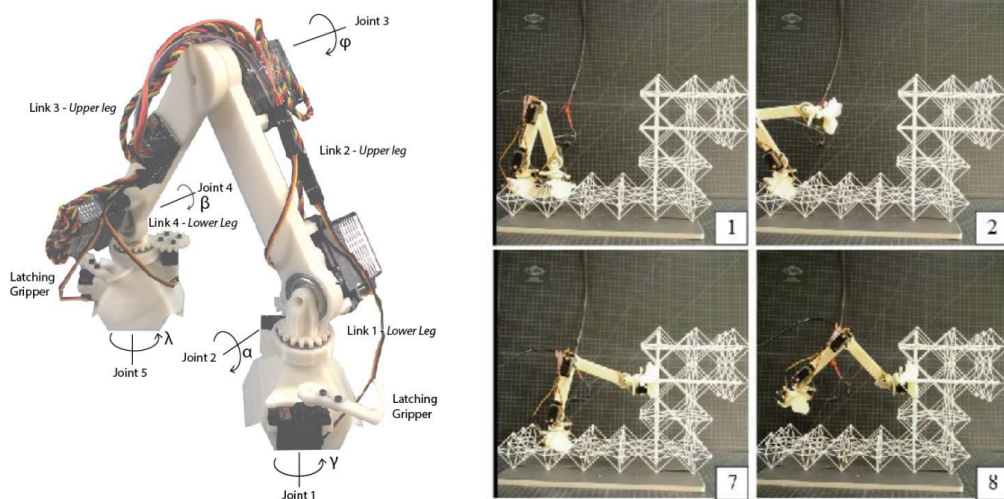


Figure 5-8: A) BILL-E, a 7 DOF serial robot capable of traversing and assembling voxel structures. B) Stills of BILL-E traversing a voxel structure [19].

5.2.1 Ribosomal Assemblers

Figure 5-9 provides an estimate for the required ribosomal assembler swarm sizes necessary to construct structures in a comparable timescale to a gantry based assembler. At larger scales, the estimated required robot quantities to compete with an equivalent gantry assembler approach the ten to hundred thousands, and therefore assuming seven actuators per robot, assembling a $100m$ length scale structure could be expected to require 700,000 actuators. These assemblers can be thought of as small serially distributed actuators themselves, but the primary scaling problems associated with their design stem from the need for large swarms of discrete robots. To that end, a modular serial robot was designed using an arrangement of 3 DOF prismatic actuators that could be made using the same parallelized architecture discussed in chapter 4. In this case a modular array of three actuators could be implemented in parallel as shown in Figure 5-10, and panelized arrays of these modules could leverage the manufacturing and assembly qualities discussed in Chapter 4 to create swarms of discrete robots.

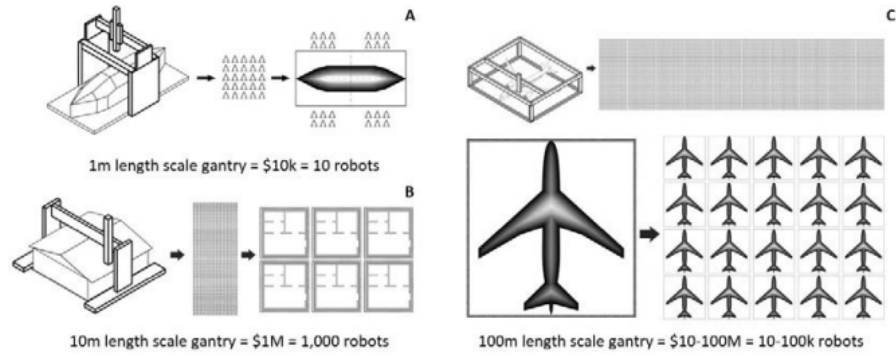


Figure 5-9: Equivalent robot quantities required to assemble structures at various scales [20].

The final prototype as of the time of writing this thesis can be seen in Figure 5-10-B. Six modules are stacked in series to create a robot capable of moving and manipulating objects using a single modular assembly as shown in Figure 5-10-A, although an additional wrist actuator will likely be necessary to navigate a voxel structure. Each module contains a microcontroller and two RS484 modules used for an I2C communication bus between modules, adapted from Jake Read's work on distributed machine control. Power and communication are bussed through each module via the ribbon cable shown in Figure 5-10-B, where thermal limitations along the bus would ultimately limit the number of modules to be placed in series. Each module includes three 25mm diameter stepper motors coupled to an M3 threaded rod which connects to a threaded spherical bearing in the next module. This allows for each module to orient the subsequent module up to 35° in pitch and roll, as well as elongate and contract by up to 25mm . With a

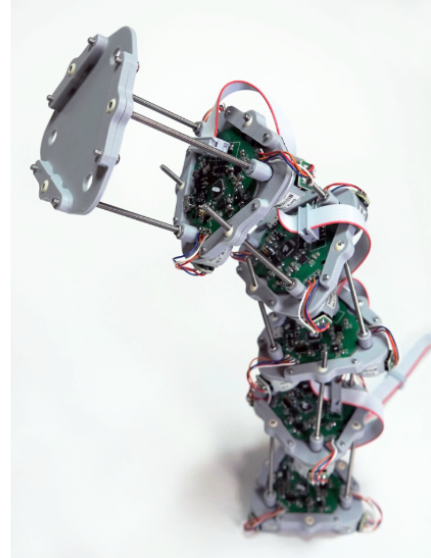
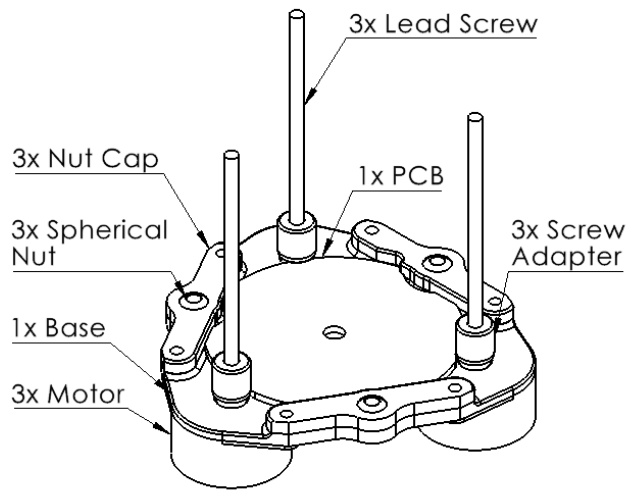


Figure 5-10: A) Serpentine robot module showing assembly components. B) Assembled serpentine robot with five driven and one passive module.

The primary goal for future design iterations will be to replace the discrete stepper motors used in the current design with the PCB motors discussed in Chapter 4. Several design changes at the motor level will be needed to increase output torque and minimize frictional losses associated with the large axial loads calculated in Table 3.2, and mass of the robot. These include increasing motor diameter, which scales linearly with torque, as well as incorporating a rolling element bearing to reduce frictional losses, and continuous driving current with designated motor drivers. The use of directly integrated PCB motors should substantially reduce mass at each module, which would further reduce load requirements. Figure 5-11 shows another module prototype which uses a single lasercut delrin part to replace the module base and spherical nuts shown in Figure 5-10-A. The use of flexures would allow for each module to be assembled with a minimal number of parts, although off-axis flexure stiffness would ultimately determine overall robot stiffness.

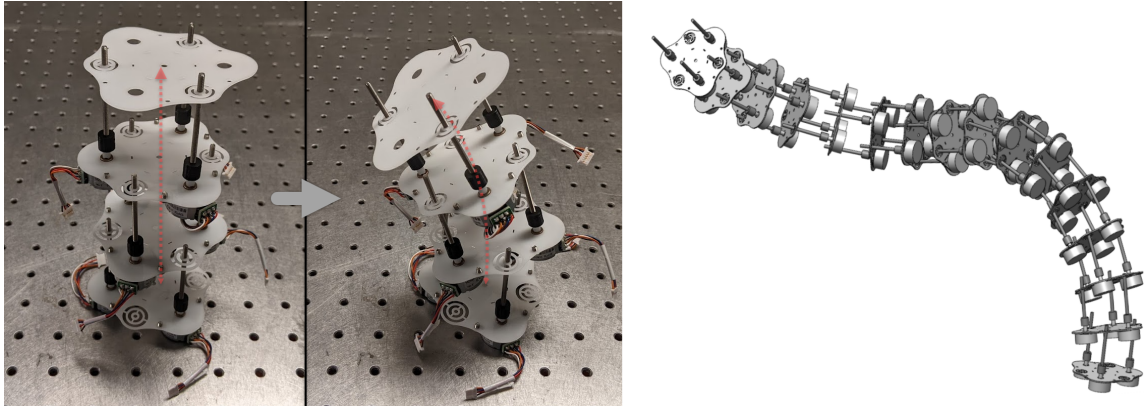


Figure 5-11: A) Serpentine robot arm prototype using spherical flexures. B) CAD model of the flexural prototype extrapolated to higher order degrees of freedom.

Chapter 6

Conclusion

This thesis demonstrated the design and manufacture of a scalable actuator and control scheme, intended to allow for wider adoption of macro-scale distributed actuation applications. An axial flux 2-phase PCB stepper motor was designed and iterated on over a range of prototypes and simulation techniques, including a magnetic circuit model, volume integral model, and a commercial FEA solver. This motor was then integrated into a modular 8x8 array which could be multiplexed at the power electronics level to achieve reliable rotary and linear motion. A discrete time simulation was used to find an optimal multiplexing commutation approach, and a script was written to interpolate arbitrary functions over the surface of the array in real time. Finally two approaches to serially distributed actuation were explored, including a tendon driven continuum robot assembled from discrete metamaterials, and a modular serpentine robot intended for automated assembly of those metamaterials. There is not a clear set of selection criteria for every distributed actuation application, but Table 6.1 outlines several of the key parameters used to guide the design of this thesis, and the results achieved for the prototype 8x8 parallel actuator array.

Future Work

It is likely that there are more suitable motor architectures for distributed actuation at the scales discussed in this thesis, that are only missing economies of scale to be obvious candidates. In particular piezoelectric stepping or stick-slip motors [28], or

Property	8x8 Array
Quantity	64
Actuator Density [sqft ⁻¹]	104.9
Linear Speed [mm/s]	0.868
Mass/Actuator [g]	13.2
Force [N]	1.9
Resolution [μ m]	21
Stroke [mm]	45
Power/Actuator [W]	0.90
Cost/Actuator [USD]	\$1.13

Table 6.1: Critical parameters for characterizing distributed linear actuators.

electrostatically driven microhydraulic actuators [23] have the potential to surpass the resolution and power density capabilities of an electromagnetic motor. In terms of electromagnetic actuation, this work leveraged the maturity and affordability of the PCB fabrication industry to make inexpensive actuators that could be rapidly assembled at large quantities. It is possible that an alternative manufacturing approach such as foil stamping or rotary die cutting would allow for higher throughput and better copper packing densities for manufacturing large numbers of parallelized windings. Because motor rotors present a manufacturing and assembly problem that inherently cannot be parallelized, additional exploration towards designing a switched reluctance motor could potentially yield a rotor consisting of a single stamped sheet metal part, that would provide the greatest improvements towards scalability.

Finally many of the principles outlined in this thesis could be used to achieve distributed position and force sensing. While both of these would be useful for improving distributed actuation use cases, it is likely that they might find use in stand alone applications where distributed sensing of macro-scale structures is required.

Bibliography

- [1] Direct current magnetization curves for various magnetic materials. In *Metals Handbook*, volume 1, page 792. American Society for Metals, 8 edition.
- [2] Adapa. A/S Product Brochure. <https://adapamoulds.com/adapa-a-s-product-brochure/>.
- [3] R. Arsenault, R. Biasi, D. Gallieni, A. Riccardi, P. Lazzarini, N. Hubin, E. Fedrigo, R. Donaldson, S. Oberti, S. Stroebele, R. Conzelmann, and M. Duchateau. A deformable secondary mirror for the VLT. page 62720V. URL: <http://proceedings.spiedigitallibrary.org/proceeding.aspx?doi=10.1117/12.672879>, <https://doi.org/10.1117/12.672879> doi:10.1117/12.672879.
- [4] Susan V. Brooks. Current Topics for Teaching Skeletal Muscle Physiology. 27(4):171–182. URL: <https://journals.physiology.org/doi/10.1152/advan.2003.27.4.171>, <https://doi.org/10.1152/advan.2003.27.4.171> doi:10.1152/advan.2003.27.4.171.
- [5] Nick Cheney, Robert MacCurdy, Jeff Clune, and Hod Lipson. Unshackling evolution: Evolving soft robots with multiple materials and a powerful generative encoding. In *Proceeding of the Fifteenth Annual Conference on Genetic and Evolutionary Computation Conference - GECCO '13*, page 167. ACM Press. URL: <http://dl.acm.org/citation.cfm?doid=2463372.2463404>, <https://doi.org/10.1145/2463372.2463404> doi:10.1145/2463372.2463404.
- [6] Nicholas B Cramer, Daniel W Cellucci, Olivia B Formoso, Christine E Gregg, Benjamin E Jenett, Joseph H Kim, Martynas Lendraitis, Sean S Swei, Greenfield T Trinh, Khanh V Trinh, and Kenneth C Cheung. Elastic shape morphing of ultralight structures by programmable assembly. 28(5):055006. URL: <https://iopscience.iop.org/article/10.1088/1361-665X/ab0ea2>, <https://doi.org/10.1088/1361-665X/ab0ea2> doi:10.1088/1361-665X/ab0ea2.
- [7] Ronan Daly, Tomás S. Harrington, Graham D. Martin, and Ian M. Hutchings. Inkjet printing for pharmaceuticals – A review of research and manufacturing. 494(2):554–567. URL: <https://linkinghub.elsevier.com/retrieve/pii/S0378517315002331>, <https://doi.org/10.1016/j.ijpharm.2015.03.017> doi:10.1016/j.ijpharm.2015.03.017.

- [8] Oliver Dietzel. – Hybrid Nanopositioning Systems with Piezo Actuators. URL: https://static.pi-usa.us/fileadmin/user_upload/pi_us/files/blog/PI-WP4014-Hybrid-Nanopositioning-Systems.pdf.
- [9] ECM. ECM Product Website. <https://pcbstator.com/>.
- [10] L. Flemming and S. Mascaro. Control of Scalable Wet SMA Actuator Arrays. In *Proceedings of the 2005 IEEE International Conference on Robotics and Automation*, pages 1338–1343. IEEE. URL: <http://ieeexplore.ieee.org/document/1570301/>, <https://doi.org/10.1109/ROBOT.2005.1570301> doi:10.1109/ROBOT.2005.1570301.
- [11] Gerrit A. Folkertsma, Sangbae Kim, and Stefano Stramigioli. Parallel stiffness in a bounding quadruped with flexible spine. In *2012 IEEE/RSJ International Conference on Intelligent Robots and Systems*, pages 2210–2215. IEEE. URL: <http://ieeexplore.ieee.org/document/6385870/>, <https://doi.org/10.1109/IROS.2012.6385870> doi:10.1109/IROS.2012.6385870.
- [12] Azam Gholizadeh, Siamak Abbaslou, Pengfei Xie, Ara Knaian, and Mehdi Javanmard. Electronically actuated microfluidic valves with zero static-power consumption using electropermanent magnets. 296:316–323. URL: <https://linkinghub.elsevier.com/retrieve/pii/S0924424719301943>, <https://doi.org/10.1016/j.sna.2019.06.037> doi:10.1016/j.sna.2019.06.037.
- [13] Martin Grimmer, Mahdy Eslamy, Stefan Glied, and Andre Seyfarth. A comparison of parallel- and series elastic elements in an actuator for mimicking human ankle joint in walking and running. In *2012 IEEE International Conference on Robotics and Automation*, pages 2463–2470. IEEE. URL: <http://ieeexplore.ieee.org/document/6224967/>, <https://doi.org/10.1109/ICRA.2012.6224967> doi:10.1109/ICRA.2012.6224967.
- [14] Haihong Zhu and Wayne J. Book. Construction and control of massive hydraulic miniature-actuator-sensor array. In *2006 IEEE Conference on Computer Aided Control System Design, 2006 IEEE International Conference on Control Applications, 2006 IEEE International Symposium on Intelligent Control*, pages 820–825. IEEE. URL: <http://ieeexplore.ieee.org/document/4776751/>, <https://doi.org/10.1109/CACSD-CCA-ISIC.2006.4776751> doi:10.1109/CACSD-CCA-ISIC.2006.4776751.
- [15] J. R. Hendershot and T. J. E. Miller. *Design of Brushless Permanent-Magnet Motors*. Number 37 in Monographs in Electrical and Electronic Engineering. Magna Physics Pub. ; Clarendon Press.
- [16] David H. Hughes, F. Peter Schloerb, Itziar Aretxaga, Edgar Castillo-Domínguez, Miguel Chávez Dagostino, Edgar Colín, Neal Erickson, Daniel

Ferrusca Rodriguez, David M. Gale, Arturo Gómez-Ruiz, José Luis Hernández Rebollar, Mark Heyer, James D. Lowenthal, Alfredo Montaña, Marcos Emir Moreno Nolasco, Gopal Narayanan, Alexandra Pope, Iván Rodríguez-Montoya, David Sánchez-Argüelles, David R. Smith, Kamal Souccar, Miguel Velázquez de la Rosa Becerra, Grant W. Wilson, and Min S. Yun. The Large Millimeter Telescope (LMT) Alfonso Serrano: Current status and telescope performance. In Heather K. Marshall, Jason Spyromilio, and Tomonori Usuda, editors, *Ground-Based and Airborne Telescopes VIII*, page 277. SPIE. URL: <https://www.spiedigitallibrary.org/conference-proceedings-of-spie/11445/2561893/The-Large-Millimeter-Telescope-LMT-Alfonso-Serrano--current-status/10.1117/12.2561893.full>, <https://doi.org/10.1117/12.2561893> doi: 10.1117/12.2561893.

- [17] Infinitum. Infinitum Product Website. <https://www.infinitumelectric.com/>.
- [18] G.H. Jang and J.H. Chang. Development of an axial-gap spindle motor for computer hard disk drives using PCB winding and dual air gaps. 38(5):3297–3299. URL: <http://ieeexplore.ieee.org/document/1042530/>, <https://doi.org/10.1109/TMAG.2002.802292> doi:10.1109/TMAG.2002.802292.
- [19] Ben Jenett and Kenneth Cheung. BILL-E: Robotic Platform for Locomotion and Manipulation of Lightweight Space Structures. In *25th AIAA/AHS Adaptive Structures Conference*. American Institute of Aeronautics and Astronautics. URL: <https://arc.aiaa.org/doi/10.2514/6.2017-1876>, <https://doi.org/10.2514/6.2017-1876> doi:10.2514/6.2017-1876.
- [20] Benjamin Jenett. Discrete Mechanical Metamaterials. URL: <https://cba.mit.edu/docs/theses/20.09.jenett.pdf>.
- [21] Benjamin Jenett, Christopher Cameron, Filippos Tournomousis, Alfonso Parra Rubio, Megan Ochalek, and Neil Gershenfeld. Discretely assembled mechanical metamaterials. 6(47):eabc9943. URL: <https://www.science.org/doi/10.1126/sciadv.abc9943>, <https://doi.org/10.1126/sciadv.abc9943> doi:10.1126/sciadv.abc9943.
- [22] Benjamin Jenett, Christine Gregg, Daniel Cellucci, and Kenneth Cheung. Design of multifunctional hierarchical space structures. In *2017 IEEE Aerospace Conference*, pages 1–10. IEEE. URL: <http://ieeexplore.ieee.org/document/7943913/>, <https://doi.org/10.1109/AERO.2017.7943913> doi:10.1109/AERO.2017.7943913.
- [23] Jakub Kedzierski and Hero Chea. Multilayer microhydraulic actuators with speed and force configurations. 7(1):22. URL: <http://www.nature.com/articles/s41378-021-00240-7>, <https://doi.org/10.1038/s41378-021-00240-7> doi:10.1038/s41378-021-00240-7.

- [24] Ara Knaian. Electropermanent Magnetic Connectors and Actuators: Devices and Their Application in Programmable Matter.
- [25] Puneet Kumar Singh and C. Murali Krishna. Continuum Arm Robotic Manipulator: A Review. 2(6):193–198. URL: http://www.hrpub.org/journals/article_info.php?aid=1728, <https://doi.org/10.13189/ujme.2014.020603> doi:10.13189/ujme.2014.020603.
- [26] Richard J. Lacasse. Green Bank Telescope active surface system. pages 310–319. URL: <http://proceedings.spiedigitallibrary.org/proceeding.aspx?articleid=944996>, <https://doi.org/10.1117/12.308802> doi:10.1117/12.308802.
- [27] Daniel Leithinger, Sean Follmer, Alex Olwal, and Hiroshi Ishii. Physical telepresence: Shape capture and display for embodied, computer-mediated remote collaboration. In *Proceedings of the 27th Annual ACM Symposium on User Interface Software and Technology*, pages 461–470. ACM. URL: <https://dl.acm.org/doi/10.1145/2642918.2647377>, <https://doi.org/10.1145/2642918.2647377> doi:10.1145/2642918.2647377.
- [28] Hsien-Shun Liao, Christian Werner, Roman Slipets, Peter Emil Larsen, Ing-Shouh Hwang, Tien-Jen Chang, Hans Ulrich Danzebrink, Kuang-Yuh Huang, and En-Te Hwu. Low-cost, open-source XYZ nanopositioner for high-precision analytical applications. 11:e00317. URL: <https://linkinghub.elsevier.com/retrieve/pii/S2468067222000621>, <https://doi.org/10.1016/j.ohx.2022.e00317> doi:10.1016/j.ohx.2022.e00317.
- [29] Xin Liu, Anthony Rossi, and Ioannis Poulakakis. A Switchable Parallel Elastic Actuator and its Application to Leg Design for Running Robots. 23(6):2681–2692. URL: <https://ieeexplore.ieee.org/document/8470106/>, <https://doi.org/10.1109/TMECH.2018.2871670> doi:10.1109/TMECH.2018.2871670.
- [30] P.-Y. Madec. Overview of deformable mirror technologies for adaptive optics and astronomy. pages 844705–844705–18. URL: <http://proceedings.spiedigitallibrary.org/proceeding.aspx?articleid=1358867>, <https://doi.org/10.1117/12.924892> doi:10.1117/12.924892.
- [31] David Meeker. *Finite Element Method Magnetics User’s Manual*. FEMM, 4.2 edition.
- [32] PCB Motor. How to Reduce Motor Size by Integrating Accurate, Low Cost Piezo Motors. URL: <https://pcbmotor.com/whitepaper-how-to-reduce-motor-size/>.
- [33] Chris Munro and Daniel Walczyk. Reconfigurable Pin-Type Tooling: A Survey of Prior Art and Reduction to Practice. 129(3):551–565. URL: <https://asmedigitalcollection.asme.org/manufacturingscience/article/>

129/3/551/462123/Reconfigurable-PinType-Tooling-A-Survey-of-Prior,
<https://doi.org/10.1115/1.2714577> doi:10.1115/1.2714577.

- [34] Royal Institute of Technology. Emetor, PMSM design tool.
<http://www.eme.ee.kth.se/emetor>.
- [35] Andres Osorio Salazar, Yusuke Sugahara, Daisuke Matsuura, and Yukio Takeda. Scalable Output Linear Actuators, a Novel Design Concept Using Shape Memory Alloy Wires Driven by Fluid Temperature. 9(1):14. URL: <https://www.mdpi.com/2075-1702/9/1/14>, <https://doi.org/10.3390/machines9010014> doi:10.3390/machines9010014.
- [36] John M. Papazian. Tools of Change. 124(02):52–55.
<https://doi.org/10.1115/1.2002-FEB-4> doi:10.1115/1.2002-FEB-4.
- [37] Ron Pelrine, Allen Hsu, Annjoe Wong-Foy, Brian McCoy, and Cregg Cowan. Optimal control of diamagnetically levitated milli robots using automated search patterns. In *2016 International Conference on Manipulation, Automation and Robotics at Small Scales (MARSS)*, pages 1–6. IEEE. URL: <http://ieeexplore.ieee.org/document/7561725/>, <https://doi.org/10.1109/MARSS.2016.7561725> doi:10.1109/MARSS.2016.7561725.
- [38] Ron Pelrine, Annjoe Wong-Foy, Allen Hsu, and Brian McCoy. Self-assembly of milli-scale robotic manipulators: A path to highly adaptive, robust automation systems. In *2016 International Conference on Manipulation, Automation and Robotics at Small Scales (MARSS)*, pages 1–6. <https://doi.org/10.1109/MARSS.2016.7561728> doi:10.1109/MARSS.2016.7561728.
- [39] Markus Raab, Arif Kazi, and David L. Trumper. Magnetically levitated BLDC motor as a modular teaching tool. In *2015 16th International Conference on Research and Education in Mechatronics (REM)*, pages 255–262. <https://doi.org/10.1109/REM.2015.7380403> doi:10.1109/REM.2015.7380403.
- [40] François Rigaut. Astronomical Adaptive Optics. 127(958):1197–1203. URL: <http://iopscience.iop.org/article/10.1086/684512>, <https://doi.org/10.1086/684512> doi:10.1086/684512.
- [41] G. Robinson and J.B.C. Davies. Continuum robots - a state of the art. In *Proceedings 1999 IEEE International Conference on Robotics and Automation (Cat. No.99CH36288C)*, volume 4, pages 2849–2854. IEEE. URL: <http://ieeexplore.ieee.org/document/774029/>, <https://doi.org/10.1109/ROBOT.1999.774029> doi:10.1109/ROBOT.1999.774029.
- [42] Alfonso Parra Rubio. Discrete Continuum Robotic Structures.

- [43] Bulent Sarlioglu, Casey T. Morris, Di Han, and Silong Li. Driving Toward Accessibility: A Review of Technological Improvements for Electric Machines, Power Electronics, and Batteries for Electric and Hybrid Vehicles. 23(1):14–25. URL: <http://ieeexplore.ieee.org/document/7733081/>, <https://doi.org/10.1109/MIAS.2016.2600739> doi:10.1109/MIAS.2016.2600739.
- [44] Takuso Sato, Hiroyuki Ishida, and Osamu Ikeda. Adaptive PVDF piezoelectric deformable mirror system. 19(9):1430. URL: <https://opg.optica.org/abstract.cfm?URI=ao-19-9-1430>, <https://doi.org/10.1364/AO.19.001430> doi:10.1364/AO.19.001430.
- [45] Aniruddha V. Shembekar, Yeo Jung Yoon, Alec Kanyuck, and Satyandra K. Gupta. Generating Robot Trajectories for Conformal Three-Dimensional Printing Using Nonplanar Layers. 19(3):031011. URL: <https://asmedigitalcollection.asme.org/computingengineering/article/doi/10.1115/1.4043013/726284/Generating-Robot-Trajectories-for-Conformal>, <https://doi.org/10.1115/1.4043013> doi:10.1115/1.4043013.
- [46] Alexa F. Siu, Eric J. Gonzalez, Shenli Yuan, Jason B. Ginsberg, and Sean Follmer. shapeShift: 2D Spatial Manipulation and Self-Actuation of Tabletop Shape Displays for Tangible and Haptic Interaction. In *Proceedings of the 2018 CHI Conference on Human Factors in Computing Systems*, pages 1–13. ACM. URL: <https://dl.acm.org/doi/10.1145/3173574.3173865>, <https://doi.org/10.1145/3173574.3173865> doi:10.1145/3173574.3173865.
- [47] Anthony Steed, Eyal Ofek, Mike Sinclair, and Mar Gonzalez-Franco. A mechatronic shape display based on auxetic materials. 12(1):4758. URL: <https://www.nature.com/articles/s41467-021-24974-0>, <https://doi.org/10.1038/s41467-021-24974-0> doi:10.1038/s41467-021-24974-0.
- [48] Maurice Taylor. Magnetically operated sign.
- [49] Arnold Magnetic Technologies. NEODYMIUM IRON BORON MAGNETS. URL: <https://www.arnoldmagnetics.com/products/neodymium-iron-boron-magnets/>.
- [50] Thorlabs. Piezoelectric Deformable Mirror DMH40(/M)-F01 Operation Manual. URL: <https://www.thorlabs.com/drawings/9b1aad257aa26d64-92799946-F7F0-BC13-71CCFD6C96C70FB4/DMH40-F01-Manual.pdf>.
- [51] Lei Tian, Zhengxiong Zhu, Jialian Zhang, and Jianqiang Ma. Design and fabrication of deformable mirror driven by piezoelectric buzzer array. page 102555F. URL: <http://proceedings.spiedigitallibrary.org/proceeding.aspx?doi=10.1117/12.2267774>, <https://doi.org/10.1117/12.2267774> doi:10.1117/12.2267774.

- [52] Furkan Tokgöz, Gökhan Çakal, and Ozan Keysan. Comparison of PCB winding topologies for axial-flux permanent magnet synchronous machines. 14(13):2577–2586. URL: <https://onlinelibrary.wiley.com/doi/10.1049/iet-epa.2020.0622>, <https://doi.org/10.1049/iet-epa.2020.0622> doi:10.1049/iet-epa.2020.0622.
- [53] Sana Ullah, Steve P. McDonald, Richard Martin, Maamar Benarous, and Glynn J. Atkinson. A Permanent Magnet Assist, Segmented Rotor, Switched Reluctance Drive for Fault Tolerant Aerospace Applications. 55(1):298–305. URL: <https://ieeexplore.ieee.org/document/8432090/>, <https://doi.org/10.1109/TIA.2018.2864718> doi:10.1109/TIA.2018.2864718.
- [54] R. Velazquez, E.E. Pissaloux, and M. Wiertlewski. A compact tactile display for the blind with shape memory alloys. In *Proceedings 2006 IEEE International Conference on Robotics and Automation, 2006. ICRA 2006.*, pages 3905–3910. IEEE. URL: <http://ieeexplore.ieee.org/document/1642300/>, <https://doi.org/10.1109/ROBOT.2006.1642300> doi:10.1109/ROBOT.2006.1642300.
- [55] Elise Vernet, Marc Cayrel, Norbert Hubin, Roberto Biasi, Gerald Angerer, Mario Andrighettoni, Dietrich Pescoller, Daniele Gallieni, Matteo Tintori, Marco Mantegazza, Armando Riccardi, Marco Riva, Giorgio Pariani, Runa Briguglio, and Marco Xompero. The Adaptive Mirror for the E-ELT. <https://doi.org/10.12839/AO4ELT3.13431> doi:10.12839/AO4ELT3.13431.
- [56] Daniel F. Walczyk, Jayant Lakshmikanthan, and Daniel R. Kirk. Development of a reconfigurable tool for forming aircraft body panels. 17(4):287–296. URL: <https://linkinghub.elsevier.com/retrieve/pii/S0278612598800769>, [https://doi.org/10.1016/S0278-6125\(98\)80076-9](https://doi.org/10.1016/S0278-6125(98)80076-9) doi:10.1016/S0278-6125(98)80076-9.
- [57] Zhijian Wang. Rapid Manufacturing of Vacuum Forming Components Utilising Reconfigurable Screw-Pin Tooling. URL: http://eprints.nottingham.ac.uk/11403/1/Rapid_Manufacturing_of_Vacuum_Forming_Components_Utilising_Reconfigurable_Screw_Pin_Tooling.pdf.
- [58] Elliot Williams, Charles Dorn, Sergio Pellegrino, and Ali Hajimiri. Origami Inspired Shape Changing Phased Array. In *2020 50th European Microwave Conference (EuMC)*. IEEE.
- [59] Yang Xu, Ziqi Wang, Siyu Gong, and Yong Chen. Reusable support for additive manufacturing. 39:101840. URL: <https://linkinghub.elsevier.com/retrieve/pii/S2214860421000051>, <https://doi.org/10.1016/j.addma.2021.101840> doi:10.1016/j.addma.2021.101840.
- [60] Zhenishbek Zhakypov, Edin Golubovic, Tarik Uzunovic, and Asif Sabanovic. High precision control of a walking piezoelectric motor in

bending mode. In *2013 9th Asian Control Conference (ASCC)*, pages 1–6. IEEE. URL: <http://ieeexplore.ieee.org/document/6606270/>, <https://doi.org/10.1109/ASCC.2013.6606270> doi:10.1109/ASCC.2013.6606270.

- [61] Kai Zhang, Eric J. Gonzalez, Jianglong Guo, and Sean Follmer. Design and Analysis of High-Resolution Electrostatic Adhesive Brakes Towards Static Refreshable 2.5D Tactile Shape Display. 12(4):470–482. URL: <https://ieeexplore.ieee.org/document/8845668/>, <https://doi.org/10.1109/TOH.2019.2940219> doi:10.1109/TOH.2019.2940219.